FACULTY OF SCIENCES

# Modified PMOs for Luminescence and Catalysis


Laurens Bourda

Promotor: Prof. Dr. Pascal Van Der Voort
Co-promotor: Dr. Himanshu Sekhar Jena
Supervisor: Dr. Anna Kaczmarek


Academic Year 2017–2018

A dissertation submitted to Ghent University in partial fulfilment of the requirements for the degree of Master of Science in Chemistry

GHENT UNIVERSITY

# Acknowledgements

Finally, we have reached the end of a very long, busy and exciting year. It's now Saturday night and I'm writing this while watching the champions league finale. In my opinion, this anecdote is a perfect summary of the year, whatever I was doing, this work was always on my mind. While I owe many people my most sincere acknowledgements for their help during the year, I owe as many friends my apologies for my limited availability throughout the year. In conclusion, this could be a very long list and I hope I don't forget anyone.

First of all and most importantly, I'd like to thank Prof. Dr. Pascal Van Der Voort, for making it possible for me to work on this very exciting project and even go to Noordwijkerhout and present my work on Netherlands' Catalysis and Chemistry Conference XIX. Especially since even before the project started some guidance problems arose and changes in the original plan had to be made. Moreover, I'm very grateful for getting the opportunity to pursue my own ideas, make my own mistakes and just generally getting a lot of trust and freedom. Finally, I really liked to work in COMOC and experience and learn and use a whole range of techniques and methods, it gave me the variety and challenge I came to love during the project.

My greatest gratitude to Dr. Himanshu Jena, who was my source of knowledge through the entire year and the victim of my ever arising questions. My thanks for guiding me trough the year and difficult parts, for always being optimistic and for the refreshing and helpful ideas, comments and notes. Furthermore, a special thanks for Dr. Anna Kaczmarek, without you the project had looked completely different, as I had not even come up with the idea to test these exciting luminescence applications for my materials. On top of that my great thanks for the many comments and help on the writing part.

Funda and Tom, thank you for the help with all instruments and technical parts. Thanks for wanting to join in this 'nice' precursor synthesis and everlasting column separations. But most importantly, thank you for the nice and friendly chats and conversations. Those were an important part of my day and one of the reasons of my evergoing happiness during the year.

Actually, I should thank all COMOC people, you all made the year so much easier and nicer. I really enjoyed the small talks in the office or the lab, our lunch and kicker breaks, our

badminton and tennis sessions. You made me feel very welcome and part of the group very quick and I'm very grateful for that.

Also I would like to acknowledge Katrien Haustraete for TEM measurements, Jan Goeman for GC/MS analysis and Olivier Janssens for SEM imaging.

Continuing with my friends, Benjamin, Boris, I know we didn't meet and eat together as much as we used to and I'm sorry for that. Still, it was very nice to share our excitement and disappointment about our projects during the year with you, Dieter, and Adriaan in the 'Koen Koen Klan fanclub'. I also enjoyed the seldom moments we still came together. Moreover, I'm really thankful for the proofreading by Benjamin, correcting all my little mistakes must have been a hell of a job but you even seemed to enjoy it.

All my other classmates and fellow students, you're too many to all name here, I really enjoyed our studying years together and I hope we will meet regularly after we are graduated. I wish you all the very best and I want to be regularly informed on your latest escapades. I also want to give a special mention to Loren and Tim, who helped me numerous times with LaTeX troubles and errors. Without their help this work hadn't looked as nice as it does now.

Lotte, Maya, Cheyenne and Jana, I think Malta was almost the last time we all came together. It has been so long, I really miss our regular 'terrasjes', hopefully we can catch up during the summer! Many thanks for listening to my stories about this project, I know you didn't care about the subject, but still telling you was refreshing.
Joachim, thanks for your outsider comments on the work, it really helped me bringing it to the level it reached now. Like with all previously named people, we should meet more regularly!

Mama and papa, Arnaud and Cedric, thanks for your evergoing support, for the questions how I'm doing and for your advicr on how to handle stuff after graduating. I guess you didn't understand most of what I told about the project and still you kept asking how I was progressing. I know you almost never saw me and still you did everything you could to help me. Many, many thanks, not only for this year but for all these years.

Finally, I have reached the last and maybe most important person. By now the game is already finished and I want to go to sleep, but first I'd like to thank you, Imke. During the whole year, you were my support, the first one to receive my complains and the first one to share my joy. I know you don't care about chemistry, but still you tried your best to understand what was taking all my attention. Our weekends together were my relax periods, the times that I could truly be myself and just enjoy. Thank you for everything!

Laurens Bourda
Gent, May 26, 2018

# Modified PMOs For Luminescence And Catalysis

L. Bourda*[a], H. Jena[a], A. Kaczmarek[b] and P. Van Der Voort[a]

[a] COMOC, Center for Ordered Materials, Organometallics & Catalysts , Department of Chemistry, Ghent University, Krijsglaan 281-S3, B-9000 Ghent, Belgium
[b] $L^3$, Luminescent Lanthanide Lab, Department of Chemistry, Ghent University, Krijsglaan 281-S3, B-9000 Ghent, Belgium.
*laurens.bourda@ugent.be

The monoallyl ring Periodic Mesoporous Organosilica (PMO), a mesoporous material showing high surface area and cylindrical 5.0 nm pores, was used as versatile and stable support material. Two different ligands, a porphyrine ligand and a picolinic acid derivate, were covalently attached to this support using thiol-ene click reaction. By coordination of different metals, these materials were proven to show potential for different applications. The $Co^{2+}$ coordinated materials demonstrated catalytic activity for Carbon Capture and Utilization (CCU) by catalyzing the coupling of $CO_2$ and epoxides to cyclic carbonates. While coordination of $Ln^{3+}$ ions gave very interesting visible (for the picolinic acid derivate material) and NIR (for the porphyrine material) luminescence properties.

*Keywords*: PMOs, Porphyrins, Picolinic acid, $CO_2$ conversion, $Ln^{3+}$ luminescence

## Introduction

Periodic Mesoporous Organosilicas (PMOs), firstly synthesized in 1999 by Ozin (1), Stein (2) and Inagaki (3) are hybrid organic-inorganic support materials. The ordered mesoporosity of these materials is obtained by the hydrolysis and condensation of organically bridged silica precursors $(X)_3Si{-}R{-}Si(X)_3$ with R an organic group and X a methoxy/ethoxy group) around a liquid crystal template. A big advantage of PMOs, compared to other silica materials, is the direct incorporation of organic groups in the network, rendering more stable and hydrophobic materials. To further improve these properties, increased organic loading was desired, this was obtained by the development of the ring type PMO (4), later modified to a versatile starting material by the addition of a reactive allyl group (monoallyl ring PMO) (5).

Porphyrin complexes have shown to be interesting materials with a remarkably broad range of applications. They are not only vital for biological functions as oxygen, electron and solar energy transfer (6), these materials also draw much attention for application in photodynamic therapy (PDT) (7). Moreover, because of their ability to strongly absorb light over a broad wavelength range and easily bind $Ln^{3+}$ ions with their tetraaza macrocylic core, these materials are perfect ligands for near-infrared (NIR) emitting lanthanides (8). Furthermore, they show great potential in the catalytic conversion of $CO_2$ and epoxides to cyclic carbonates (9). Still, these materials are expensive, hard to handle and difficult to

isolate. It is by consequence evident that heterogenization of these complexes would be very attractive.

To avoid time-consuming and expensive research on the linking of ligands to a PMO support, a universal anchoring method would be highly desired. Moreover, this would render more readily comparable results, as the influence of ligand attachment would be minimal. Combining thiol-ene click chemistry (10) with Anzenbacher's *et al.* method (11) for heterogenization of porphyrins, such a method could be developed for the coupling of carboxylic acid bearing groups on the monoallyl ring PMO.

Here, the power of our method is illustrated by the coupling of a complex (porphyrin) and simple ligand onto the monoallyl PMO. Picolinic acid was chosen as the second ligand, as the coupling method generates two neighboring N atoms, leading to an ideal coordination space for catalytically active metals or luminescent lanthanides. Moreover, to the best of our knowledge, no PMO with porphyrin functions dangling in the porphyrin has been reported up to date, while only one material similar to the PMO coupled picolinic acid has been described (12).

## Experimental

The following chemicals were used as received: 1,1,3,3,5,5-hexaethoxytrisilacyclohexane (HETSCH, 95%, ABCR), t-BuLi (1.7 M in pentane, Sigma-Aldrich), allylbromide (99%, Sigma-Aldrich), anhydrous THF (99.9%, 250 ppm BHT as inhibitor, Sigma-Aldrich), $NaHCO_3$ (Chem lab, 99.5%+), silica gel (60˚A, 60-200 μm, ROCC), EtOAc (99%, Carl Roth), hexane (mixture of isomers, Acros Organics), Pluronic P123 (Mn = 5800 g/mol, Sigma-Aldrich), KCl (99.5%, Carl Roth), HCl (37%, Fisher Chemical), Acetone (laboratory reagent grade, Fisher Chemical), 4,4',4",4"'-(Porphine-5,10,15,20-tetrayl)tetrakis(benzoic acid (> 97 %, TCI), Picolinic Acid (99%, Acros Organics), $SOCl_2$ (99.5+%, Acros Organics), Cysteamine (> 95% TCI), $CHCl_3$ (Laboratory reagent grade, Fisher Chemical), $NEt_3$ (> 99%, Sigma-Aldrich), NaCl (> 99.5%, Fisher Chemical), $MgSO_4$ (99% anhydrous, Fisher Chemical), 2-hydroxy-4'-(2-hydroxyethoxy)-2-methylpropiophenone (Irgacure 2959, 98%, Sigma-Aldrich), $NaH_2PO_4 \cdot 2\,H_2O$ (Typanalyse, Ferak Berlin), $Na_2HPO_4$ (98 %, Sigma-Aldrich, $Ln(NO_3)_3 \cdot 6H_2O$ (Ln = Eu, Tb, Yb) (99.9% Sigma Aldrich), Methanol (96%, VWR), $Co(OAc)_2 \cdot 4H_2O$ (99%, Honeywell Riedel-de Haën AG), DMF (Analytical reagent grade, Fisher Chemical), Epichlorohydrin (99.9%, Fluorochem), mesitylene (98%, Sigma-Aldrich), $CH_2Cl_2$ (HPLC grade, Fisher Chemical), DMAP (≥98%, Fluka Analytical), $CO_2$ (Air liquid Belgium)

PMO synthesis

The procedure described by Clerick *et al.* (13) was used.

For the synthesis of the precursor 60 mL of anhydrous THF and 20 mL HETSCH was mixed. This solution was heavily stirred at -78.5 °C and 1 equivalent t-BuLi (18.7 mL) was added over 30 minutes, followed by 30 minutes of continued stirring. In a separate flask a solution of 40 mL anhydrous THF and 4.568 mL allylbromide (1.07 equivalents) was prepared and cooled to -78.5 °C. The HETSCH solution was added to the stirred allylbromide solution over 30 minutes. The resulting mixture was left to stir overnight with temperature gradually increasing. Afterwards, the resulting yellow solution was washed with 25 mL 0.2 w% $NaHCO_3$ solution and 2x50 mL $H_2O$. The solvent was evaporated (under reduced pressure) out of the resulting organic phase and a faint yellow oil was

obtained. The resulting AHETSCH precursor was purified by flash column chromatography with hexane:EtOAc (10:1).

For the PMO synthesis 0.375 g Pluronic P123 and 2.19 g KCl were dissolved in 11.25 mL $H_2O$ in a 50 mL flask. 0.9 mL of HCl (37%) was added and the mixture was stirred (600-800 RPM) to yield a clear blue solution. Subsequently, 0.5625 g of the yielded AHETSCH was added to yield a molar composition of AHETSCH:H2O:P123:HCl:KCl 1:500:0.0517:8.62:23.5. The mixture was directly brought to stirring at 45 °C for 3 hours, after which the stirring was turned off and the temperature was raised to 95 °C to let the material age for 24 hours. A white precipitate was formed and filtered off. The powder was washed with 3x25 mL $H_2O$ and 3x25 mL acetone and subsequently the template was removed using 6 hour Soxhlet extraction in acetone. The yielded white powder was dried overnight at 120 °C in vacuum.

Ligand attachment

In a procedure derived from Anzenbacher *et al.* (11), porphyrin (100 mg, 0.126 mmol) or picolinic acid (155 mg, 1.26 mmol) were dissolved in 5 mL $SOCl_2$. The mixture was refluxed for 4 hours at 80 °C under Ar atmosphere. The remaining solvent after reaction was removed under reduced pressure. Subsequently the chlorinated porphyrin/picolinic acid was dissolved in 10 mL $CHCl_3$ and stirred at 0 °C under Ar atmosphere. Separately, 1 equivalent of cysteamine was dissolved in 10 mL $CHCl_3$ and 2 equivalents of $NEt_3$ , this was drop wise added to the porphyrin/picoline solution. The mixture was covered with Al-foil and stirred for 2 hours. The resulting solution was then washed with $NaHCO_3$ and brine, before drying of the organic phase over $MgSO_4$ (this washing step was not used for the porphyrin mixture). After evaporation of the organic phase, a light yellow (picoline) or dark purple (porphyrine) powder was obtained.

To click the generated amides on the PMO a pH 7 phosphate buffer was first prepared by dissolving 0.655 g $NaH_2PO_4 \cdot 2H_20$ (4.2 mmol) and 0.696 g $Na_2HPO_4$ (5.8 mmol) in water, the resulting solution was flushed with Ar. 50 mL Irgacure 2959 (0.22 mmol, excess), was dissolved in the phosphate buffer and flushed with Ar. In a general procedure, 100 mg of monoallyl ring PMO and 0.14 mmol of the amide (25.5 mg picolin compound or 126.735 mg porphyrin compound) were added to this Irgacure initiator. The resulting suspension was mixed in ultrasonic bath and treated for 3 hours in a home-made UV reactor ($\lambda$ = 360 nm). The product was filtered of and washed with $H_2O$ and acetone. Subsequently, to remove all leftover reagents, the powder was Soxhlet extracted using acetone for 6 hours. Finally, the yielded product was dried overnight at 110°C.

Coordination of $Co^{2+}$

In a general procedure, equimolar amounts of the ligand and $Co(OAc)_2 \cdot 4H_2O$ are dissolved in DMF and refluxed overnight at 160 °C. Afterwards, the obtained powder is filtered and washed with DMF. The product is purified using Soxhlet extraction with acetone (6 hours).

Coordination of $Ln^{3+}$

In a general procedure, an excess of a lanthanide salt was dissolved in 5 mL of methanol and added to a pyrex tube containing the PMO material. The tube was closed and treated

with ultrasounds for 20 minutes, before leaving for 24 hours at room temperature to soak. Afterwards, the mixture was heated for 24 hours at 85 °C. After cooling to room temperature, the resulting powder was filtered of and washed with methanol to remove adsorbed lanthanide ions. Finally, the resulting powder was dried at 60 °C.

Catalytic procedure

In a general procedure, a 125 mL stainless steel Parr reactor was loaded with 10 mg catalyst, 1 mg DMAP, 46.26 mg epichlorohydrin and 2 mL $CH_2Cl_2$ . The reaction vessel was subsequently flushed and placed under pressure with $CO_2$, whereafter it was heated to reach 120 °C and the desired pressure. After the desired reaction time had passed, the mixture was allowed to cool down to ~ 40 °C and the resulting mixture was transferred to a 25 mL flask using acetone. The acetone was removed under reduced pressure to yield the resulting mixture for analysis.

Characterization and analysis

$N_2$ -sorption experiments were performed on a micromeretics Tristar II at 77 K. Diffuse Reflectance Infrared Fourier Transform Spectroscopy (DRIFTS) measurements were done using a Nicolett 6700 FTIR spectrometer equipped with a Greasby-Specac diffuse reflectance cell, modified to measure samples at 20 - 300 °C under vacuum. Pore ordening was confirmed using PXRD on a Thermo Scientific ARL X'TRA X-ray diffractometer using Cu Kα radiation of 40 kV and 30 mA. CHNS analysis was performed on a Thermo Flash 200 elemental analyser with $V_2O_5$ as catalyst. Co loadings were studied by X-ray Fluorescence (XRF) on a Rigaku NEX CG with an Al source and compared to Sr-Kα as internal standard. The chemical structure of reagents and catalytic products were analyzed using $^1$H NMR in $CDCl_3$ or DMSO, on a Bruker 300 MHz AVANCE spectrometer with chemical shifts (δ) expressed in ppm relative to a tetramethylsilane standard.

Luminescence properties were measured using an Edinburgh Instruments FLSP920 UV-vis-NIR spectrometer setup, equipped with a 450W Xe lamp as steady state excitation source. Luminescence decay times of the sample were obtained via a 60W pulsed Xe lamp, operating at a frequency of 100 Hz. PL decay times of the ungrafted samples were recorded using using a Supercontinuum white light laser for TCSPC (Time Correlated Single Photon Counting, 80 ps - hundreds of ns). Emission signals in the visible range were detected using a Hamamatsu R928P photomultiplier tube, a Hamamatsu R5509-72 photomultiplier was used for signals in the NIR region. To properly compare results, all setings were kept equal between measurements (same amounts, all samples put between quartz plates, same split size, step and dwell time). All emission spectra have been corrected for detector response.

## Results and discussion

Covalent coupling of different ligands on the PMO

The synthetic procedure used for the coupling of porphyrin and picolinic acid on the PMO is schematically shown in **Figure 1**. As can be seen, the method consists of chlorination of the carboxylic acid and subsequent amide coupling with cysteamine. This is followed by a thiol-ene click reaction with PMO allyl functions. By coupling of picolinic acid the shown Pic@PMO structure is yielded, while the anchoring of porphyrin on the PMO gives the presented Porph@PMO structure.

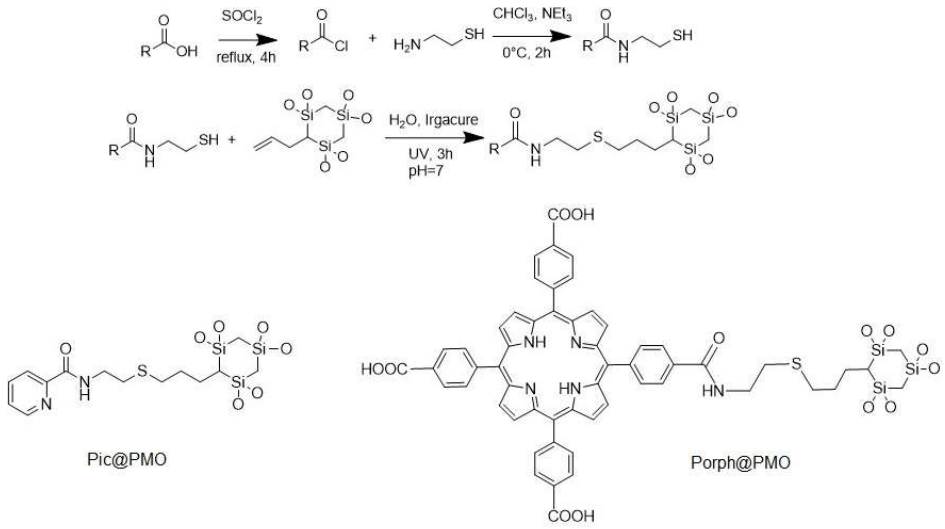


Figure 1. Above: The used coupling method to anchor ligands on the PMO, with R = the desired ligand. Below: a schematic drawing of the obtained materials.

The coupling was confirmed via DRIFTS, in **Figure 2** a spectrum of pure monoallyl PMO (monoallyl PMO) is compared to the spectra obtained for PorphCys (amide coupled porphyrin with cysteamine), PicCys (resulting amide from coupling of picolinic acid and cysteamine), Pic@PMO 3 and Porph@PMO 1. Aside from the C-H and Si-O-Si stretch vibrations at respectively 2950-2800 $cm^{-1}$, 1200-1000 $cm^{-1}$ and 800 $cm^{-1}$, three allyl peaks show up in the Monoallyl PMO spectrum: the olefin C-H stretch at 3078 $cm^{-1}$, the C=C stretch at 1637 $cm^{-1}$ and the olefin C-H out of plane deformation at 908 $cm^{-1}$ (13). However, the ligand coupled materials show a clear peak at 1599 $cm^{-1}$, assigned to the amide and indicating successful coupling on the PMO. Moreover, The C=C stretch intensity is clearly reduced, which indicates that these allyl groups have been used in the thiol-ene click reaction (still, this reaction is not complete as peaks stay visible, most likely not all allyl

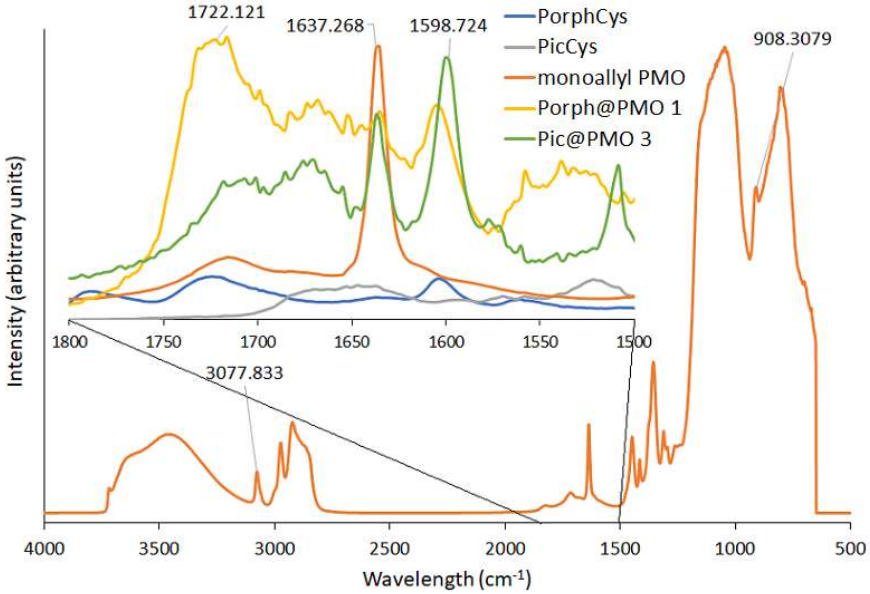


Figure 2. DRIFTS spectrum of monoallyl ring PMO, a zoom on the region of interest for coupling is provided with additional spectra of PorphCys, PicCys, Porph@PMO 1 and Pic@PMO 3

groups are accessible for the ligands). Observing the PicCys spectrum, it is visible that the amide peak is shifted and sharper after binding, due to the increased mass of the compound. For the porphyrin this is, most likely due to the extensive conjugated aromatic system, not observable as PorphCys already showed a peak at the amide position. An additional peak at 1722 $cm^{-1}$ in the porphyrin samples was assigned to the carboxylic acid functions.

Structural analysis data is presented in **TABLE I**, a clear difference in structural response could be observed for both materials. While Pic@PMO 3 shows almost no difference in structural data before and after reaction, a big decrease in Surface area ($S_{BET}$) and pore volume ($V_p$) is observed for Porph@PMO 1. This is explained by the higher loading and molecular mass of the porphyrin ligand. Using the loading, a ligand mass percentage of 52.23% was calculated for Porph@PMO 1. As Surface area and pore volume are dependent on the mass, it was expected that these values would decrease. However, Pic@PMO 3 only shows 6.6 mass% ligand, which is in the error range of $N_2$-sorption measurements and thus explains the almost equal values before and after modification. Still, the invariant pore size ($d_p$) and wall thickness (t), indicate that the ligands are indeed attached and not adsorbed on the pores. Moreover, as characteristic type IV isotherm with sharp H1 hysteresis are observed both before and after modification (see the full thesis for these isotherms), it could be concluded that the post-modification did not disturb the materials pore structure.

**TABLE I: Structural analysis of coupled materials**

| | Pic@PMO 3 before | Pic@PMO 3 after | Porph@PMO 1 before | Porph@PMO 1 after |
|---|---|---|---|---|
| $S_{BET}(m^2/g)$[a] | 548 | 565 | 605 | 406 |
| $V_p\ (cm^3/g)$[b] | 0.61 | 0.63 | 0.78 | 0.52 |
| $d_{p,\ BJH}$ (nm)[c] | 5.0 | 5.1 | 5.1 | 5.1 |
| t (nm)[d] | 7.7 | 7.3 | 7.3 | 7.0 |
| Loading (mmol/g)[e] | / | 0.37 | / | 0.61 |

[a]Specific surface area determined via Brunauer-Emmett-Teller theory. [b]Pore volume determined from adsorption branch at P/P0 = 0.99. [c]Pore size calculated from desorption branch following Barrett-Joyner-Halenda theory. [d]wall thickness was calculated combining pore volume and XRD results, [e]Ligand loading was determined using CHNS analysis

## Catalysis: from $CO_2$ to cyclic carbonates

Based on the catalytic results obtained by Paddock et al. (9), our heterogeneous $Co^{2+}$ coordinated catalysts (Co@Pic@PMO and Co@Porph@PMO) were tested in the catalytic coupling of $CO_2$ and epichlorohydrin. The results were analyzed using $^1H$ NMR. DMAP was chosen as a co-catalyst and reaction time was set to two hours. In these conditions, a comparison between the developed heterogeneous catalysts and a homogeneous catalyst was made. Moreover, the catalysts were tested for activity at different pressures. The obtained conversions can be found in **TABLE II**, a proposed catalytic scheme is presented in **Figure 3.**

**TABLE II: $CO_2$ pressure effect on catalytic activity**

| Entry | Catalyst | Pressure (bar) | Conversion (%) |
|---|---|---|---|
| 1 | Co@Porph | 6 | 100 |
| 2 | Co@Porph@PMO | 6 | 91.6 |
| 3 | Co@Porph@PMO | 4 | 78.2 |
| 4 | Co@Porph@PMO | 2 | 18.2 |
| 5 | Co@Pic@PMO | 6 | 79.9 |
| 6 | Co@Pic@PMO | 5 | 71.3 |
| 7 | Co@Pic@PMO | 4 | 76.2 |

Reaction conditions: catalyst (10 mg), co-catalyst (DMAP, $8*10^{-3}$ mmol), epichlorohydrin (0.5 mmol), $CH_2Cl_2$ (2 mL), time = 2 hours, 120 °C.

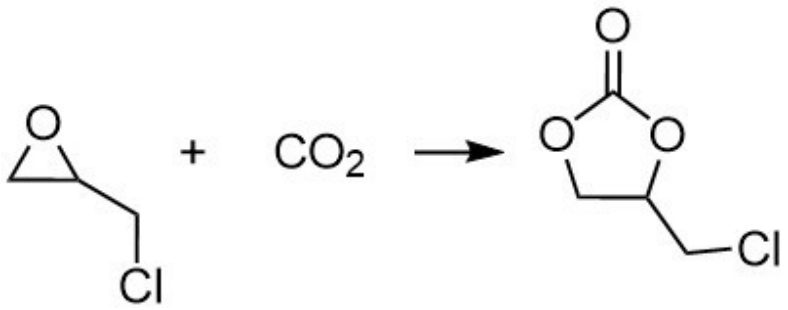


Figure 3. A scheme of the catalyzed coupling of $CO_2$ and epichlorohydrin

From the calculated conversions at 6 bar (entry 1, 2 and 5), it could be concluded that both materials exhibit excellent catalytic activity. The homogeneous system of $Co^{2+}$ coordinated to pure porphyrin (entry 1) proves itself as a very efficient catalyst with a conversion of 100%, but the heterogenized porphyrin also converted more than 90% of the epichlorohydrin to the desired cyclic carbonate. This result is, due to diffusion limits in the heterogenized materials, quite expected. Moreover, the picolinic acid derivate (entry 4), which to the best of our knowledge hasn't been tested for this reaction yet, also shows a conversion close to 80%. It is noted that this is less than for the porphyrin materials, but this picolinic acid ligand is much simpler and cheaper to prepare.

When following the conversion using Co@Porph@PMO as a catalyst in function of pressure (entry 2-4) it is clear that high pressure is required to efficiently perform this reaction. At 4 bar still a good conversion is obtained of close to 80%, but at 2 bar a dramatic drop in conversion was observed. These results are in agreement with the results obtained by Paddock *et al.* (9) for homogeneous catalysts, as they even worked at much higher pressures than 6 bars to get good conversions and fast reaction. However, when looking at the Co@Pic@PMO conversions in function of pressure (entry 5-7), it is observed that almost no pressure dependence occurs.. Most likely some starting material gets stuck in the pores of the PMO and thus can't be found in the NMR spectrum. As very small quantities are used here, this could lead to huge fluctuations in the observed conversions. It has to be noted that this process could also have had significant influence on the previously discussed conversions.

To check recyclability of the catalysts, some preliminary tests have been done. The filtrate of all catalytic reactions have been tested for $Co^{2+}$ presence to see if leaching occurs. As XRF analysis of the samples showed no $Co^{2+}$ or very small peaks between the noise, it could be concluded that the developed catalysts does not leach. Moreover, a first recyclability test was already done using Co@Porph@PMO, with conditions like in entry 2, but only one hour of reaction time. Analyzing this recycling run, 70.3% conversion was obtained. Most likely after two hours, this run would thus have yielded comparable conversion to the 91.6% observed for Co@Porph@PMO. Which means that the starting material left in the pores does not poison the catalyst.

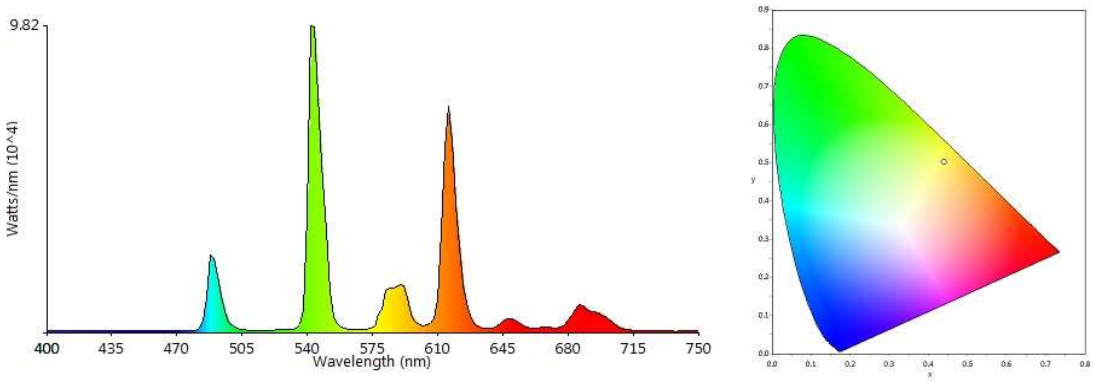


Figure 4. Luminescence profile of Tb,Eu(1:1)@Pic@PMO excited at 322 nm, left: emission spectrum with representation of matching colors at each wavelength, right: CIE chromaticity diagram of the sample

Luminescence: Visual and NIR emittance

Pic@PMO luminescence: to obtain luminescent properties in the Pic@PMO samples, it has been (co-)grafted with $Tb^{3+}$ and $Eu^{3+}$ ions, yielding green and red emission. In **Figure 4** the luminescence profile of a sample containing equal molar ratios of $Tb^{3+}$ and $Eu^{3+}$ (Tb,Eu(1:1)@Pic@PMO) , excited at 322 nm, is presented. Spectra of pure $Tb^{3+}$/ $Eu^{3+}$ grafted samples can be found in the full thesis.

It could be observed that both $Tb^{3+}$ and $Eu^{3+}$ emit efficiently, as intense, sharp f-f transition peaks of both are observed (for $Tb^{3+}$ the most intense peak, emitting in the green region, can be found at 542 nm, for $Eu^{3+}$, the most intense peak, emitting in the red, is situated at 616 nm). Altogether, a yellowish emission was observed. When looking at the CIE chromatogram, it is clear that an additional blue emitting component is required to emit white light. However, for this material, blue emitting bands could only result from the ligand and as no ligand band is present it will thus be impossible to obtain pure white light for this material.

Porph@PMO luminescence: Porphyrin ligands are, as previously discussed, perfect ligands for NIR emitting lanthanides. As $Yb^{3+}$ is the strongest emitter of the NIR lanthanides, it was grafted on Porph@PMO to yield Yb@Porph@PMO. When looking at the excitation profile (**Figure 5**) of this material, two clear regions show up. First, around 475 nm, the porphyrin Soret band could be observed, characteristic for the allowed porphyrin $S_0 \rightarrow S_2$ transition. Still, it has to be noted that a broad band around 350 nm also appeared, which could not be assigned. As this band was not present in pure Porph@PMO, it could maybe have a relationship with the low wavelength Soret band shoulder observed in that sample. Secondly, at higher wavelengths, between 650 and 750 nm, at the far edge of the visual range, 4 peaks appear. The position and relative intensity (to the Soret band) of these peaks are unprecedent for porphyrin materials, moreover these are not observed in ungrafted Porph@PMO (as can be seen in the excitation spectra for that material, see the full thesis). It could be possible that these peaks correspond with the porphyrin Q bands (characteristic for the forbidden porphyrin $S_0 \rightarrow S_1$ transitions), usually observed as weak

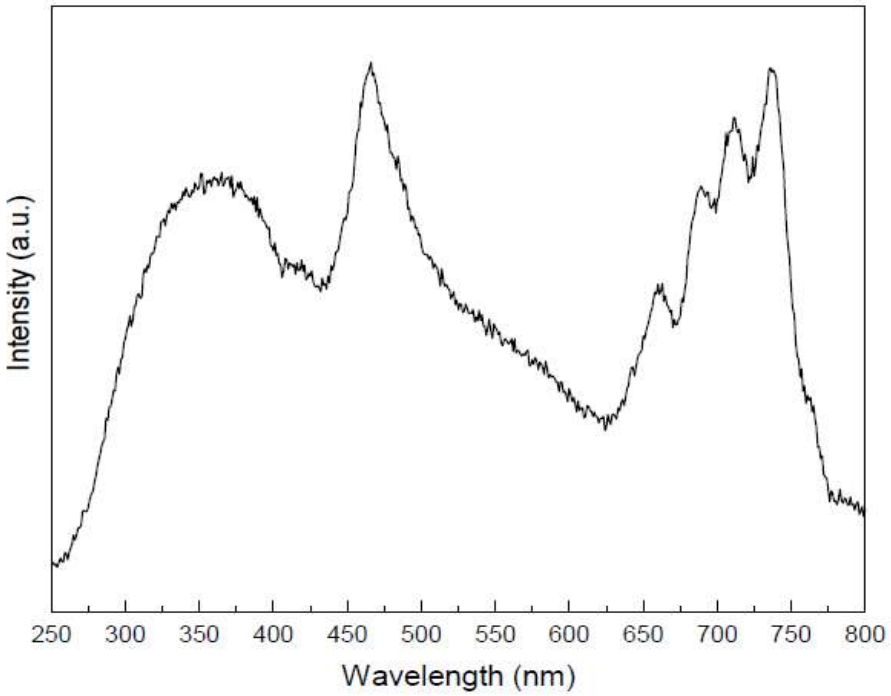


Figure 5. Excitation spectrum of Yb@Porph@PMO

peaks around 600 nm, and shifted due to the porphyrin-PMO attachment. However, a UV- absorption test has to be performed to confirm if real light absorption happens at these high wavelengths.

Moreover, excitation of the material was possible in both discussed peaks, excitation at 467 nm and at 650 nm both yielded characteristic $Yb^{3+}$ emission around 975 nm. As these materials could thus be excited at high wavelengths and emit light in the NIR range, they could potentially be very interesting for cancer treatment using PDT.

**TABLE III: Luminescent decay times**

| Sample | $T_1$(µs) | $T_2$(µs) | $T_{av}$(µs) |
|---|---|---|---|
| Pic@PMO | $8.1*10^{-4}$ | $4.6*10^{-3}$ | $1.1*10^{-3}$ |
| Eu@Pic@PMO | 232.9 | 626.0 | 189.3 |
| Tb@Pic@PMO | 703.0 | 171.0 | 611.5 |
| Tb,Eu(1,1)@Pic@PMO 542 nm peak | 86.2 | 450.7 | 324.9 |
| Tb,Eu(1,1)@Pic@PMO 616 nm peak | 469.3 | / | / |
| Yb@Porph@PMO 467 nm excitation | 19.4 | 4.6 | 11.9 |
| Yb@Porph@PMO 650 nm excitation | 18.0 | 3.9 | 9.8 |

Luminescence decay times: decay times have been measured for all $Ln^{3+}$ grafted materials and are presented in **TABLE III.**

It is readily noted from the presented data that decay times for pure Pic@PMO are very short, in the range of 1 ns. The lanthanide coordinated materials show, as expected, much longer decay times between 100 µs and 1 s. Furthermore, $Tb^{3+}$ shows more efficient luminescence than $Eu^{3+}$ as its decay times are considerable longer. As the energy level of the picolinic acid excited state matches better with the $Tb^{3+}$ accepting level, this result was quite expected. More surprising is the trend in the co-doped material, as the $Eu^{3+}$ peak shows the longest decay time in this sample. This results suggests that there is Tb-to-Eu energy transfer in this material, suggesting that the picolinic ligands are grafted in close proximity to one another on the PMO support.

The porphyrin samples both show quite long decay, in agreement with comparable materials. Moreover, both excitation wavelengths result in efficient luminescence as the obtained decay times are very comparable. Still, excitation at 467 nm (in the Soret band) proves to be slightly more efficient.

## Summary

The monoallyl ring PMO was successfully used as support material for two different ligands. Using an universal method, porphyrin and picolinic acid were covalently bound to the support without influencing the ordered mesoporous structure.

Successful preliminary catalytic tests showed the developed materials have potential for the catalytic conversion of $CO_2$ and epoxides to cyclic carbonates. Moreover, the catalysts proved not to be prone to leaching and a first second run test showed similar activities as the frsh catalysts.

By grafting of $Ln^{3+}$ ions, diverse luminescent applications are within reach. The Pic@PMO materials were (co-)grafted with $Tb^{3+}$ and $Eu^{3+}$ to yield respectively green, red and warm yellow light. The Porph@PMO materials showed great potential in NIR emittance, with the possibility to be efficiently excited at both high (at the edge of visual and NIR range) and low (in the blue light range) wavelengths.

## Acknowledgments

Many thanks to F. Aliç and T. Planckaert for their help with numerous measurements and to J. Ouwehand for productive discussions about PMO behavior. My gratitude to UGhent department of chemistry for giving me the opportunity to work on this project.

## References

1. T. Asefa, M. J. MacLachlan, N. Coombs, and G. A. Ozin, Nature, 6764, 402, 867–871,
2. B. J. Melde, B. T. Holland, C. F. Blanford, and A. Stein, Chemistry of Materials, 11, 11, 3302–3308
3. S. Inagaki, S. Guan, Y. Fukushima, T. Ohsuna, and O. Terasaki, Journal of the American Chemical Society, 41, 121, 9611–9614
4. K. Landskron, B. D. Hatton, D. D. Perovic, and G. A. Ozin, . Science, 5643, 302, 266–269
5. M. Ide, E. De Canck, I. Van Driessche, F. Lynen, and P. Van der Voort, RSc Advances, 8, 5, 5546–5552
6. K. M. Kadish, Smith K. M., and R. Guilard. The Porhyrin Handbook. Academic Press, 2000.
7. T. J. Dougherty, C. J. Gomer, B. W. Henderson, G. Jori, D. Kessel, M. Korbelik, J. Moan, and Q. Peng, Journal of the National Cancer Institute, 12, 90, 889–905
8. V. Bulach, F. Sguerra, and M. W. Hosseini, Coordination Chemistry Reviews, 15-16, 256, 1468–1478
9. R. L. Paddock, Y. Hiyama, J. M. McKay, and S. T. Nguyen., Tetrahedron Letters, 9, 45, 2023–2026
10. C. E. Hoyle and C. N. Bowman., Angewandte Chemie International Edition, 9, 49, 1540–1573
11. P. Anzenbacher, V. Kral, K. Jursikova, J. Gunterova, and A. Kasal., Journal of Molecular Catalysis a-Chemical, 1, 118, 63–68
12. M. Vasconcellos-Dias, C. D. Nunes, P. D. Vaz, P. Ferreira, P. Brandao, V. Felix, and M. J. Calhorda., Journal of Catalysis, 2, 256, 301–311
13. S. Clerick, E. De Canck, K. Hendrickx, V. Van Speybroeck, and P. Van der Voort., Green Chemistry, 22, 18, 6035–6045

# Contents

# List of Figures

# List of Tables

# List of Abbreviations

| | |
|---|---|
| $a_0$ | cell parameter |
| AHETSCH | 2-allyl-1,1,3,3,5,5-hexaethoxytrisilacyclohexane |
| | |
| BET | Brunauer, Emmet and Teller |
| BJH | Barret, Joyner and Halenda |
| | |
| CCS | Carbon Capture and Storage |
| CCT | Correlated Color Temperature |
| CCU | Carbon Capture and Usage |
| CIE | International Commission on Illumination |
| COF | Covalent Organic Framework |
| | |
| $d_{(100)}$ | d spacing of the 100 planes |
| $d_{p,BJH}$ | BJH desorption pore width |
| DMAP | 4-Dimethylaminopyridine |
| DMF | Dimethylformamide |
| DRIFTS | Diffuse Reflectance Infrared Fourier Transform Spectroscopy |
| DTA | Differential Thermal Analysis |
| | |
| e | wall thickness |
| | |
| HETSCH | 1,1,3,3,5,5-hexaethoxytrisilacyclohexane |
| HMDS | hexamethyldisilazane |
| | |
| MCM | Mobil Composition of Matter |
| MOF | Metal Organic Framework |

| | |
|---|---|
| NIR | near-infrared |
| NMR | Nuclear Magnetic Resonance |
| P123 | Pluronic P123 |
| PE | polyoxyethylene |
| PicCys | N-(2-mercaptoethyl)picolinamide |
| PMO | Periodic Mesoporous Organosilica |
| PO | polyoxopropylene |
| PorphCys | 4,4',4"-(20-(4-((2-mercaptoethyl)carbamoyl)phenyl)porphyrin-5,10,15-triyl)tribenzoic acid |
| PXRD | Powder X-ray Diffraction |
| RC-delay | Resistive-capacitive delay |
| $S_{BET}$ | BET Surface Area |
| SBA | Santa Barbara Amorphous |
| SBU | Secondary Building Units |
| SEM | Scanning Electron Microscopy |
| STEM-EDX | Scanning Transmission Electron Microscopy Energy-Dispersive X-ray spectroscopy |
| TCSPC | Time Correlated Single Photon Counting |
| TEM | Transmission Electron Microscopy |
| TEOS | Tetraethyl orthosilicate |
| TGA | Thermal Gravimetric Analysis |
| THF | Tetrahydrofuran |
| $V_p$ | BJH desorption pore volume |
| XRF | X-ray Fluorescence |

# Chapter 1

# Periodic Mesoporous Organosilicas (PMOs)

## 1.1 Development of PMOs: a walk through the history of porous materials

The first porous materials, zeolites, were already discovered in 1756 by Cronstedt [1] and have been synthesised since the late 1940's [2]. Nowadays they are commonly used in many industrial processes. These materials are crystalline aluminosilicates built out of corner-sharing $[SiO_4]^{4-}$ and $[AlO_4]^{5-}$ tetrahedra, arranged in such a way that they form porous structures (well-defined networks of channels and cavities) with molecular dimensions. Zeolite structures can be classified based on their Secondary Building Units (SBU), which link together to yield the complex three-dimensional structure of the corresponding zeolite. These materials have some very promising catalytic properties, they behave like superacids (a material possesing both Bronsted and Lewis acid sites) and are shape selective. Besides that, they can also be used as washing powder due to their ion exchange properties or as gas adsorbents by making use of their molecular sieve properties. But they also show an important drawback [3], the largest zeolites consist of 12-ring pore systems, with ring dimensions in the range of 7 Å, which is more or less the size of a substituted aromatic ring. As a result of this, a size limitation for zeolite catalysis exists. Compounds larger than these pores can not enter the system and will by consequence not react.

From the 1980's on, alternatives without these micropore (pore diameters smaller than 2 nm) limitations have been searched for, but it was only in 1992, with the creation of Mobil Composition of Matter (MCM) [4] that the first stable ordered mesoporous (pore diameter in the range of 2-50 nm) material was synthesized. This material was created by adding long-

chained organic cationic surfactants, organized in micelles, to the synthetic mixture. A dense Si-network is formed around these micelles and after calcination a highly porous material, with pores $\geq$ 2 nm and surface areas of over 1000 $m^2/g$ is obtained. The most important examples of these materials are MCM-41 and MCM-48.

Another important milestone was the discovery of Santa Barbara Amorphous (SBA) materials in 1998 [5], which were prepared using non-ionic triblock copolymers ($EO_xPO_yEO_x$, a central hydrophobic polyoxopropylene, PO, chain surrounded by two hydrophilic polyoxyethylene, PE, chains) in acidic media as a template. The most remarkable difference between MCM and SBA materials lies in the wall thickness: while a typical MCM material has a wall thickness of around 1 nm, SBA-15 (the most known SBA material) has a wall thickness of 3-7 nm and is by consequence far more stable.

To make these materials even more attractive, it was desired to add organic functionalities R in the network, which would render better hydrothermal stability and access to functionality inside the materials structure. Multiple options for this are available, one could for example graft an organosilane on surface OH groups, leading to a surface bounded organic group. However these groups will not be homogeneously dispersed, may cause pore blocking and could be prone to leaching. A second possibility is co-condensation of an inorganic precursor (like TEOS, tetraethyl orthosilicate) with an organosilane. This one-pot synthesis will render a homogeneously dispersion of organic groups, but can't reach high loadings (20-40 mol% maximum) [6]. Finally, direct incorporation of organic groups in the structure is also an option, which doesn't show these important drawbacks. As can be seen in **Figure 1.1**, PMOs are such materials. While MCM and SBA materials were built as a network of $SiO_2$ molecules, this is not the case for PMOs. These new hybrid materials were synthesized like Ordered Mesoporous Silicas via a surfactant-templated supramolecular assembly process, but using organically bridged silica precursors ($(X)_3Si{-}R{-}Si(X)_3$ with R an organic group and X a methoxy/ethoxy group). As the used R group is highly interchangeable (only too big and flexible organic groups are not usable, as these will diminish pore-ordering [6]), large varieties of materials became available, with tailorable properties. It is by consequence evident that since the first PMO publications in 1999 by the groups of Ozin [7], Stein [8] and Inagaki [9] many different PMO types have been synthesized and studied.

## 1.2 The PMO synthesis

The synthesis of porous silica is performed via a sol-gel process, shown in **Figure 1.2** (for silica materials, for PMOs this process is analogous but with the previously described bridged

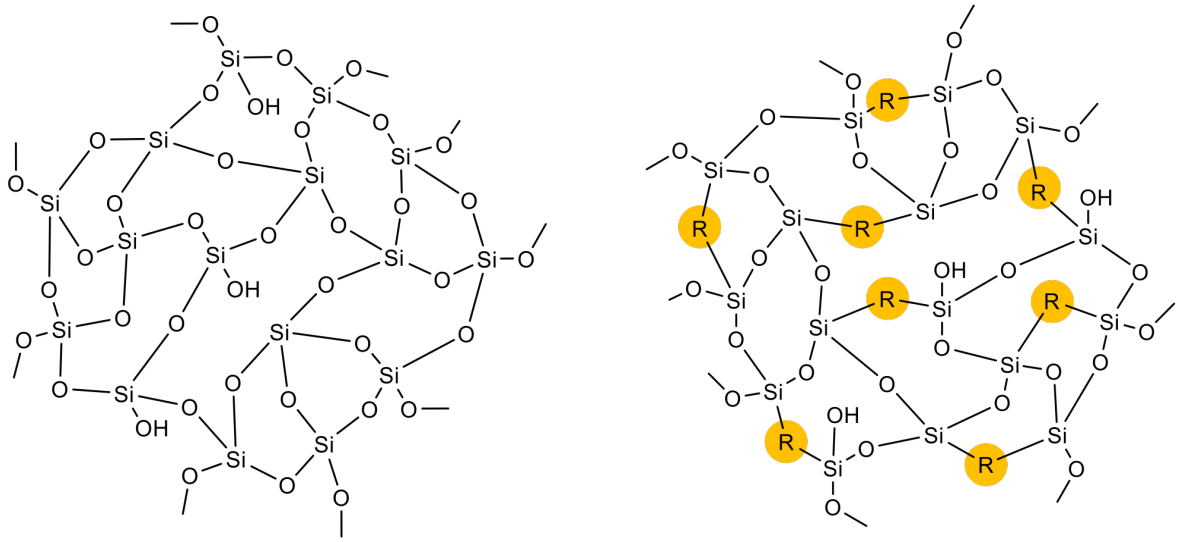

**Figure 1.1:** Chemical structure of a $SiO_2$-network (left) like in MCM materials and a $[RSiO_{3/2}]_n$-network with incorporated R-groups like in PMOs. [10]

silica precursor as starting material). This process consists of two steps, starting with a hydrolysis were Si−OH functionalities are formed, this can be either base or acid catalyzed. Subsequently, the formed Si−OH groups polymerize into a $SiO_2$ network via a condensation reaction [10], [6], [3].

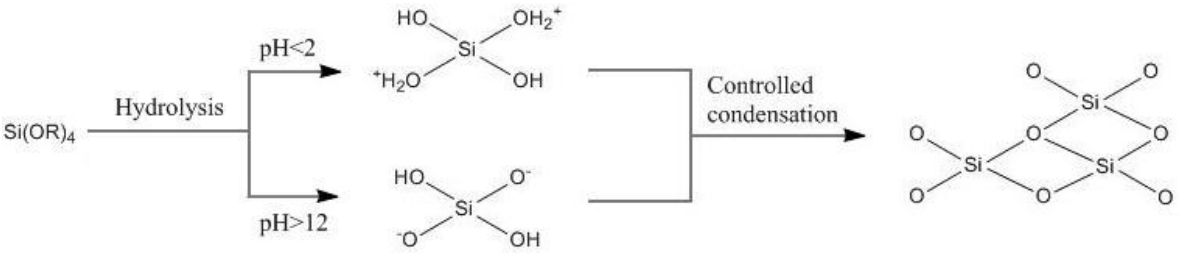


**Figure 1.2:** A schematic drawing of the sol-gel based synthesis of porous silica materials. Both hydrolysis and condensation steps are shown [6]

.

To yield ordered porosity, a template based system was developed. Surfactants are dissolved and form micelles, which act as liquid crystal templates. After formation of these micelles, the silica precursor is added and the above discussed sol-gel process is started. The silica material will polymerize around these micelles, which yields an ordered material, defined by the shape of the micelles. Features like porosity and wall thickness can be influenced by

appropriate choice of surfactants (anionic, cationic or non-ionic), pH, addition of metal salts and concentrations [6], [10].

## 1.3 PMO applications

As has been mentioned earlier, PMO properties can be optimized for multiple applications by changing the bridging organic group. Moreover, these materials are ordered, show a homogeneous distribution of functionality (which is not achievable with simple post-modificational grafting on the surface of Mesoporous Silicas), a high mechanical and hydrothermal stability, large pore sizes and high surface areas. In the following part, a short overview of some important PMO applications is composed, a more complete overview has already been made in multiple specialized reviews ([11–14]).

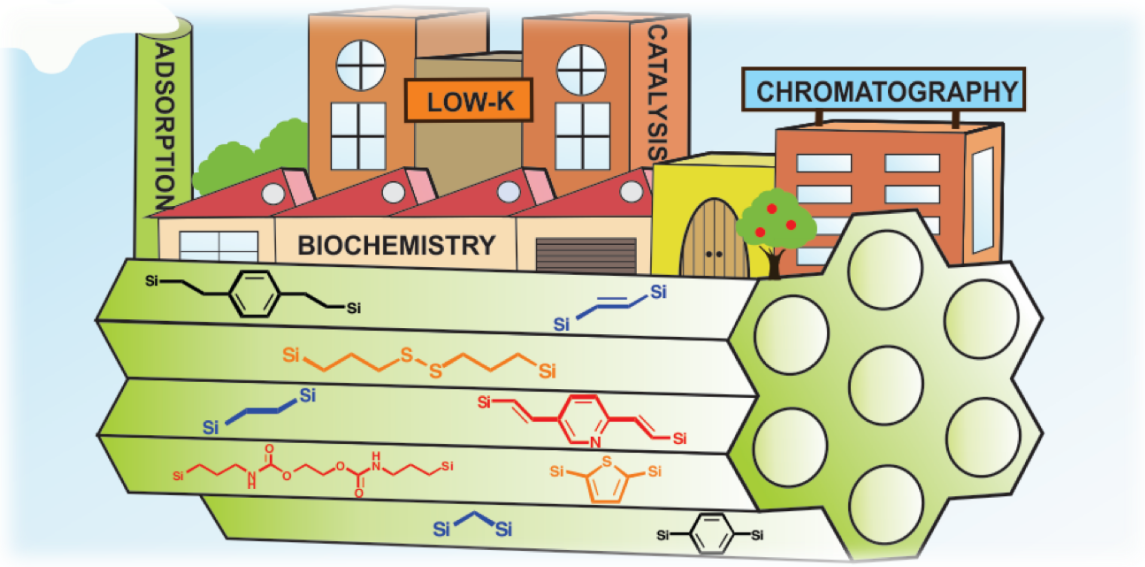


**Figure 1.3:** A schematic overview of some PMO applications [10]

### 1.3.1 Low k materials

For further development of microelectronic devices, downscaling is required. However, for this purpose, better isolating, low k (dielectric constant) materials are needed, to be able to place the interconnect wires closer without inducing RC-delay (Resistive-capacitive delay) [15]. To reach these ultra low k values (preferably below 2), the used material should be highly porous (as air has the lowest reachable k value of 1,0006 with a difference to vacuum that can be considered negligible) and extremely hydrophobic to avoid water adsorption (water has a high

k value of 80). As PMOs are highly porous hydrophobic materials, they are by consequence an important low k candidate. Furthermore, a high chemical and mechanical stability are desired, to withstand the sometimes severe conditions used in the manufacturing process [16]. By increasing the hydrophobicity of the material, one can further optimize the k value. This could be achieved by adding more organic character ($Si-(CH_2)_n-Si$ groups over $Si-O-Si$ groups), which also induces a higher mechanical stability [17]. Additionally one could perform a self-hydrophobizing thermal treatment or a hydrophobizing HMDS treatment [11].

### 1.3.2 Chromatographic phases

Chromatography routinely uses silica materials as packing material for the stationary phase, for their high mechanical strength, rigidity, large surface areas (which is beneficial for the retention) and modifiable surface. However these materials suffer from poor hydrothermal stability: at high pH or high temperature, commercially available columns are often not stable. Due to the increased hydrophobicity of PMOs in comparison to silica materials, they show improved hydrothermal stability. Furthermore, by use of the wide range in post-modifications available, one can attach a long alkylchain and make a very hydrophobic, stable stationary phase, perfect for reversed phase chromatography [18]. Another option is making stationary phases for chiral chromatography by adding chiral functionalities to the PMO [19]. However, there still remains a difficulty in making perfect spherical particles (which are needed to allow uniform packing of the column and thus reduce Eddy Diffusion) of the right size.

### 1.3.3 Adsorption

Adsorption of heavy metals, toxic compounds and gasses is a big environmental issue. Traditionally functionalized silicas and activated carbon are used for these processes, but PMOs (besides Metal Organic Frameworks (MOFs) and Covalent Organic Frameworks COFs) could be able to outperform these materials. Key to optimizing the materials for this process is increasing their stability during the adsorption process and making them reusable. Additionally the adsorption should be selective. A wide range of approaches, from which some are noted in the review by Walcarius *et al.* [20], can be used to tackle this problem. For example one could co-polymerize a PMO monomer with some metal complexes, subsequently etch the metal ions away and use the material as a selective adsorbent for the metal ion template, as cavities shaped as the corresponding metal complexes are formed in the material (molecular imprinting) [21].

When considering gas adsorption applications, it is also very important to look at the pore structure and interactions with present functionalities. Up to today, PMOs have not been

able to outperform zeolites or MOFs in this particular field [11]. Another interesting field of study could be adsorption of organic compounds, not only in the removal of toxic compounds but also in the sensing of dyes, pesticides etc.

### 1.3.4 Biomedical applications

PMOs could also be used as supports for a wide range of biomolecules, one of the first examples of such an adsorption process was published by Qiao *et al.* [22] for cytochrome c on an ethane PMO. Drug release [23] and protein refolding [24] properties have also been studied for this material.

### 1.3.5 Catalysis

Catalysis is until today the most wildely studied and important PMO application. Catalytic activity of PMOs can be achieved via an almost infinite amount of approaches. Here, the main catalytic functions with some examples are shortly discussed. A more detailed description of the catalysis performed in this work can be found in **Chapter 3**.

- Acid and base catalysis: By far the most incorporated acidic group has been the sulfonate group. This group could be added by direct sulfonation [25], post-modification [26], co-condensation [27] or grafting [28]. Base catalysis by PMOs is a much less studied process, but still multiple catalyzed reactions by PMOs have been reported. For example Knoevenagel [29] and Henry [29], [30] reaction catalysts, or catalysts for the $CO_2$ - epoxide coupling [31].

- Site specific catalysis: Different metals, like Ti [32], Sn [33], V [34], Nb [35], Al [36] and Cr [37] have been incorporated in the PMO framework, mostly catalyzing redox processes. As in general, activity per metal center increases with hydrophobic character, metal-substituted PMOs are usually highly active. Still leaching is often unavoidable for this type of materials [11].

- Heterogenized complexes: Organometallic compounds, however commonly very expensive and/or toxic, are very often used in catalysis. For this reason, heterogenization of these complexes on solid supports is very attractive. PMOs are one of these studied supports and many metal complexes have been incorporated in bridges or covalently attached to these materials (as has been done in this work). It is evident that leaching of these compounds should be avoided. A few examples of PMO supported complexes, resistant to leaching and with similar catalytic activities as their homogeneous counterparts are cited here ([38–41]).

- Bifunctional materials: Bifunctional PMOs are support materials bearing two different catalytic groups. The catalysts can have a cooperating effect, facilitating reactions needing different catalysts, or enabling one-pot reactions. The first bifunctional PMO was reported by Mehdi *et al.* [42], who created a material with acidic groups in the framework and basic groups in the pores.

- Enantioselective catalysis: Enantioselective catalysis has important applications in the preparation of chiral compounds in pharamceutical industry, therefore preparing new heterogeneous enantioselective catalysts is a very attractive topic. However it is often very challenging to obtain enantioselectivities and activities higher or comparable to those of homogeneous catalysts. Nevertheless, some attractive results have been obtained by tuning the ligand and PMO environment [43]. Furthermore, it could be concluded by Polarz *et al.* [44] that under steric conditions PMO catalysts can be very attractive due to cooperation between surface functional groups and the neighbouring catalytic center. Using this information, tuning of pore size, temperature and surface functional groups can lead to far better results than for homogeneous catalysts.

An important sidenote is the observed improved catalytic activity of PMO supported materials (compared to silica or some zeolite materials, per catalytic site) in organic reactions when water is involved [45], [46]. This is most likely due to the high hydrophobicity of the PMO support, causing increased diffusion of organics in to the pores.

## 1.4 The monoallyl ring PMO: an ultrastable support material

For most PMO applications, a high hydrophobic character is highly desirable. Although PMOs with simple bridges (ethane, methane, etc.) already show a high hydrophobicity and desirable properties, still these materials could be tuned to yield a higher hydrophobic character. By doing this, their mechanical and hydrothermal stability will increase [47]. As the organic groups, incorporated in the PMO framework, are responsible for this improved hydrophobicity, it is very attractive to further replace oxygen atoms by organic groups. This was achieved for the first time by Landskron *et al.* in 2003 [48], by building of an interconnected network of $[Si(CH_2)]_3$ rings (as can be seen in **Figure 1.4 B**) from the $[(EtO)_2Si(CH_2)]_3$ (1,1,3,3,5,5- hexethoxytrisilacyclohexane: HETSCH) precursor drawn in **Figure 1.4 A**. Note that, in comparison to the PMO drawn in **Figure 1.1** on the right, this structure has two organic groups bound to each Si instead of one. Different publications described the improved stability of this material ([18], [45], [49]). From these tests, it could be concluded that due to the improved hydrophobicity, contact with water is reduced and by consequence, the ma-

terial is very stable in acidic medium, basic medium (some degradation for pH 13 during 24 hours) and during (hydro)thermal treatment. For improved performance during mechanical treatment, an additional hydrophobization step needs to be applied [49].

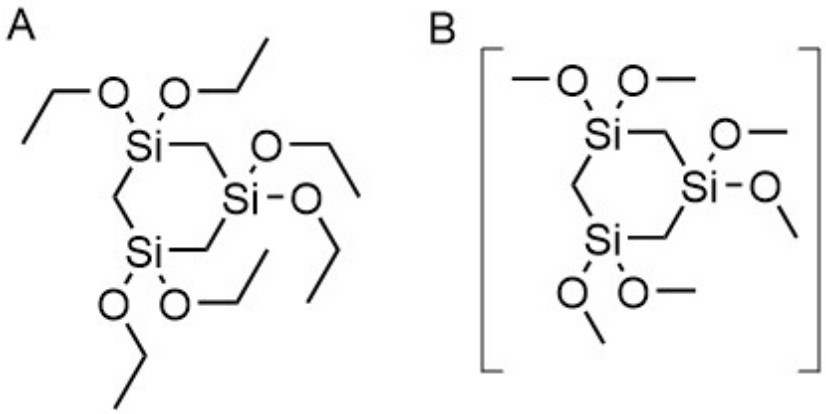


**Figure 1.4:** A) Chemical structure of the HETSCH Precursor B) Chemical structure of one Ring PMO subunit

An important disadvantage of this material, is the lack of reactive groups available for post-modification reactions. To overcome this problem, the HETSCH precursor was modified by Ide *et al.* [18] to yield a AHETSCH precursor (see **Figure 1.5**). By adding of a propene group to one of the bridging carbons (via a SN2 reaction with allylbromide, see **Chapter 2**) a reactive allyl function is created. This newly added group will be homogeneously spread over the material, dangling in the pores, which makes it easy to reach for further reaction.

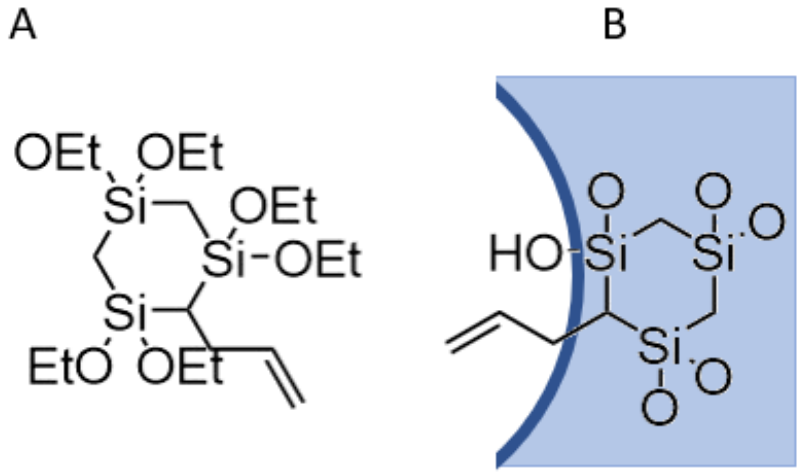


**Figure 1.5:** A) Chemical structure of the AHETSCH Precursor B) Schematic drawing of one monoallyl ring PMO subunit, with the allyl group dangling in the pores

# Chapter 2

# The monoallyl ring PMO

In this work, the previously discussed monoallyl ring PMO was chosen as the support material. Its exceptional stability was already presented in the previous chapter, but by the addition of an allyl group to the precursor, a remarkable reactivity has been achieved too. As can be seen in **Figure 2.1** a wide range of reactions, leading to a variety of functional groups, can be used. The thiol-ene click reaction is easily performed at high yields in different solvents, at mild conditions and with different thiol-bearing molecules. Due to these properties, it is an ideal post-modification reaction.

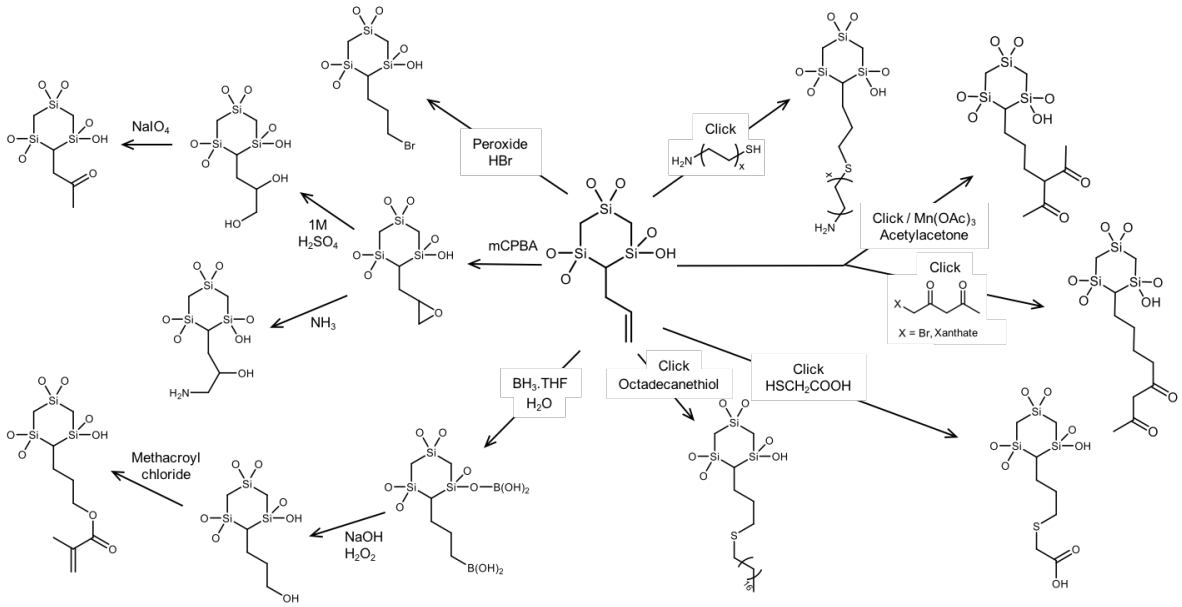


**Figure 2.1:** Overview of different post-synthetic modifications onto the monoallyl ring PMO [10]

## 2.1 The thiol-ene click reaction as a versatile tool

Since Sharpless *et al.* [50] defined 'click chemistry' for the first time in 2001 these reactions have received enormous amounts of attention. When striving for the environmentally friendly synthesis of complicated organic molecules these reactions are ideal tools. Click reactions are defined by high selectivities and rapid reaction with high conversion in mild conditions. Moreover reaction conditions should be simple and only non-harmful (or preferably none) byproducts can be formed. As the thiol-ene reaction, extensively discussed by Bowman *et al.* [51], satisfies these conditions while also being photoinitializable, it is a very attractive tool. Additionally, one has absolute control of reaction start (and stop) by simple UV irradiation of the mixture. The reaction shows a cyclic radical behaviour and can (in ideal circumstances) give yields close to 100 %. It has already been used to modify PMO precursors [52] as well as post-modify PMOs [53].

As the material selected for this work bears an allyl function, any thiol bearing molecule can be used to click onto the PMO. Furthermore, many desirable ligands are commercially available in carboxylic acid form. By consequence, it is very attractive to use a linker bearing an amine group to easily yield a stable amide bond. Keeping this in mind, cysteamine (see chemical structure in **Figure 2.2 A**) was selected as the linker. This molecule is commonly used as a drug [54], bears no other unused functional groups (to decrease risk of side reaction) and is easily commercially available. A slight disadvantage of this linker is that it has to be put under inert atmosphere (e.g. in a glovebox) for storage.

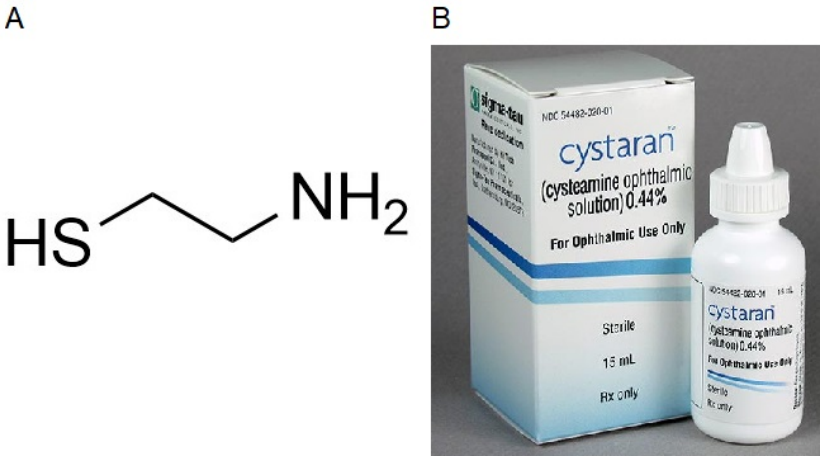


**Figure 2.2:** A) Chemical structure of the used cysteamine linker
B) Cysteamine used as a drug [55]

## 2.2 Synthesis and effect of influencing parameters

The network formation of PMOs is a complicated process with many influencing parameters: nature of the ligand, temperature, pH, stirring speed and time, and concentration of the compounds all show important implications in the formed material. A slight variation in one of these parameters can already yield a material with disordered pores, pores of an incorrect size, or a material with reduced stability. Moreover, optimized values are different from PMO to PMO (with different bridging groups). These processes have not yet been studied in detail for the monoallylring PMO, but Vercaemst *et al.* has carried out some comparable work on the ethylene and ethenylene PMOs [56], [57].

### 2.2.1 Synthesis of the PMO precursor

To obtain the AHETSCH precursor (2-allyl-1,1,3,3,5,5-hexaethoxytrisilacyclohexane), a nucleophilic ring addition of deprotonated HETSCH (1,1,3,3,5,5-hexaethoxytrisilacyclohexane) on allylbromide was performed. The procedure (described in **Appendix A** and shown in **Figure 2.3**) of Clerick *et al.* [45] was used.

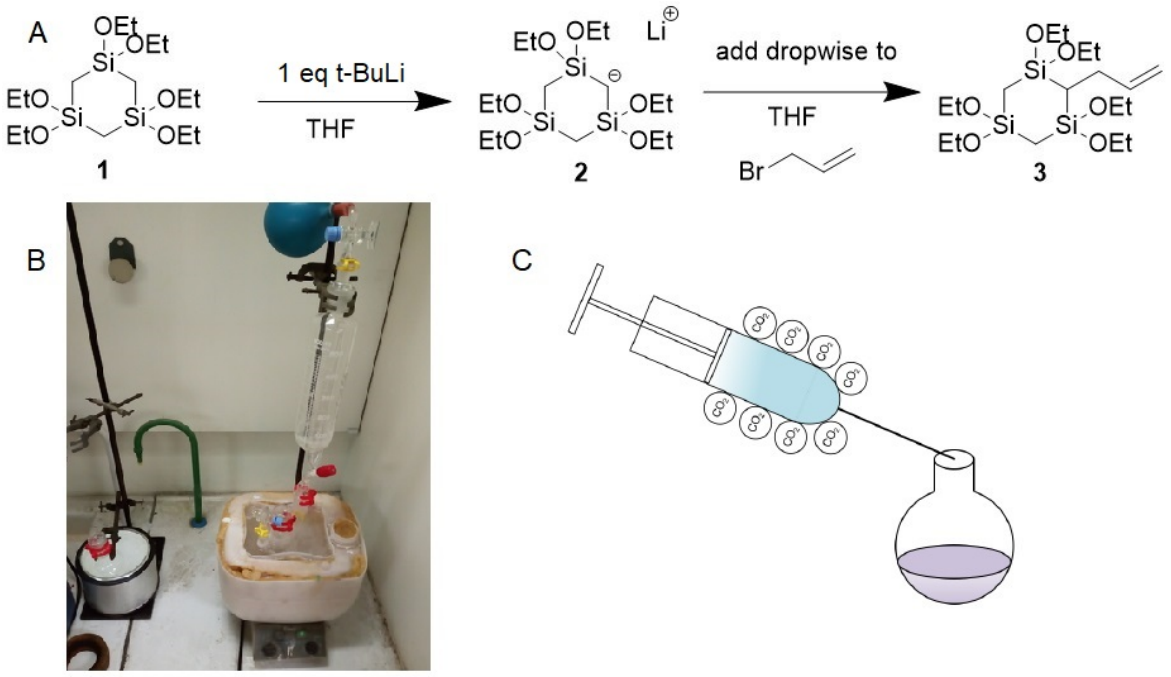


**Figure 2.3:** A) Reaction scheme of the AHETSCH synthesis, B) Picture of the reaction set-up, C) Schematic drawing of the $CO_2$ cooled HETSCH addition to allylbromide solution [10]

### 2.2.2 PMO network formation

In order to yield an ordered material, purification of the earlier synthesized precursor is needed [10]. Pure monoallyl ring precursor is obtained using column chromatography and confirmed via $^1$H NMR (Nuclear Magnetic Resonance) analysis. Still, the used synthesis is sensitive to changes, which is illustrated by the yielded reduction in ordering when trying to scale up the synthesis.

The synthesis, fully described in **Appendix A**, of the PMO material, consists of hydrolysis and self-condensation (as already described in **Chapter 1**) in acidified water. P123 (Pluronic P123) is used as surfactant and KCl is added in order to facilitate precursor-surfactant interactions. Afterwards the remaining surfactant is removed using acetone Soxhlet.

### 2.2.3 Post-synthetic modification: the thiol-ene click reaction

Using a thiol-ene click reaction, the desired ligands (in this project: porphyrin and picolinate) are attached onto the PMO, using a procedure fully described in **Appendix A**. To evade partial deterioration of the material due to remaining $NEt_3$ in the ligand precursor, a pH 7 phosphate buffer is added. The reaction is performed under Ar atmosphere, as airborne oxygen would promote termination of the reaction. In this chapter, addition of a simple cysteamine ligand to the PMO will be discussed to show the potential of this reaction.

## 2.3 Characterization

### 2.3.1 Characterization of the precursor

The synthesized precursor was characterized by $^1$H NMR and compared to the spectra of pure mono allyl ring precursor shown by Clerick [10] . The $^1$H NMR spectra of the pure precursor and synthesized precursor (before column separation) can be found in **Appendix C**. The $^1$H NMR spectra of the purified precursor can be found in **Figure 2.4**.

When calculating the yield of the reaction, the hydrogen b peak is the most important. When the intensity of the hydrogen f peak is set to one, hydrogen b should yield an intensity of 12 for pure monoallyl ring PMO precursor (as the monoallyl PMO precursor has 1 hydrogen at position f and 12 at position b). When a mixture is obtained, the relative intensity of the hydrogen b peak will be higher as unreacted ring precursor has no hydrogen f in its structure (but still 12 hydrogens at position b). So the yield can be calculated as $12/I_{Hb}$, which gave a yield of 38.5% for this synthesis, somewhat less than the result of Clerick [10]. Clearly, additional column purification was needed to remove the unreacted ring precursor.

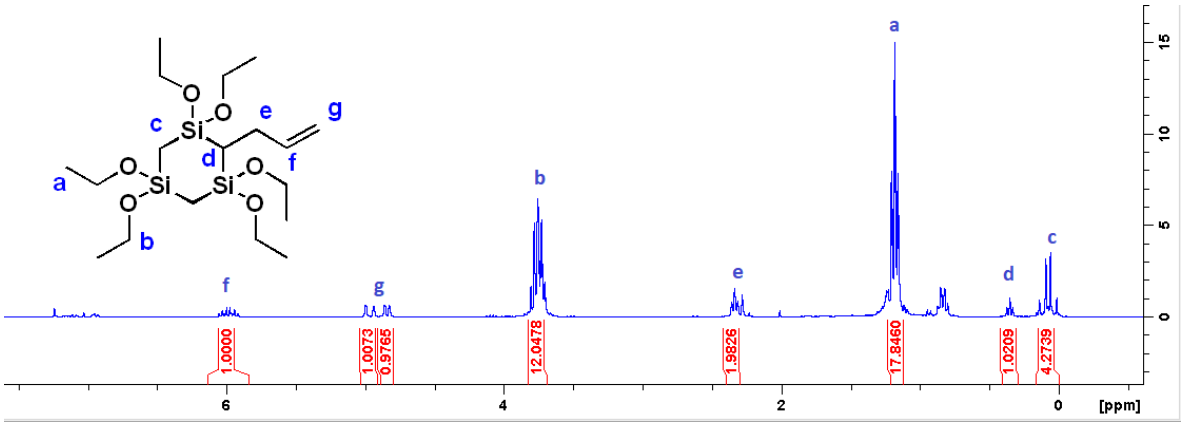


**Figure 2.4:** $^{1}$H NMR of the PMO precursor after column purification

The following peaks were assigned: (300 MHz, $CDCl_3$) $\delta$ = 5.98 (ddt, $J$=17.0, 9.9, 7.0, 1H, $CH_2CH$=$CH_2$, hydrogen f), 4.97 (d, $J$=17.0, 1H, CH=C$H_2$, hydrogen g), 4.84 (d, $J$=10.0, 1H, CH=C$H_2$, hydrogen g), 3.81 - 3.69 (m, 12H, OC$H_2$, hydrogen b), 2.37 - 2.27 (m, 2H, CHC$H_2$CH=$CH_2$, hydrogen e), 1.21 - 1.14 (m, 18H, $OCH_2CH_3$, hydrogen a), 0.35 (t, $J$=6.6, 1H, C$H$(Si)$_2$($CH_2CH$=$CH_2$), hydrogen d), 0.16 - 0.0 (m, 4H, SiC$H_2$Si, hydrogen c). A peak around 0.84 ppm remained unidentified.

The obtained spectrum matches almost perfectly with the previously mentionted literature spectrum. However, it has to be noted that all peak positions are downshifted by hundreds of a ppm in comparison with the literature spectrum. From the observed intensities, it can be concluded that the synthesis and purification of the precursor was successful.

### 2.3.2 Structural characterization

To show the sensitivity of this synthesis, a fully ordered material (monoallyl PMO) is compared to an attempt of upscaling the synthesis (PMO upscaled). The only difference between these synthesis batches is that for PMO upscaled all quantities were doubled (which kept the used molar ratios constant). In **Figure 2.5** and **Table 2.1** the $N_2$-sorption isotherms and data of both samples are shown.

**Table 2.1:** $N_2$-sorption data of monoallyl PMO, PMO upscaled and Cys PMO

| | Monoallyl PMO | PMO Upscaled | Cys PMO |
|---|---|---|---|
| BET Surface Area $(m^2/g)^a$ | 672 | 548 | 358 |
| BJH desorption pore volume $(cm^3/g)^b$ | 0.89 | 0.61 | 0.56 |
| BJH desorption pore width (nm)$^c$ | 5.2 | 5.0 | 5.0 |

[a]Specific surface area determined via Brunauer-Emmett-Teller theory [58]., [b]Pore Volume determined from adsorption branch at $P/P_0 = 0.99$, [c]Pore size calculated from desorption branch following Barrett-Joyner-Halenda theory [59].

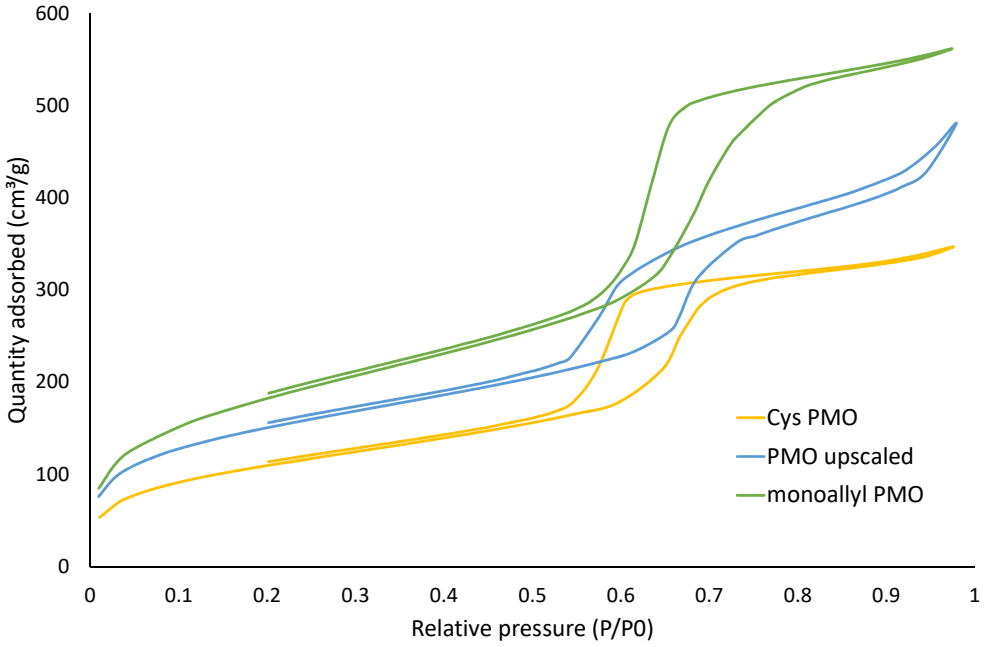


**Figure 2.5:** $N_2$-sorption isotherms of monoallyl PMO, PMO upscaled and Cys PMO

**Figure 2.5** shows a clear type IV isotherm with sharp H1 hysteresis for monoallyl PMO, indicating a highly ordered material with uniform cylindrical mesopores (like SBA-15). For PMO upscaled, the poresize distribution is broadened, with increased macroporosity observable. This is assigned to irregular and disordered areas in the material, which were proven to

have a significant influence on diffusion in the material [60]. Moreover, the internal surface area and desorption pore volume are somewhat lowered for PMO Upscaled ($S_{BET}$ = 548 $m^2/g$, $V_p = 0.61\ cm^3/g$ for PMO Upscaled while Monoallyl PMO shows $S_{BET} = 672\ m^2/g$), $V_p = 0.89\ cm^3/g$), while the pore width ($d_{p,BJH}$) stays constant at 5 nm. Consequently, the better structured Monoallyl PMO is the best choice as a support material.

Furthermore, the data for a clicked PMO (Cys PMO) is also included in **Figure 2.5** and **Table 2.1**. This PMO is prepared by clicking of cysteamine via the thiol-ene reaction discussed previously. By adding this reactive group, the mass of the PMO material increases, which causes a reduction in surface area and pore volume (as these are inversely proportional with the mass). Secondly, the decoration of the pore walls with these cysteamine groups also causes a decrease for $S_{BET}$ and $V_p$. Additionally, when studying the isotherm, no decrease in ordering can be observed, the pore width also stays constant.

Using PXRD, one intense (100) reflection is obtained at very low $2\theta$ values. As PMOs only exhibit pore ordening (and no structural ordening), this peak can be attributed to the pore diameter. The yielded d spacing of the (100) planes $d_{(100)}$ (using Bragg's fomula, **Formula 2.1**) will be indicative for the distance between two pores and can be used to calculate the cell parameter ($a_0$) (**Formula 2.2**) as P6mm 2D hexagonal ordering is observed. Subsequently, in combination with the BJH pore width, wall thickness (e, via **Formula 2.3**).

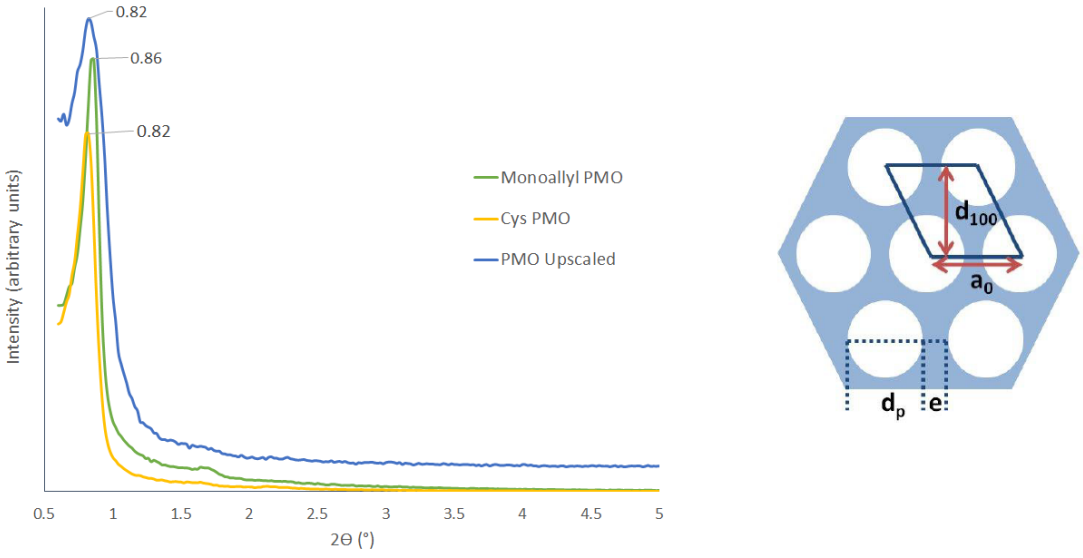


**Figure 2.6:** Left: PXRD diffractograms of monoallyl PMO, PMO upscaled and Cys PMO, the maximum of the (100) reflection peak is marked for each sample; Right: a scheme of the important parameters used in the calculation of the wall thickness [6]

$$n\lambda = 2d_{hkl}sin(\theta) \tag{2.1}$$

$$a_0 = \frac{2d_{100}}{\sqrt{3}} \tag{2.2}$$

$$e = a_0 - 0.95 * D_p \tag{2.3}$$

With $\lambda$ = the wavelength of the incident X-ray (1.54 Å) and n = 1 (first order reflection). The corresponding PXRD pattern and a scheme showing the important parameters is given in **Figure 2.6**.

When combining XRD and BJH data, the pore wall thickness can be calculated as 6.9 nm (monoallyl PMO) and 7.7 nm (PMO Upscaled and Cys PMO). These values are in the same range and thus it can be concluded that the synthesized PMO materials yield reproducible wall thicknesses which are preserved during post-modification. Furthermore, as these values are quite high for mesoporous silica, this can be attributed as one of the reasons of monoallyl PMOs exceptional stability.
Looking further into the spectrum of Monoallyl PMO, one can recognize a second, less intense, diffraction peak at $2\theta = 1.64°$, which originate of the (110) reflection. This peak is an extra indication of the improved ordering of this material over PMO Upscaled. In Cys PMO, however hardly visible, a slight increase in intensity is also noted at this $2\theta$ value.

### 2.3.3 Functional characterization

The formed PMO materials were all characterized using DRIFTS (Diffuse Reflectance Infrared Fourier Transform Spectroscopy), the obtained spectra for the unmodified monoallyl PMO and PMO upscaled are shown in **Figure 2.7**, together with the spectra for the click reacted Cys PMO.

When comparing the DRIFTS spectra, no clear difference between the two unmodified materials are observed. This means that while the structure is different, the desired functionalities are still present in the PMO upscaled sample. A broad C-H stretch vibration (2950-2800 $cm^{-1}$) can be observed as well as two Si-O-Si stretch vibrations (1200-1000 $cm^{-1}$ and 800-750 $cm^{-1}$ respectively). Moreover, three clear allyl peaks are found: an olefin C-H stretch (around 3070 $cm^{-1}$), a C=C stretch (around 1635 $cm^{-1}$) and an olefin out of plane CH deformation (around 895 $cm^{-1}$). Furthermore some residual $H_2O$ can be observed as a very broad peak (3700-3200 $cm^{-1}$). The modified PMO shows two clear additional peaks, a $NH_2$ bend around 1600 $cm^{-1}$ and a C-N stretch around 1500 $cm^{-1}$. When looking at the out of plane CH

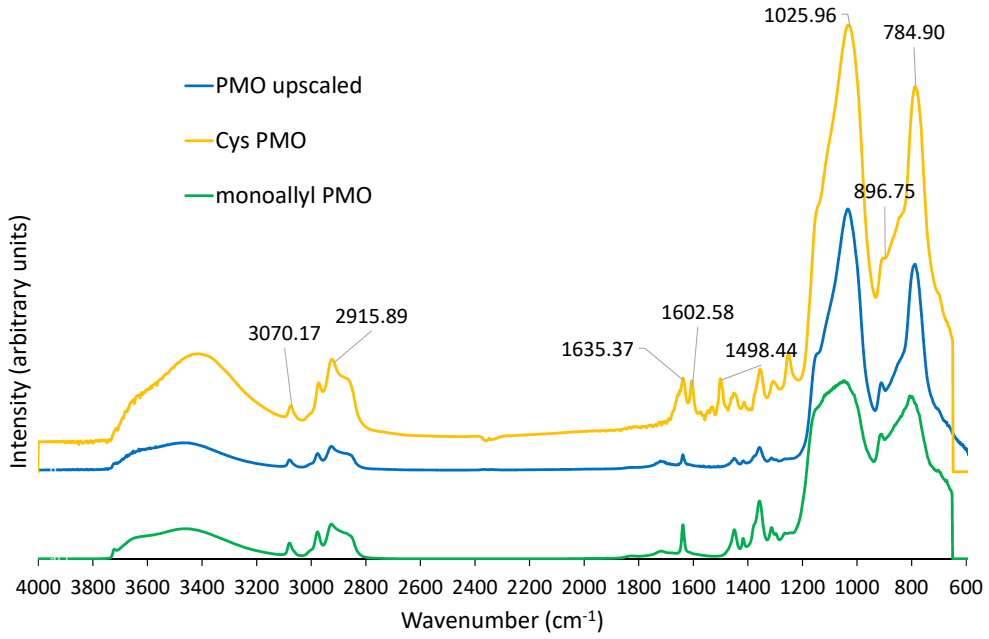


**Figure 2.7:** DRIFTS spectra of monoallyl PMO, PMO upscaled and Cys PMO

deformation, a decrease in relative intensity for the allyl peak is also noted in this sample (wich is less clear for the other 2 allyl peaks), caused by the coupling of cysteamine thiols to PMO allyl groups.

The functional loading of the prepared Cys PMO has been determined using CHNS elemental analysis. 100 mg PMO was coupled with 11 mg cysteamine linker (0.14 mmol) and UV treated for 1 hour. A loading of 0.74 mmol/g was obtained for N atoms, which are only present in the linker. By consequence, the loading of the linker was found to be 0.74 mmol/g, which is in agreement with the results obtained by Clerick *et al.* [45] for the same reaction.

# Chapter 3

# Covalent coupling of different ligands on the PMO: a uniform method

## 3.1 From simple to complex ligands

The wide range of reactions available to perform on PMOs also shows a slight disadvantage. Methods are often optimized for the application they are used in and are not always suitable for slightly different materials. Using a universal method could help avoiding additional expensive and time-consuming research on the linking of functional groups. Moreover, used ligands are often hard to compare as completely different modification routes are used. This problem is well illustrated by paragraph 4.1.1 of the review by Van der Voort *et al.* [11], were many different anchoring methods of $SO_3H$ groups onto PMO are shown. As structure and linker (and by consequence accessibility, stability and hydrophobicity) are different in all complexes, no relationship between catalytic activity and the amount of functional groups could be established by the authors. If functional groups would be attached onto the same support via the same linker (and process), one could eliminate the influence of these factors and study the behaviour of the heterogenized functional group more easily.

A potentially widely usable method was developed, inspired by Anzenbacher's *et al.* heterogenization of porphyrins [61], which could be used to couple a range of ligands bearing a carboxylic acid group on the monoallyl ring PMO. This method consists of a three step process, realizable in one day. First the acid is converted into the corresponding acyl chloride, afterwards an amide bond is formed with attachment of cysteamine and finally thiol-ene click chemistry is used to anchor the ligand onto the PMO, a schematic overview of this process is

presented in **Figure 3.1**. As a proof of concept, two different ligands (a simple and a more complex one) have been coupled to the PMO support and some potential applications have been studied.

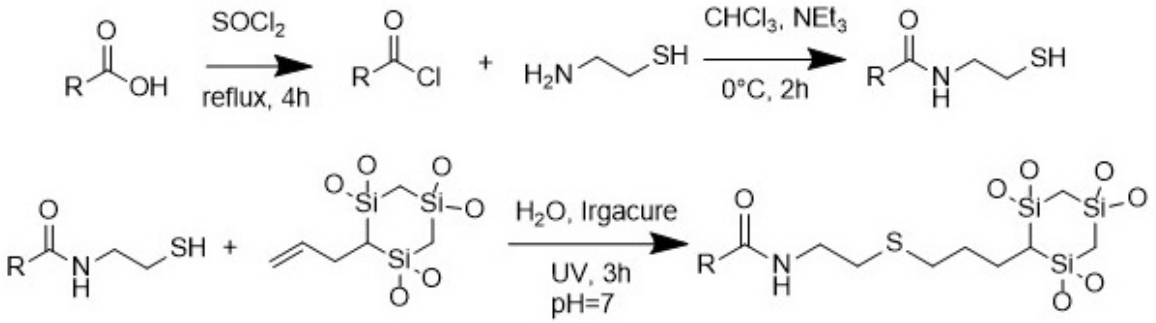


**Figure 3.1:** The developed method to anchor different kinds of ligands onto the PMO support

### 3.1.1 Picolinic acid

As pyridine is a widely used organic molecule, it has already been attached to a PMO material shortly after the first reports on PMO. Already in 2001, Burleigh *et al.* [62] developed a co-condensation route to make a pyridine PMO. Surprisingly, until today, only very few pyridine derivatives have been coupled to PMOs. Moreover, to the best of our knowledge, only one PMO material with a pyridin derivative dangling in the pores has been described [63]. Therefore, it was very interesting to anchor picolinic acid, a pyridin derivative with a carboxylic acid at the 2 position, to our PMO using our newly developed method.

In **Figure 3.2**, it can be seen that two neighbouring N atoms are created using this approach. This kind of complexes on PMOs have earlier been proven as good hydrogen bond donors [64], [65], complexing agents [63], adsorption agents [64], [66] and basic catalysts [65]. Our developed materials were tested as catalyst for the coupling of $CO_2$ and epoxides (which has already been reported with a comparable material [66]) and as luminescent materials (by coordination of different visible emitting lanthanides).

### 3.1.2 Porphyrins

Porphyrin complexes have already proven to be very attractive in a remarkable range of applications. The existence of these complexes is for example vital for biological functions as oxygen, solar energy and electron transfer [67], [68], but their uses can be elaborated to be as

diverse as magnetic materials [69] and environment sensors [70]. Due to their important role in photosynthesis, porphyrins have also drawn large attention for applications in solar cells [71] and photodynamic therapy [72]. Namely these complexes are able to strongly absorb light from the UV over the visible range to the NIR (perfect for photodynamic therapy due to the large penetration in the body of these wavelengths). Combination with the ability to easily bind $Ln^{3+}$ ions with their tetraaza macrocylic core makes these structures also perfect ligands for near-infrared (NIR) emitting lanthanides [73]. Moreover porphyrin ligands have also been reported as excellent catalysts in a wide range of reactions [74] including the coupling of epoxides and $CO_2$ [75].

A variety of these porphyrin complexes are commercially available, but all are expensive. Moreover they are time-consuming to make and difficult to isolate and handle properly. It is by consequence evident that heterogenisation of these complexes would be very attractive. Polymer supported porphyrin complexes have been reviewed by Leadbeater *et al.* [76] and also some porphyrin bridged PMOs have been developed [77–79]. However, to the best of our knowledge, no PMO with dangling porphyrin functions has been studied yet. Here these kind of materials (see **Figure 3.2**) are synthesized for the first time.

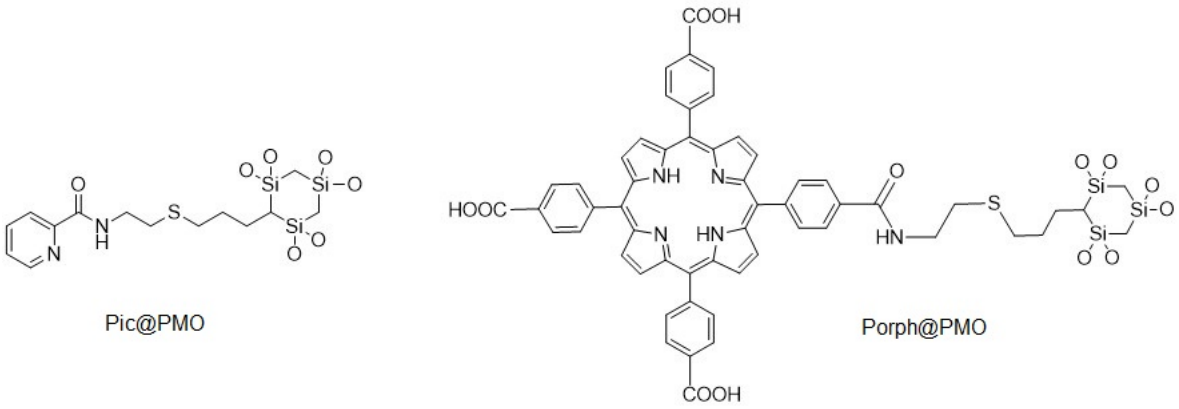


**Figure 3.2:** Chemical structure of the developed materials: picolonic acid coupled onto PMO (Pic@PMO) and porphyrin coupled onto PMO (Porph@PMO)

## 3.2 Synthesis

A uniform method has been developed to potentially couple a wide range of ligands onto the monoallyl ring PMO. Moreover the method is easy, fast and generates almost no by-products.

### 3.2.1 Chlorination of the ligand

In order to generate a stable amide bond, the carboxylic acid on the ligand had to be converted to a reactive acid chloride. This was achieved by refluxing of the ligand in $SOCl_2$ for 4 hours. The white picolinic acid yielded a dark brown acid chloride, the dark purple porpyrin resulted in a dark green acid chloride.

### 3.2.2 Amide bond formation

To avoid reactions of cysteamines free thiol groups with the ligands acid chloride groups and subsequent overreaction, the cysteamine solution was added dropwise to the ice-cooled ligand solution. Moreover to prevent radicals from forming (which would have resulted in disulfide bridge formation) the reaction was executed in Ar atmosphere and covered with Al foil. After reaction, the picoline product was purified using a literature found process,[80] via washing steps with $NaHCO_3$ and brine, to remove leftover $NEt_3$ from the mixture. For the porphyrin mixture this step was not needed. Finally, a tan (picolin) or dark purple (porphyrin) powder was obtained.

### 3.2.3 Coupling on the PMO

To evade deterioration effects on the PMO due to some leftover $NEt_3$ in the mixture, a pH = 7 phosphate buffer has been prepared. Furthermore, if in the previous step some thioesters were formed, these would rapidly rearrange to amides in these conditions via native chemical ligation [81]. The reaction was performed under Ar to evade termination by radical reaction with $O_2$. Reaction time was altered depending on stirring and desired loading to drive the reaction to completion. Afterwards unreacted product was removed with Soxhlet extraction using acetone.

## 3.3 Characterization

### 3.3.1 Coupling of picolinic acid

The amide coupling of picolinic acid and cysteamine to N-(2-mercaptoethyl)picolinamide (PicCys) was followed using $^1H$ NMR analysis (see **Figure 3.3**). The aromatic shifts after synthesis are visibly shifted and two new peaks resulting from the coupled cysteamine carbons have appeared. Some other peaks could also be assigned, acetone resulting from incomplete drying of the tube in the picolinic acid spectrum and water and $NEt_3$ which were not completely washed out in the PicCys spectrum. A detailed assignment of both spectra can be found in **appendix C**.

As the resulting $^1$H NMR spectrum of PicCys perfectly matches the spectrum found by Gale *et al.* [80], the reaction was concluded to be successful. Moreover, our method used shorter reaction times and didn't need addition and removal of a protecting group.

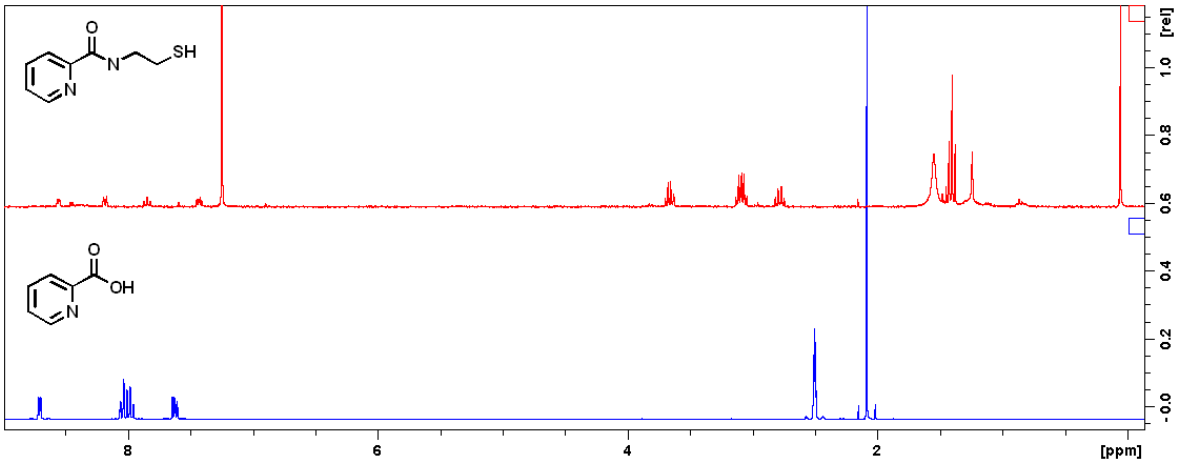


**Figure 3.3:** $^1$H NMR of Picolinic Acid (blue, in DMSO) and PicCys (red, in $CDCl_3$)

The FTIR spectra of an unmodified PMO (Monoallyl PMO), the synthesized ligand (PicCys) and 2 coupled materials are plotted in **Figure 3.4**. Both Pic@PMO 1 and Pic@PMO 3 were click reacted using the above described procedure, but purification was performed differently. Pic@PMO 1 was filtered and washed with $H_2O$, subsequently it was stirred in heated water (65 °C), finally to be filtered and washed again (the procedure used by Clerick *et al.* [45]). Pic@PMO 3 was filtered and washed with acetone and water and thereafter treated with Soxhlet extraction using acetone.

When comparing the spectra of the unmodified PMO and reacted materials, the first thing to notice are the allyl peaks. A reduction in intensity for the olefin C-H out of plane deformation (908 $cm^{-1}$) is hard to notice, but the olefin C-H stretch around 3077 $cm^{-1}$ and especially the C=C stretch in the zoomed part (1637 $cm^{-1}$) are clearly reduced in intensity. It can be concluded that this group indeed reacted and coupled some ligands on the PMO. The free amide (PicCys) showed a broad and intense amide peak (C=O stretch) around 1668 $cm^{-1}$, while for Pic@PMO 1 and Pic@PMO 3 a much sharper peak around 1598 $cm^{-1}$ appeared. This is a value lower than the amide C=O range, which points to increased mass of the molecule (slower vibrations) and thus successful bonding. Furthermore, it's observed that a simple water washing step is not sufficient to remove all uncoupled amide, as Pic@PMO 1 still shows an unbound amide peak. However, no peak around 1668 $cm^{-1}$ is observed for Pic@PMO 3, so Soxhlet extraction was proven to be an efficient method for removing all

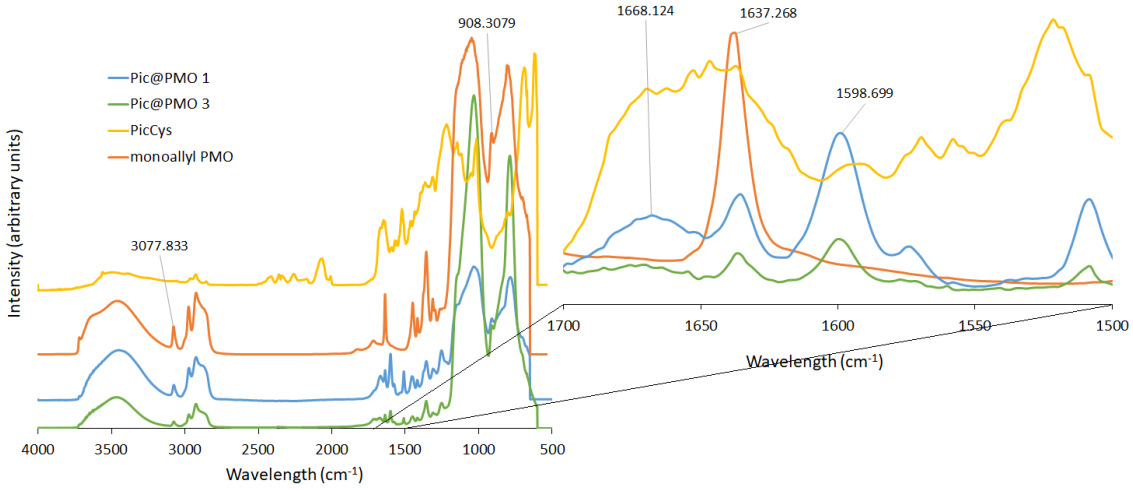


**Figure 3.4:** FTIR spectra of PicCys, Monoallyl PMO, Pic@PMO 1 and Pic@PMO 3, a zoom of the 1700-1500 $cm^{-1}$ region has been added

unreacted amide from the mixture. Finally, when comparing allyl and amide peak relative intensities, it's clear that both samples reacted with a majority of the allyl groups but still a significant amount of allyl groups remained unreacted. This means that most likely not all allyl groups in the PMO are reachable for post-modification with big ligands [10]. Still a significant part of the allyl groups remains unreacted, something which might be solved by increasing reaction time or stirring during the click reaction.

Influence of the click reaction on the porous structure of the PMO could be tested using BET analysis. Measurements were performed before and after modification, for Pic@PMO 1 and Pic@PMO 3. The measured isotherms are shown in **Figure 3.5**, data is presented in **Table 3.1**

**Table 3.1:** $N_2$-sorption data of Pic@PMO 1 and Pic@PMO 3 before and after modification

| | Pic@PMO 1 before | Pic@PMO 1 after | Pic@PMO 3 before | Pic@PMO 3 after |
|---|---|---|---|---|
| $S_{BET}(m^2/g)^a$ | 558 | 390 | 548 | 565 |
| $V_p(cm^3/g)^b$ | 0.93 | 0.63 | 0.61 | 0.63 |
| $d_{p,BJH}(nm)^c$ | 5.6 | 5.0 | 5.0 | 5.1 |

[a]Specific surface area determined via Brunauer-Emmett-Teller theory [58]., [b]Pore Volume determined from adsorption branch at $P/P_0 = 0.99$, [c]Pore size calculated from desorption branch following Barrett-Joyner-Halenda theory [59].

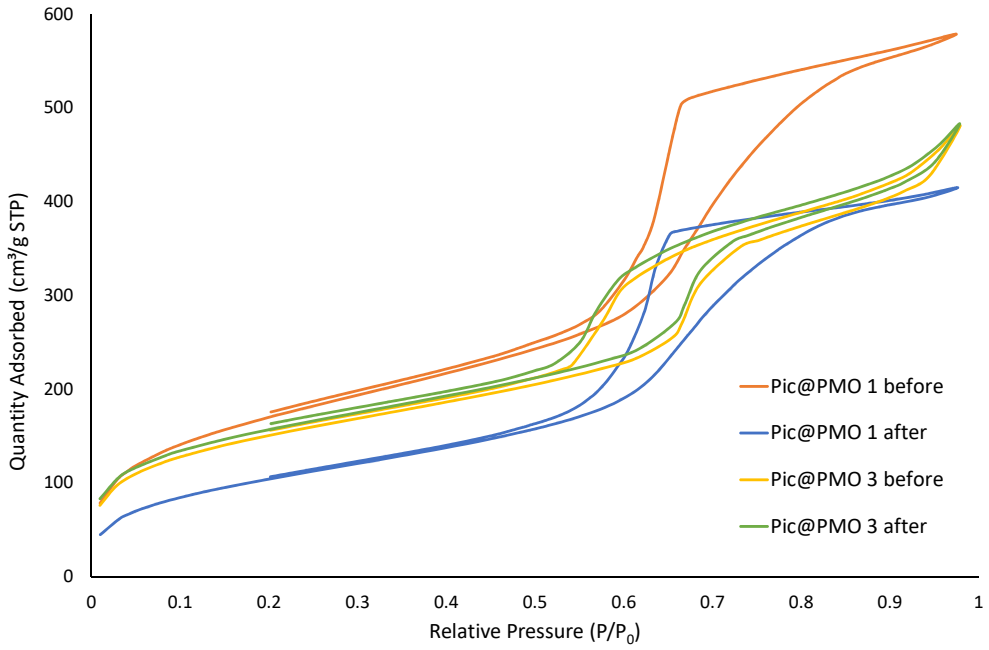


**Figure 3.5:** $N_2$-sorption isotherms of Pic@PMO 1 and Pic@PMO 3, before and after modification

When analyzing the isotherms, the first thing to note is that the clear type IV isotherm with sharp H1 hysteresis (or broadened pore size distribution for Pic@PMO 3) is preserved during modification of the material. While for Pic@PMO 1 the quantity adsorbed is clearly reduced, the shape of the isotherm is retained. Pic@PMO 3 did not even show a significant difference from the unmodified material. This clear difference in amount of adsorption is further noted when looking at the quantitative data, where surface area, pore volume and pore size are decreased for Pic@PMO 1 and retained for Pic@PMO 3. The observed decrease in pore size for Pic@PMO 1 indicates ligands adsorbed on the pore walls, which were not detected for Pic@PMO 3. Still, this effect is not enough to explain the invariant isotherm during click reaction for Pic@PMO 3. The most probable explanation for this phenomenon is a low ligand loading, lower than $\sim$ 10 %, which is in the error range of this measurement.

Combining this with PXRD data of the samples (the patterns are shown in **Figure 3.6**), the wall thickness of the different samples could be measured. By looking at the position of the (100) peak, it's readily observable that the basic material of Pic@PMO 1 had a $d_{(100)}$

(and thus most likely a wall thickness) larger than that of Pic@PMO 3, as the peak $2\theta$ value is shifted to lower angles. A wall thickness of 8.1 nm for Pic@PMO 1 before and 7.7 in Pic@PMO 3 before could indeed be calculated, using the pore widths of respectively 5.6 and 5 nm. This means that the observed increase in $d_{(100)}$ is a combination of increased pore width and wall thickness. However, when looking at the BJH results, Pic@PMO 1 after modification showed a much lower pore width than the unmodified material (from 5.6 nm to 5.0 nm), while the $d_{(100)}$ remained roughly the same. Indeed a wall thickness of 9.4 nm could be calculated for this sample, an increase of 1.3 nm in comparison with the unmodified material. This is an extra indication that indeed adsorbed material will be present on the pore walls, as no extra $SiO_2$ network formation could have happened during the modification reaction. For Pic@PMO 3 this is not the case, as even a slight, but not significant, reduction in wall thickness from 7.7 to 7.3 nm is observed.

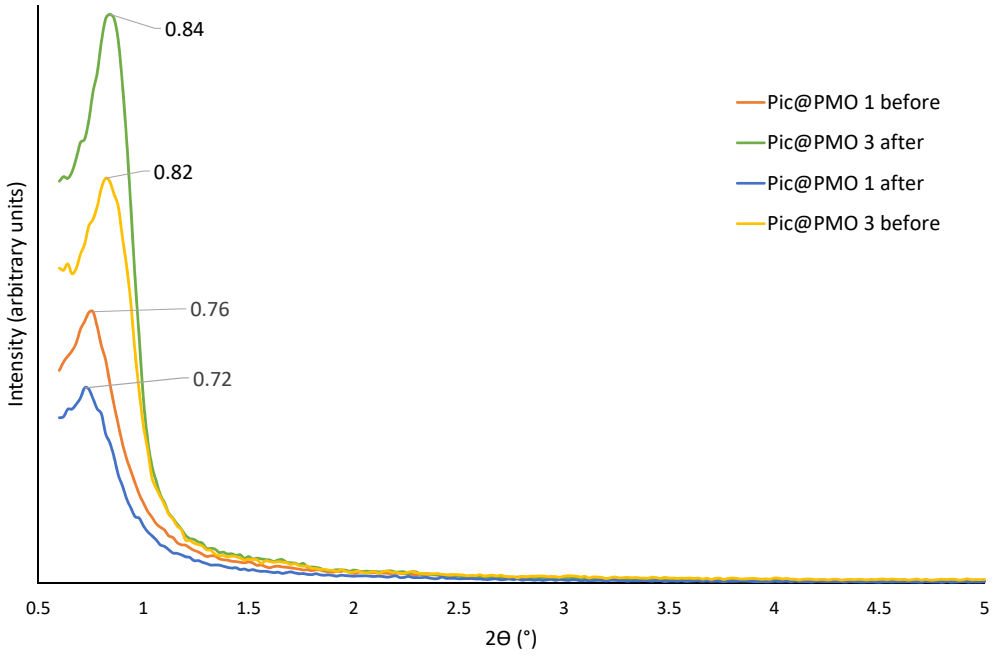


**Figure 3.6:** PXRD diffractograms of Pic@PMO 1 and Pic@PMO 3 before and after analysis, the maximum of the (100) reflection peak is marked for each sample

Using CHNS analysis, the molecular loading of picolinic acid on the PMO was determined. The measured weight-percentage of the nitrogen peak was used, as the sulphur peak was too

broad to determine accuratly. Using this, one could calculate a loading of 4.14 mmol/g N in Pic@PMO 1 and 0.73 mmol/g N in Pic@PMO 3. As each picolin ligand possesses two N atoms (**Figure 3.2**), this yields ligand loadings of 2.07 and 0.37 mmol/g. However, it is presumed that most of the detected nitrogen in Pic@PMO 1 originates from the adsorbed ligands. When comparing this result to the loadings of last chapter, it is clear that much lower loadings are obtained for Pic@PMO 3. As this result corresponds to a ligand mass percentage of 6.6 %, this explains the invariant isotherm during click reaction. Still, for preparation of this sample, an excess of PicCys has been used, as 150 mg of PMO was allowed to react with two times 40 mg PicCys (0.21 mmol). It could by consequense be concluded that click reaction with this bigger ligands is less efficient, with limited accessibility of allyl groups for these bigger ligands as one possible explanation for this.

### 3.3.2 Coupling of porphyrin

For coupling of the porphyrin with cysteamine to 4,4',4"-(20-(4-((2-mercaptoethyl)carbamoyl) phenyl)porphyrin-5,10,15-triyl)tribenzoic acid (PorphCys), the same procedure has been followed as for the picolin amide coupling. Again, the coupling has been tested using $^1$H NMR analysis (**Figure 3.7**, separate spectra can be found in **appendix C**), which suggests coupling, but no absolute certainty could be obtained.

From the observed splitting (and shift) of the aromatic peaks between 8.2 and 8.8 ppm, one could conclude that some of the benzoic acid groups are modified. When looking at the relative intensities of the aromatic peaks, it seems that indeed 1 aromatic unit is modified and 3 are unmodified, as was planned. A broad amide peak around 7 ppm is also observed, suggesting successful amide coupling. However, no cysteamine $CH_2$ peaks could be assigned. Furthermore, two very intense peaks, resulting from remaining $NEt_3$ are also observed.

Coupling of porphyrin to Porph@PMO has been checked using FTIR analysis, presented in **Figure 3.8**. First thing which should be noticed (and a clear indication of successful coupling) is that the Porph@PMO 1 spectrum shows characteristics of both PorphCys and Monoallyl PMO spectra. When looking at the zoomed in region, a reduced allyl C=C stretch peak (1637 $cm^{-1}$) is observed for Porph@PMO 1, indicating efficient thiol-ene click reaction. However, as the pure porphyrin already shows 3 C=O peaks (a very broad one around 1700 $cm^{-1}$, and sharper peaks at 1604 and 1564 $cm^{-1}$), it is very hard to detect the amide peak. The most plausible option is that the 1604 $cm^{-1}$ peak results from the amide, as its relative intensity is much higher for PorphCys and Porph@PMO 1, coinciding with a porphyrin C=O peak. Furthermore, the broad porphyrin peak around 1700 $cm^{-1}$ (most likely corresponding with the carboxylic acid) is much sharper (and shifted to 1722 $cm^{-1}$) for PorphCys and Porph@PMO

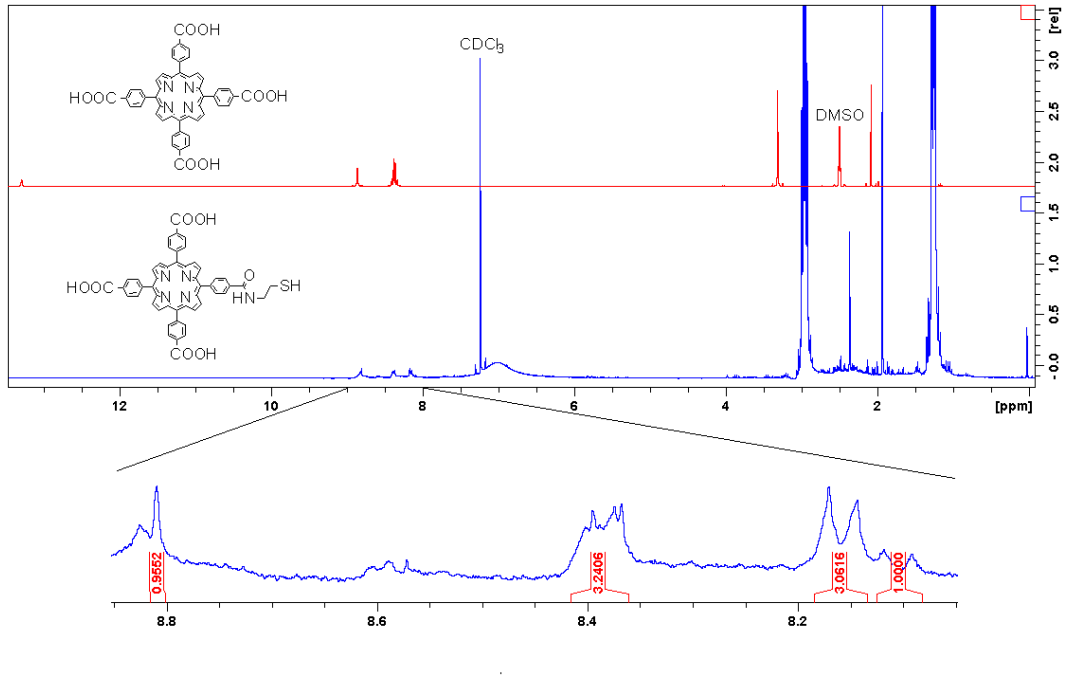


**Figure 3.7:** $^{1}$H NMR of unmodified porphyrin (blue, in DMSO) and PorphCys (red, in $CDCl_3$), a zoom at the aromatic region of PorphCys is included

1, indicating modification of these groups. Finally, a small peak just below 1800 $cm^{-1}$ is detected for PorphCys, which is attributed to the formed acyl chloride, surprisingly this peak is not observed for Porph@PMO 1. Possibly the acid chlorides are reacting with the water used as solvent in the click reaction.

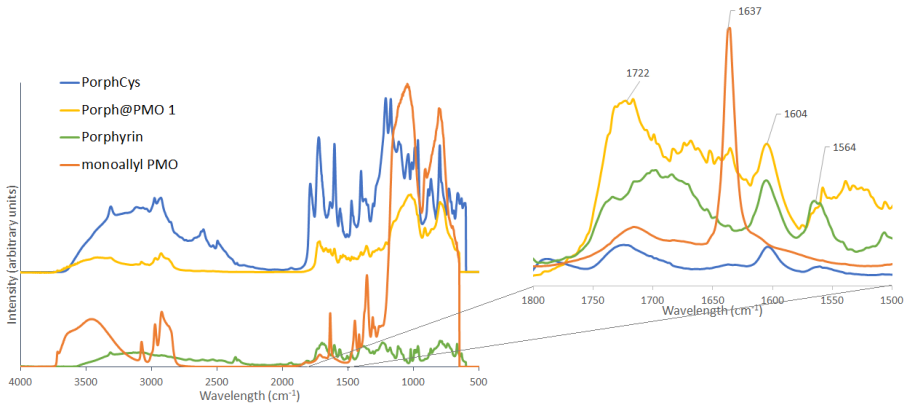


**Figure 3.8:** FTIR spectra of Porphyrin, PorphCys, Porph@PMO 1 and Monoallyl PMO. A zoom at the 1500-1800 $cm^{-1}$ region has been provided

Using $N_2$-sorption and PXRD, the structural properties of Porph@PMO 1 could be analyzed, spectra are shown in **Figure 3.9** and calculated data presented in **Table 3.2**.

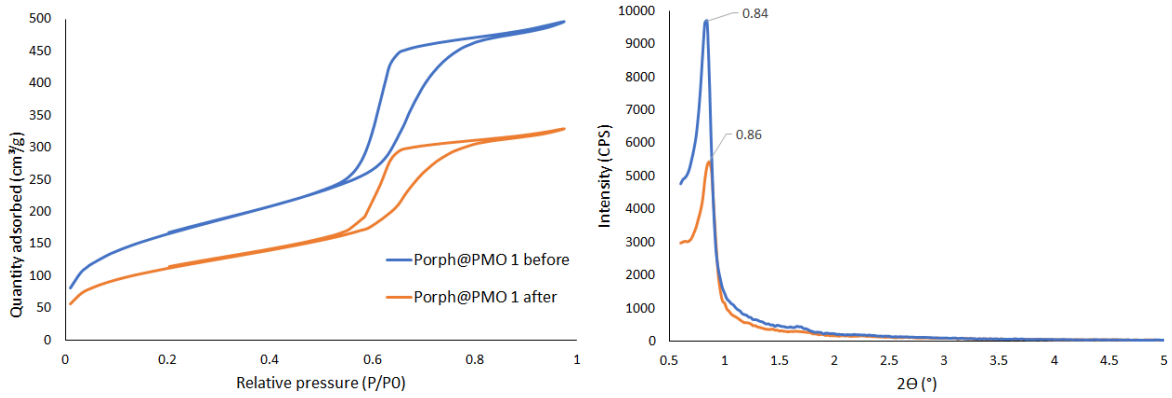


**Figure 3.9:** Left: $N_2$-sorption isotherms of Porph@PMO 1, before and after modification; right: PXRD patterns of Porph@PMO 1 before and after modification, the maximum of the (100) peak is indicated

**Table 3.2:** Structural data of Porph@PMO 1 before and after modification

| | Porph@PMO 1 before | Porph@PMO 1 after |
|---|---|---|
| $S_{BET}(m^2/g)^a$ | 605 | 406 |
| $V_p(cm^3/g)^b$ | 0.78 | 0.52 |
| $d_{p,BJH}(nm)^c$ | 5.1 | 5.1 |
| $d^d_{(100)}$ | 10.5 | 10.3 |
| $a^d_0$ | 12.1 | 11.8 |
| $t^d$ | 7.3 | 7.0 |

[a]Specific surface area determined via Brunauer-Emmett-Teller theory [58]., [b]Pore Volume determined from adsorption branch at $P/P_0 = 0.99$, [c]Pore size calculated from desorption branch following Barrett-Joyner-Halenda theory [59]., [d] the d spacing of the (100) planes, cell parameter and wall thickness were calculated combining pore volume and XRD results

When analyzing the obtained spectra, it's concluded that, as expected, introduction of the porphyrin ligand doesn't influence the PMO structure. The type IV isotherm with sharp H1 hysteresis is preserved during the reaction and the $d_{(100)}$ peak shows no significant shift in value. Still, the $d_{(110)}$, indicating high symmetry, which is slightly visible in the unmodified material, has disappeared in the modified material. As not all allyl groups are free for reaction

this reduction in symmetry was expected.
Continuing with the calculated data, a big reduction in surface area and pore volume for the modified material was noted, while no significant change in pore size and wall thickness could be observed. Once more this is an indication for successful binding of the porphyrin ligand on the PMO and sufficient washing, as no adsorbed ligands are present anymore.

One more indication for successful binding of the porphyrin on the PMO is given in **Chapter 5, Subsection 3.2**). Here the excitation and emission spectra of Porph@PMO 1 are plotted, showing typical porphyrin luminescence behaviour. Moreover, relative intensities and small shifts (especially for the porphyrin Q bands) are observed, which further indicate covalent coupling of the porphyrin.

Finally, using CHNS analysis, the molecular loading of the porphyrin ligand on the PMO was calculated. Like in Pic@PMO, the nitrogen value was used to calculate the ligand loading. A nitrogen loading of 3.08 mmol/g could be obtained, corresponding to 0.61 mmol/g porphyrine ligands (as each ligand has 5 N atoms, see **Figure 3.2**), or a very high ligand mass percentage of 52.23 %. As $\sim$ 0.13 mmol porphyrin was used on 120 mg, this is a value that is quite in agreement with the obtained loading for Cys PMO.

### 3.3.3 Stability and morphology of the materials

The stability of the materials has been tested using TGA (Thermal Gravimetric Analysis) and DTA (Differential Thermal Analysis). The TGA spectrum is presented in **Figure 3.10**, while the DTA spectrum can be found in **Appendix C**. It could be observed from the spectra that both materials lose some coordinated solvent (most likely water) in the 0-100 ℃ range. In higher temperature ranges, the materials are perfectly stable until 200 ℃, Pic@PMO 3 starts to lose mass around 225 ℃ while for Porph@PMO 2 the inflection point was observed to be around 275 ℃. For Pic@PMO 3 a mass loss of $\sim$ 20 % was noted, for Porph@PMO 2 mass loss was around 35 %. Most likely this was due to detoriation of the attached ligands, especially for Porph@PMO 2 (31 m%) this mass loss corresponds very well with the observed ligand loading. The observed mass loss for Pic@PMO 3 was much higher than the ligand loading (6.6 m%), so most likely the allyl bonds also detoriate at this temperature, rendering the total 20 % mass loss. Finally, between 400 and 500 ℃, mass loss stops and the remaining material stays stable untill the end of the measurement at 800 ℃. It could thus be concluded that the silica support is stable at very high temperatures.

Using Scanning Electron Microscopy (SEM), the morphology and size of the developed materials was studied. It could be observed from **Figure 3.11 A and B** that Pic@PMO 3

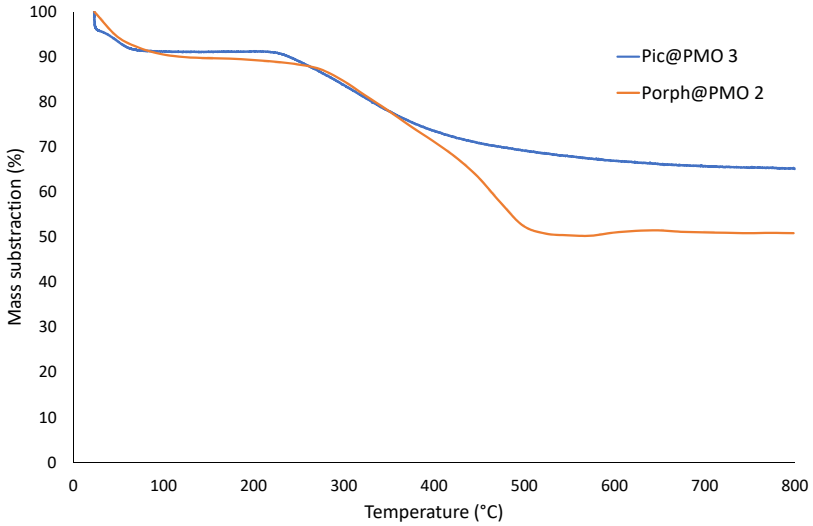


**Figure 3.10:** TGA spectra of Porph@PMO 2 and Pic@PMO 3

(synthesized using the perfectly ordered Monoallyl PMO) forms rod-shaped particles, like observed for the pure material by Clerick *et al.* [45]. When making an estimation of the size of these rods, the width is between 2 and 7 µm, while the length could easily range from 50 to 100 µm.

For Porph@PMO 2 (**Figure 3.11 C and D**), very similar rods are obtained, but mixed with sphere-like structures up to 20 µm in size. Most likely these spherical structures, which look much less ordered (when comparing the zoomed pictures of **Figure 3.11 B and D**), result from the less developed starting material PMO Upscaled.

## 3.4 Conclusions

A general method to couple carboxylic acid derivatives on the monoallyl ring PMO has been developed. A three step procces, consisting of acid chloride formation, amide coupling with cysteamine and thiol-ene click reaction on the PMO was used. These three steps are all short and easy, needing hardly any purification.

The developed method was tested for picolinic acid and tetra benzoic acid porphyrin attachment. Steps were analyzed using $^{1}$H NMR and the resulting PMO material has been functionally characterized by FTIR and structural charachterized by $N_2$-sorption and XRD,

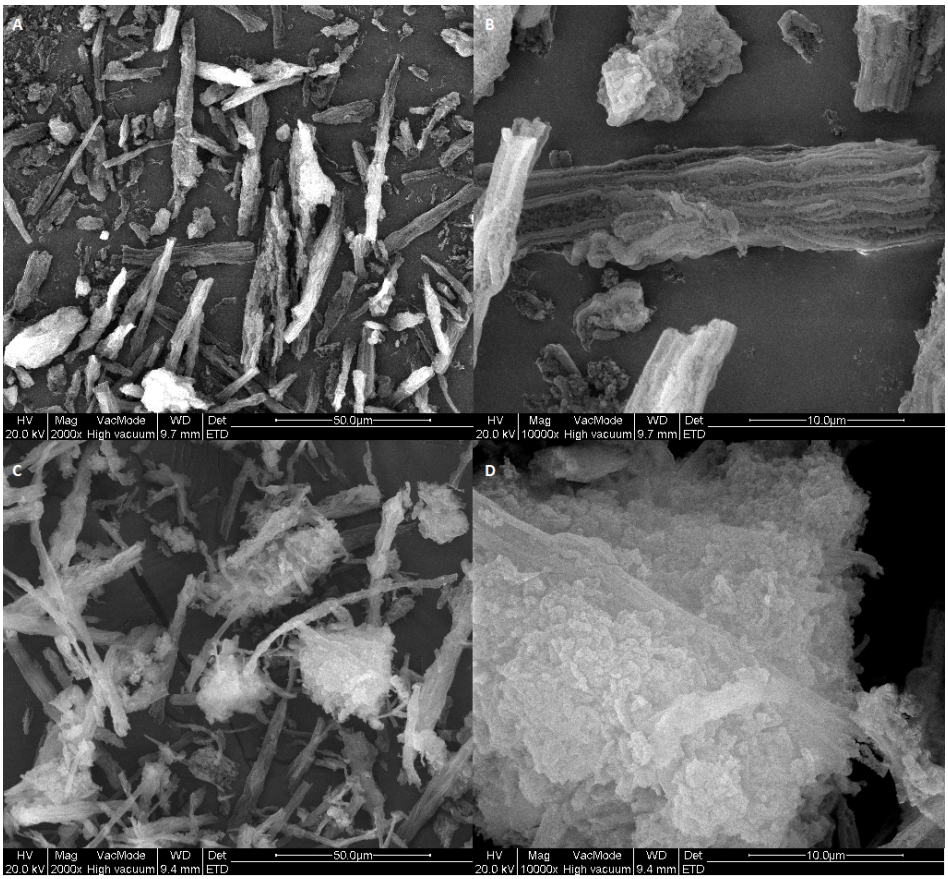


**Figure 3.11:** SEM images of Pic@PMO 3 (A and B) and Porph@PMO 2 (C and D)

loadings have been calculated using CHNS analysis. It could be concluded that successful binding of both ligands was achieved, with no adsorbed ligands present in the material (if a Soxhlet washing step was applied after click reaction). Still, as shown for Pic@PMO 3, some efficiency problems during the click reaction were observed. Increased stirring or reaction time might be possible solutions for this. However, for Porph@PMO this reaction did not cause any problems, most likely because PorphCys is more easily dissolving in water than PicCys.

Using TGA, the stability of both materials has been analyzed. It could be seen that the ligands detoriate between $\sim$ 200 and $\sim$ 500 ℃, leaving only the pure support. SEM imaging showed rodlike particles in the µm range. Disordered parts resulted in spherical particles.

# Chapter 4

# Catalysis: from $CO_2$ to cyclic carbonates

## 4.1 Green material synthesis: $CO_2$ as a building block

It is expected that in the near future, the worldwide need for new materials will keep on growing [82], as standards of living and world population will increase. While now most material and energy production is derived from fossil sources, this will cause problems with feed stock shortages in the future. Moreover, these processes are not sustainable and contribute to climate change. As one of the major scientific challenges of this era, this problem receives enormous amounts of attention and many different tactics are used to tackle this problem in various stages (e.g. optimizing processes, recycling, $CO_2$ capture). If one focuses on the capture of $CO_2$, two major possibilities exists: CCS (Carbon Capture and Storage, see [83] for more information on current progress) and CCU (Carbon Capture and Usage). As $CO_2$ is the most abundant renewable carbon source in the world [75], usage would be both environmentally as economically very attractive.

However, CCU still faces some major problems. First of all, $CO_2$ capture is a very difficult process, heavily depending on the used carbon source. A high purity is desired for easy separation, so preferably capture would be performed directly from the exhausts of industrial plants. In contrast to this, capture from air has many advantages too: installations could be placed anywhere and yield negative $CO_2$ emissions [84]. Secondly, $CO_2$ is a very stable chemical, so conversion processes need significant energy amounts and extremely active catalysts. Recent progress has been extensively discussed in a review of Kondratenko *et al.* [85].

Over the last thirty to forty years, many different reactions involving $CO_2$ have been developed

(see some examples in **Figure 4.1**), but still only very few reactions are used on industrial scale [86]. One of the most interesting and green reactions could be the catalytic synthesis of cyclic carbonates from $CO_2$ and epoxides, as can be seen in the lower left corner of the 'carbonates and carbamates' box of **Figure 4.1**.

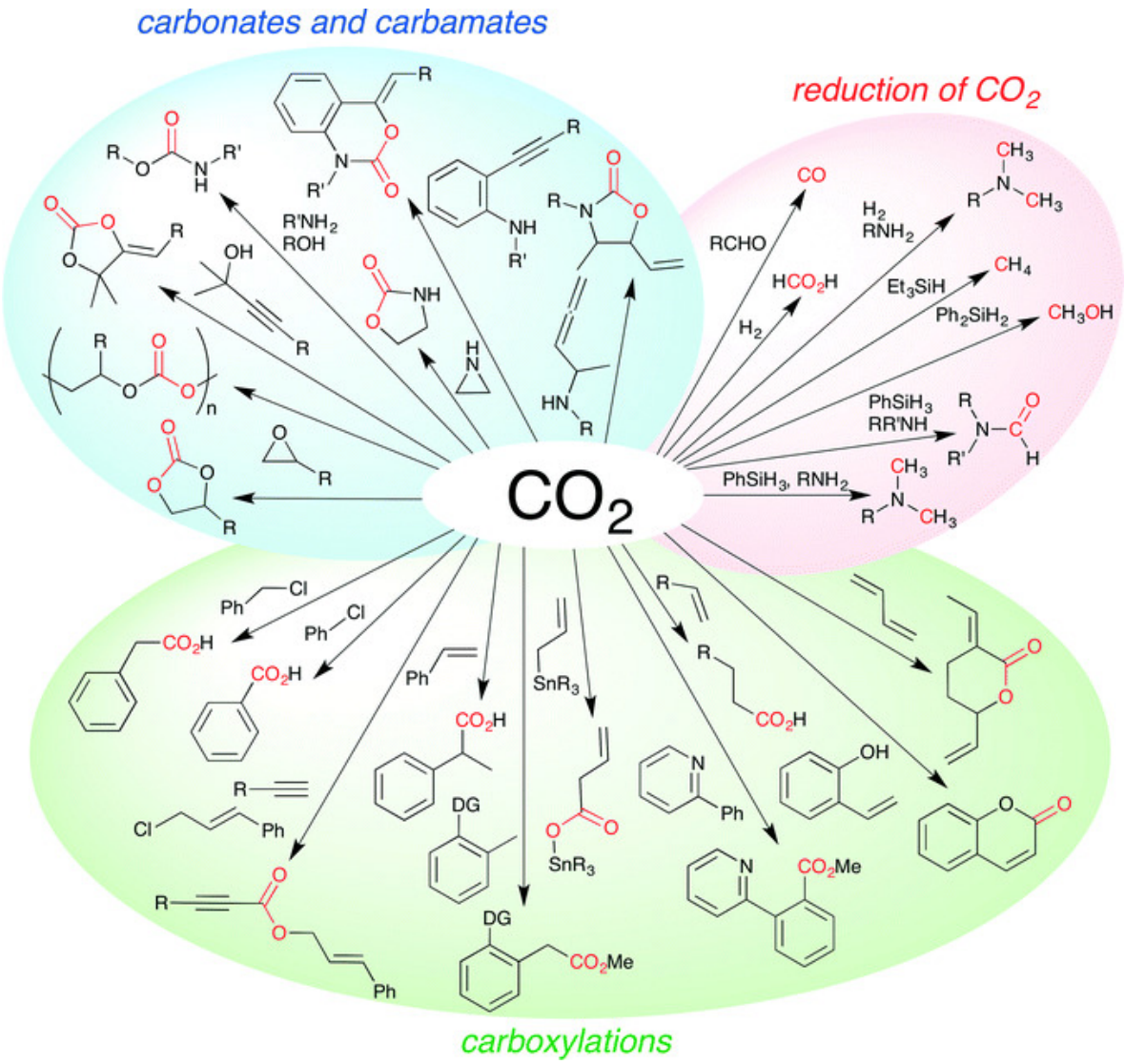


**Figure 4.1:** An overview of some products that can be obtained using $CO_2$ as building block [75]

## 4.2 Synthesis of cyclic carbonates from $CO_2$ and epoxides

Cyclic carbonates are widely used in multiple applications (*e.g.* synthesis of polycarbonates, aprotic polar solvents, fuel additives and electrolytes in batteries). Until now, these materials

are mostly synthesized via the phosgene method, using a toxic warfare gas and generating huge amounts of waste [75]. The catalyzed synthesis from epoxides and $CO_2$ would be a very attractive option to replace this non environmentally friendly process. This reaction not only uses the greenhouse gas $CO_2$ as a building block, but is also 100 % atom efficient[1] and can be performed without adding solvents. Much of the research done on this reaction has been reviewed by Martin *et al.* [87].

To overcome the often drastic reaction conditions required a wide variety of catalysts has been reported. These catalysts can be roughly divided into two groups:

- Metal complex based catalysts: by far the most studied metal complexes for this reaction are Salen [88–90] and porphyrin [91–94] complexes. The Lewis acidic metal center of these complexes, can activate epoxides by metal-oxygen coordination. To achieve reasonable conditions very often a co-catalyst, performing nucleophilic ring-opening of the epoxide, is required [75].
- Metal-free catalysts: these catalysts are very cost-efficient, readily available and show low toxicity. However they often require high temperatures, high pressures and long reaction times. They can show catalytic activity due to nucleophilic properties or coordination with the epoxide oxygen. An extended review about this type of catalysts has been made by Cokoja *et al.* [95].

Metal complex catalysts are thus often more active, but more expensive and toxic. By consequence, heterogenisation of these complexes would be very beneficial, but still only few reports on this exist [96], [97]. If these catalysts can be successfully anchored on a stable support, their price and toxicity would be far less problematic, while their high activity can still be used. The previously discussed monoallyl ring PMO is such a stable support, which has already successfully been used for catalysis [45]. By consequence our newly developed method to anchor ligands on PMOs can be readily used to yield and test the catalytic properties for this reaction of an heterogenized active metal complex.

## 4.3 Synthesis and characterization

$Co^{2+}$ was coordinated to the developed modified PMO materials (see **Chapter 3**) using reflux in DMF. Unreacted $Co(OAc)_2.4\,H_2O$ was removed using soxhlet extraction. Successful Co coordination was confirmed using XRF and influence on the structure was checked by $N_2$-sorption and PXRD measurements.

[1] Atom efficiency: the overall conversion efficiency of all atoms involved in the reaction. In a 100% atom efficient process are all atoms put in as reactants yielded in the product

### 4.3.1 Co@Pic@PMO

Using Pic@PMO 2, a material with ligand loading of 0.27 mmol/g, Co@Pic@PMO was prepared. A $Co^{2+}$ loading of 0.09 was calculated from XRF results, together with an S loading (which should be equal to the ligand loading) of 0.026 mmol/g. As there are big differences between CHNS and XRF results, it was concluded not to use these data quantitative, but only as a confirmation that $Co^{2+}$ coordination was indeed successful.

Structural results for the unmodified PMO (monoallyl PMO), the ligand coupled material (Pic@PMO 2) and the $Co^{2+}$ coordinated catalyst (Co@Pic@PMO) are presented in **Figure 4.2** and **Table 4.1**. Remarkably, it was observed that, while surface area, pore volume and wall thickness during coupling of the ligand decreased, these values increased again when coordinating $Co^{2+}$ to the material. Moreover, the surface area and wall thickness reached even higher values than measured for the unmodified material. These results should still be checked for reproducibility when making a second batch (especially the Pic@PMO 2 PXRD pattern), but suggest pore widening by coordination of $Co^{2+}$.

**Table 4.1:** Structural data of Co@Pic@PMO, Pic@PMO 2 and Monoallyl PMO 5

| | Co@Pic@PMO | Pic@PMO 2 | Monoallyl PMO |
|---|---|---|---|
| $S_{BET}(m^2/g)^a$ | 749 | 643 | 672 |
| $V_p(cm^3/g)^b$ | 0.86 | 0.84 | 0.89 |
| $d_{p,BJH}(nm)^c$ | 5.0 | 5.2 | 5.2 |
| e $(nm)^d$ | 7.7 | 5.7 | 6.9 |

[a]Specific surface area determined via Brunauer-Emmett-Teller theory [58].,[b]Pore Volume determined from adsorption branch at $P/P_0 = 0.99$, [c]Pore size calculated from desorption branch following Barrett-Joyner-Halenda theory [59]., [d] the wall thickness was calculated combining pore volume and XRD results

### 4.3.2 Co@Porph@PMO

Co@Porph@PMO was prepared using Porph@PMO 2, a material showing 0.37 mmol ligands/g in CHNS analysis. XRF analysis of Co@Porph@PMO showed 0.26 mmol $Co^{2+}$ per gram in addition to an S loading (which is equal to ligand loading) of 0.16 mmol/g. Again these data were not used quantitative but only as a confirmation of successful $Co^{2+}$ coordination.

**Figure 4.3** and **Table 4.2** show structural analysis data of PMO Upscaled (the unmodified

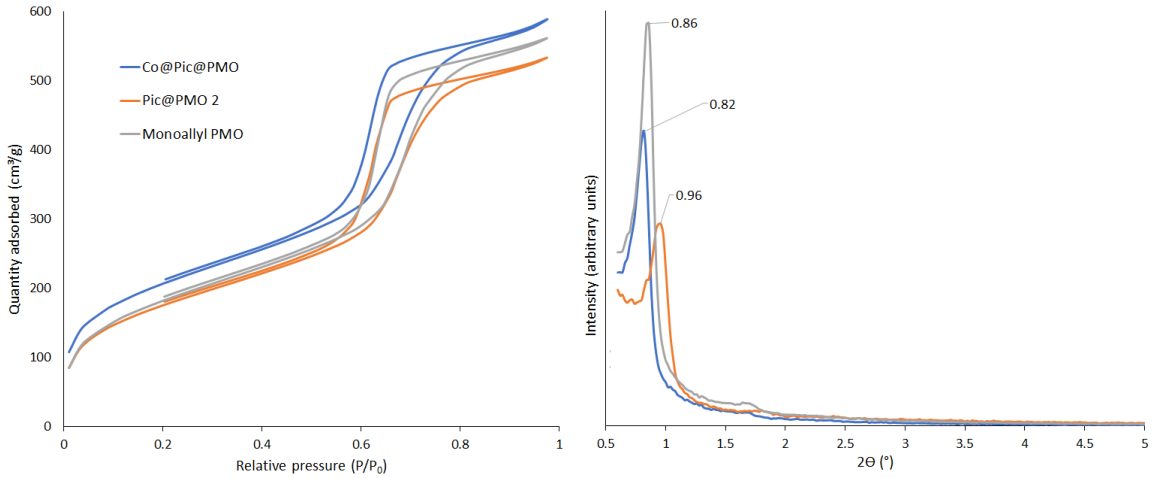


**Figure 4.2:** Structural analysis of Co@Pic@PMO, Pic@PMO 3 and Monoallyl PMO 5

PMO), Porph@PMO 2 (the ligand coupled material) and Co@Porph@PMO (the $Co^{2+}$ coordinated catalyst). As can readily be seen from the isotherm, coupling of the ligand results in a reduction in pore volume, while coordination of $Co^{2+}$ has no significant influence on the pore volume for this material. Still, the surface area increased during coordination of $Co^{2+}$, leading to a value almost as high as before anchoring of the ligands. Except a minor reduction in wall thickness during ligand anchoring, no significant changes were observed for pore width and wall thickness in this material. Like the results for Co@Pic@PMO, these should be checked to make sure the observed structural influence is reproducible, but a possible explanation for the increased surface area could be $Co^{2+}$ sticking out of the porphyrin ligand plane leading to higher ligand surfaces.

**Table 4.2:** Structural data of Co@Porph@PMO, Porph@PMO 2 and PMO Upscaled

| | Co@Porph@PMO | Porph@PMO 2 | PMO Upscaled |
|---|---|---|---|
| $S_{BET}(m^2/g)^a$ | 531 | 483 | 548 |
| $V_p(cm^3/g)^b$ | 0.47 | 0.50 | 0.61 |
| $d_{p,BJH}(nm)^b$ | 5.2 | 5.1 | 5.0 |
| $t^c$ | 7.2 | 7.3 | 7.7 |

[a]Specific surface area determined via Brunauer-Emmett-Teller theory [58]., [b]Pore size and volume calculated from desorption branch following Barrett-Joyner-Halenda theory [59]., [c] the wall thickness was calculated combining pore volume and XRD results

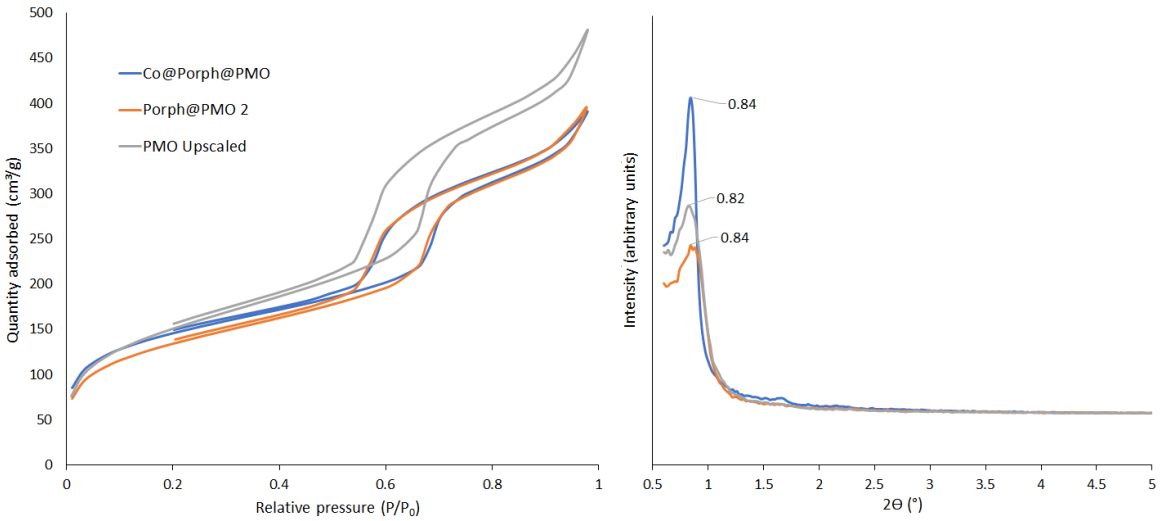


**Figure 4.3:** Structural analysis of Co@Porph@PMO, Porph@PMO 2 and PMO Upscaled

### 4.3.3 TEM images

Using Transmission Electron Microscopy (TEM) imaging, some images of both materials have been made. In **Figure 4.4 A and B**, a mixture of a nicely structured patches and disordered parts is observed. However, in **Figure 4.4 C and D**, only perfectly ordered porous materials are found. This difference is in agreement with the results from **Chapter 2**, where it was observed that PMO Upscaled (the base material for Co@Porph@PMO) showed some disordered areas, while Monoallyl PMO (the base material for Co@Pic@PMO) was proven to be perfectly ordered.

Moreover, in **Figure 4.4 C and D**, one can see the difference in planes. On the left, pores are perpendicular to the plane and thus observed as hexagons (in theory it is possible to look right trough the material using these pores), while the bigger part shows pores parallel to the plane, observed as long rods. Using the size of the white hexagons in **Figure 4.4 D**, the pore width could be estimated at 5.0 nm, perfectly matching with the obtained result using $N_2$-sorption. The distance between the center of two pores ($a_0$) could be estimated as 11 nm, close to the calculated 12 nm via PXRD and $N_2$-sorption.

Furthermore, as in both materials only the PMO structure was observed, it is very likely that indeed the ligands and $Co^{2+}$ are situated in the porous structure and not as separate nanocrystals. Still, to effectively prove this, STEM-EDX (Scanning Transmission Electron Microscopy Energy Dispersive X-ray spectroscopy) analysis is required.

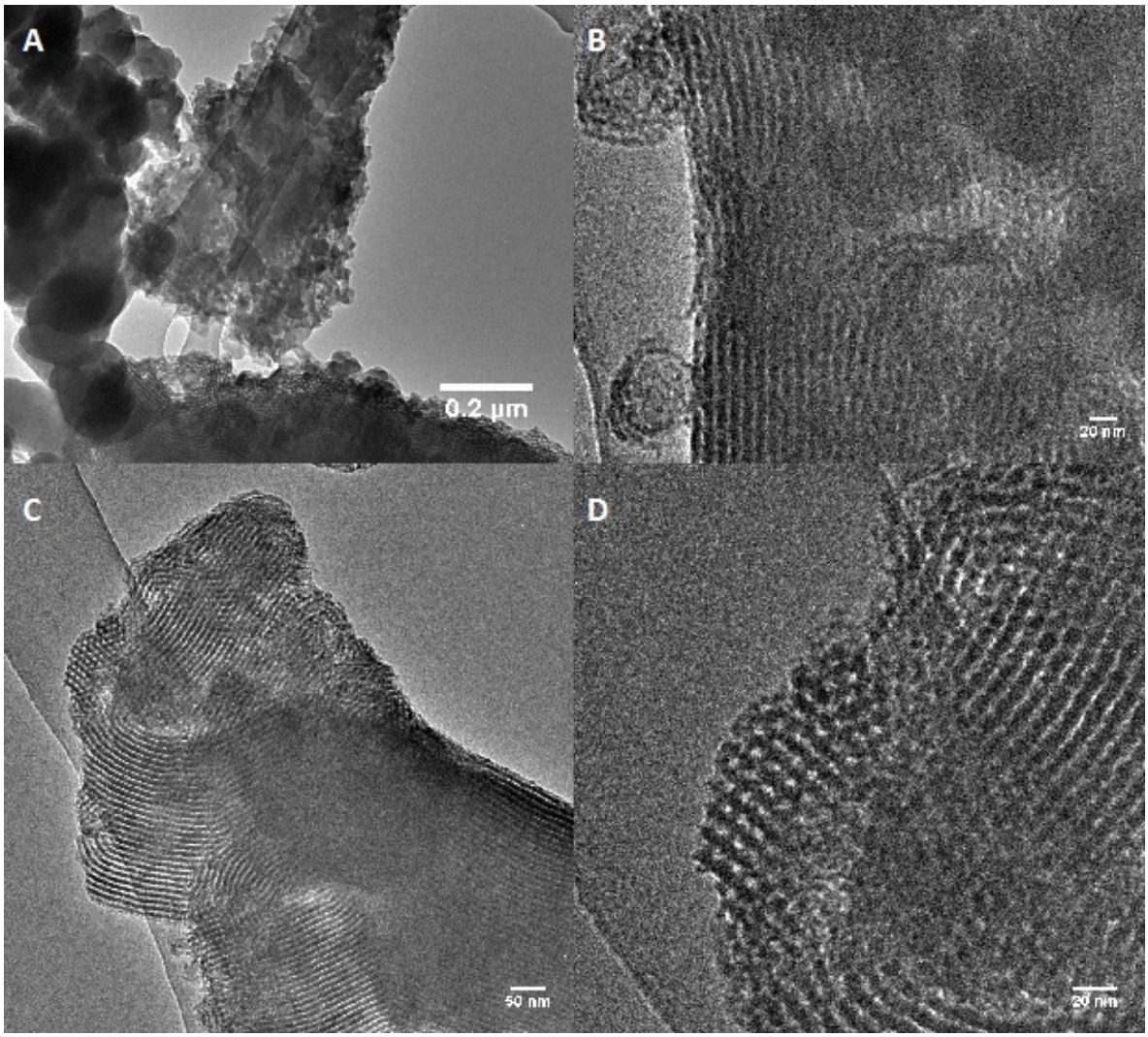


**Figure 4.4:** A and B TEM images of Co@Porph@PMO; C and D TEM images of Co@Pic@PMO

## 4.4 Catalytic tests: Results and Discussion

For catalytic testing, conditions have been based on the procedure used by Paddock *et al.* [93] for homogeneous $Co^{3+}$ porphyrin catalysts. Based on this system, parameters were altered and optimized for the synthesized Co@Porph@PMO and Co@Pic@PMO materials. To enable reaction in high temperature and pressure regimes, epichlorohydrin has been chosen as the starting material (the $^1$H NMR spectrum of epichlorohydrin can be found in **Appendix C**, a scheme of the catalytic reaction is presented in **Figure 4.5**). As a co-catalyst 4-Dimethylaminopyridine (DMAP was added. Furthermore, we increased reaction time from one to two hours.

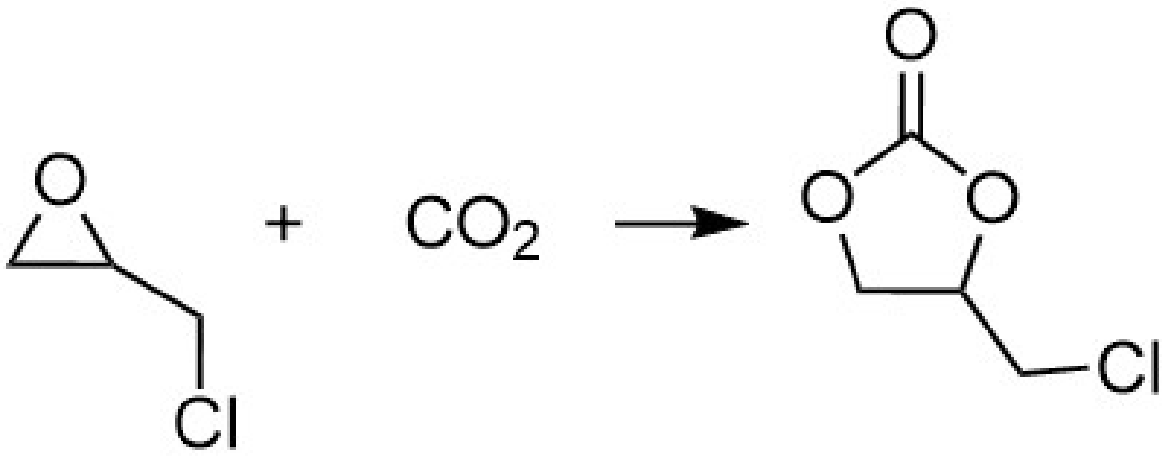


**Figure 4.5:** A scheme of the catalysed coupling of epichlorohydrine and $CO_2$

### 4.4.1 Catalytic performance

A first catalytic test (Parameters: Co@Porph@PMO, 1 hour, 6 bar $CO_2$, 120 ℃) was analyzed using GC/MS, the only peaks observed assigned belonged to the product and internal standard (mesitylene) (the obtained spectrum is presented in **Appendix C**). Thus it could be concluded that no side products were formed and reaction efficiency could be estimated using simple conversion of starting material to product. This has been done using $^1$H NMR (all spectra are presented in **Appendix C**).

In a first trial, the two different materials were compared to the homogeneous $Co^{2+}$ porphyrine (Co@Porph) catalyst, catalytic results for this trial are shown in **Table 4.3**. As, ligand loadings could not be accurately determined, 10 mg of catalyst was used in each system (which corresponds with $1.2 * 10^{-2}$ mmol for Co@Porph). From entry 1 (the homogeneous catalyst), it could be concluded that the $Co^{2+}$ porphyrin system is an efficient catalyst, as the conversion reached 100 %. When continuing with the two heterogeneous systems, a slight decrease in conversion is noted, as would be expected. Still, a conversion of over 90% for the porphyrin material (entry 2) is observed. Moreover, the picolinic acid system, which to the best of our knowledge hasn't been tested for this reaction yet, also shows a high conversion of almost 80%. The observed decrease in conversion for the heterogeneous could be explained by the increased diffusion needs to get both reactants in the pore at the catalytic active sites. For homogeneous catalysts, in solution with the starting material, this is much less limited and reaction happens faster.

**Table 4.3:** Catalytic activity of Co@Pic@PMO, Co@Porph@PMO and Co@Porph

| Entry | Catalytic system | Conversion (%) |
|---|---|---|
| 1 | Co@Porph | 100 |
| 2 | Co@Porph@PMO | 91.6 |
| 3 | Co@Pic@PMO | 79.9 |

Reaction conditions: catalyst (10 mg), co-catalyst (DMAP, 1mg, $8 * 10^{-3}$ mmol), epichlorohydrin (0.5 mmol), $CO_2$ (6 bar), $CH_2Cl_2$ (2 mL), time = 2 hours, 120 ℃.

As numerous publications about this reaction report a significant influence of $CO_2$ pressure on this reaction [93, 94, 98], this has been studied for both materials. Co@Porph@PMO has been tested at 6, 4 and 2 bars, while the slightly less active Co@Pic@PMO has been tested at 6, 5 and 4 bars.

The obtained conversions for Co@Pic@PMO are presented in **Table 4.4**. As resulted conversions are all found to be in the 70-80% interval it is readily noticed that no significant influence of pressure was obtained. Still, no significant conclusions could be drawn from this result, as it was very hard to find the starting material peak in the $^1$H NMR spectra. Most likely, this is due to the very small quantities used for this reaction, resulting in significant post-reaction treatment and big influences of small deviations. For example, the starting material could still be stuck in the pores of the catalyst, not only resulting in incorrect calculated conversions but also partial deactivation [2].

**Table 4.4:** Catalytic activity of Co@Pic@PMO at different pressures

| Entry | $CO_2$ Pressure (bar) | Conversion (%) |
|---|---|---|
| 1 | 6 | 79.9 |
| 2 | 5 | 71.3 |
| 3 | 4 | 76.2 |

Reaction conditions: catalyst (10 mg), co-catalyst (DMAP, 1mg, $8 * 10^{-3}$ mmol), epichlorohydrin (0.5 mmol), $CH_2Cl_2$ (2 mL), time = 2 hours, 120 ℃.

Finally, a comparable pressure study has been performed for the Co@Porph@PMO catalytic

[2] It has to be noted that this process could also have influenced the observed conversions in **Table 4.3**. While those results seem to be logical, deviations could still happen.

system, the obtained results are shown in **Table 4.5**. While dropping reaction pressure from 6 to 4 bar only had a small influence on the calculated conversion, a dramatic drop was observed when lowering reaction pressure to 2 bar. Moreover, intense starting material peaks have been observed in the $^1$H NMR of the 2 bar catalytic test, indicating reduced conversion and thus too much remaining starting product to remain in the pores. This result is quite expected, as the starting 6 bar is already only a fraction of the 250-300 psig ($\sim$ 17-21 bar) used by Paddock *et al.* [93], who concluded a clear relationship between pressure and catalytic activity.

**Table 4.5:** Catalytic activity of Co@Porph@PMO at different pressures

| Entry | $CO_2$ Pressure (bar) | Conversion (%) |
|---|---|---|
| 1 | 6 | 91.6 |
| 2 | 4 | 78.2 |
| 3 | 2 | 18.1 |

Reaction conditions: catalyst (10 mg), co-catalyst (DMAP, 1mg, $8 * 10^{-3}$ mmol), epichlorohydrin (0.5 mmol), $CH_2Cl_2$ (2 mL), time = 2 hours, 120 ℃.

The proposed mechanism of the reaction [93, 98], is presented in **Figure 4.6**. It can be observed from the mechanism that the role of the synthesized catalyst is to activate the epoxide by binding of the metal with the epoxide oxygen. Subsequently, the nucleophilic DMAP opens the ring and $CO_2$ is inserted. A five-membered ring is ultimately formed. As can be seen from the reaction mechanism, an acidic metal center is preferred as it will bind more easily with the epoxide [93]. By consequence, it is very likely that the oxidized catalyst (with coordinated $Co^{3+}$ instead of $Co^{2+}$) would perform even better in this reactions.

### 4.4.2 Reusability of the catalyst

The filtrate of each catalytic test was checked on leaching using the observed Co peak in XRF. A small Co peak was detected in some samples (Co@Porph@PMO 4 bar, Co@Porph@PMO 2 bar, Co@Pic@PMO 4 bar), but as the value of the peak was extremly low ( maximum: 0.13 CPS, for comparison, Co@Porph@PMO 3 yielded 233000 CPS and Co@Pic@PMO 85000 CPS for Co) this was assigned to noise. However, the homogeneous catalyst only yielded a comparable Co signal to these three samples, most likely indicating bad porphyrin solubility in chloroform.

Furthermore, a second (shorter) run has been performed for Co@Porph@PMO, catalytic

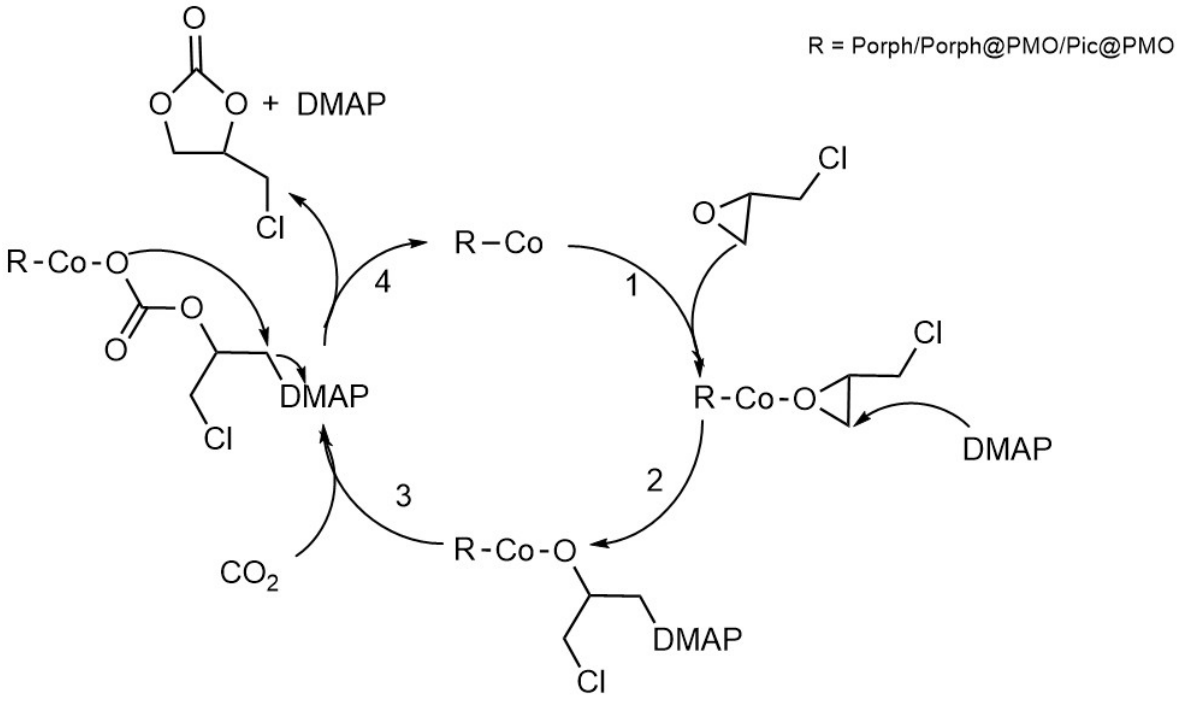


**Figure 4.6:** Proposed mechanism of the catalysed coupling of $CO_2$ and epichlorohydrin

results for this run have been given in **Table 4.6**. A conversion of 70.3 % was obtained during only 1 hour reaction time, a result that most likely for 2 hours would be very comparable to the obtained 91.6% of the first run. Moreover, in the $^1$H NMR spectrum of this sample, the starting material peaks are very prominently visible, which is in agreement with our theory of starting material getting stuck in the pores during reaction. As no clear reduction in catalytic activity is observed, it is most likely that this adsorbed starting material is not stuck on the active sites and poisoning the catalyst, but just coming out during simple washing steps.

**Table 4.6:** Reusability Co@Porph@PMO

| Entry | Catalyst | Reaction time (h) | Conversion (%) |
|---|---|---|---|
| 1 | Co@Porph@PMO run 1 | 2 | 91.6 |
| 2 | Co@Porph@PMO run 2 | 1 | 70.3 |

Reaction conditions: catalyst (10 mg), co-catalyst (DMAP, 1mg, $8 * 10^{-3}$ mmol), epichlorohydrin (0.5 mmol), $CO_2$ (6 bar), $CH_2Cl_2$ (2 mL), 120 ℃.

## 4.5 Conclusions

Both materials showed good catalytic activity with high conversions. Still, to accurately determine the potential of these materials for this reaction, the reaction needs to be performed on larger scale or a more accurate activity calculations need to be found. As no leaching was observed and a second run for Co@Porph@PMO still showed high activity, the catalysts are most likely reusable and thus successful heterogenized. Studying the reaction mechanism, it was noted that oxidation to $Co^{3+}$ should yield even better activities.
A clear pressure-activity relation was found for Co@Porph@PMO, with a steep drop at low pressures. For Co@Pic@PMO, an unclear relationship was established.

To conclude this research, more catalytic tests at other pressures need to be done, besides multiple recylcing runs of both catalysts. Furthermore, larger scale reactions, to more correctly determine activity and blank reactions (unmodified PMO, Porph@PMO and Pic@PMO without coordinated Co, no co-catalyst) are also required to unravel the catalytic activity of those materials. By doing this reactions in larger scales, the possibility to compare XPS and $N_2$-sorption spectra of the catalyst before and after reaction runs arises. This way, differences in oxidation state and pore volume could be studied to discover the true reusability of these catalysts.

# Chapter 5

# Luminescence: Visual and NIR emittance

## 5.1 Luminescent properties of lanthanide complexes

Lanthanides are the first group of elements with occupied 4f orbitals, which gives some very interesting properties. Due to the inner nature of these 4f orbitals, they are shielded by the filled 5s and 5p orbitals. This yields characteristic narrow emission peaks, sizeable quantum yields and relatively long luminescence decay times [99], [100] for their $Ln^{3+}$ ions, which find many different applications [101]. However, the f-f transitions of lanthanides are partly forbidden and thus show a very low absorption probability, which results in low emission intensities. This problem is solved by complexing $Ln^{3+}$ ions with various organic ligands (e.g. $\beta$-deketonates), which are used as an energy harvesting moiety [99]. These ligands efficiently absorb light and transfer the energy to the lanthanide ion. A scheme of this process, called the antenna effect is provided in **Figure 5.1**.

To ensure efficient luminescence, these complexes have to follow some restricting conditions. First of all the T1-Ln* energy difference should be between 2500 and 3500 $cm^{-1}$ to ensure efficient energy transfer. Secondly, quenching groups like OH and NH in the immediate environment of the $Ln^{3+}$ ion should be avoided. To ensure this, the first coordination sphere should be tight and rigid [99]. Many complexes following these restrictions have been developed. Furthermore, the complex should have good thermodynamic and kinetic stability. Nevertheless, the used organic ligands fail to withstand mechanical treatment, high temperatures, pressures and moisture [101], [102].

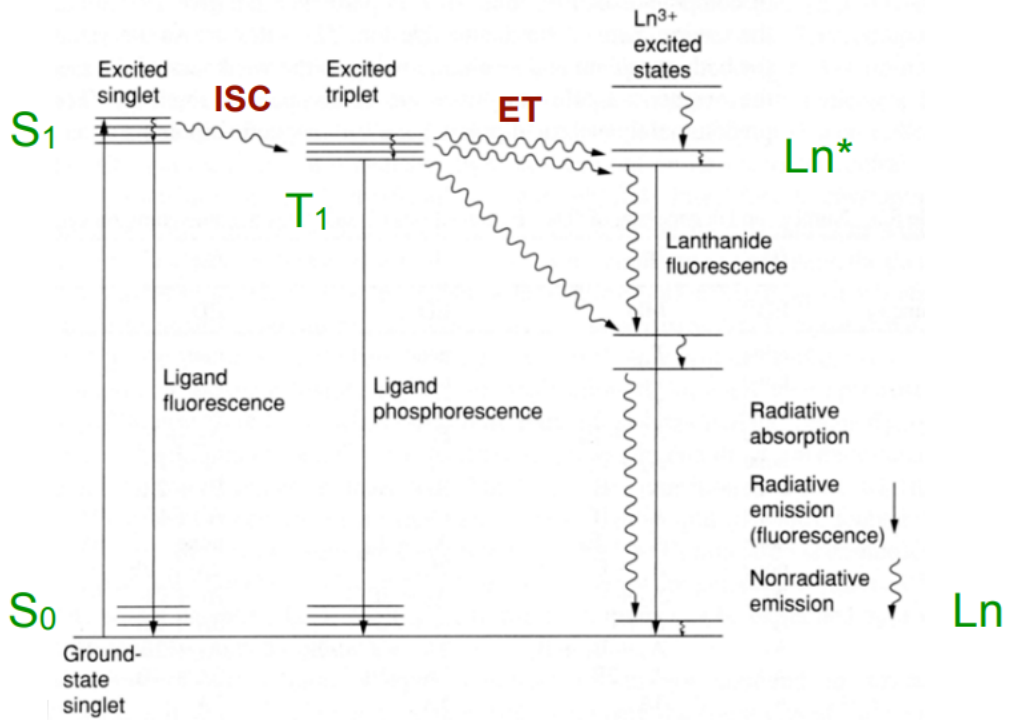


**Figure 5.1:** A schematic representation of possible energy transfer processes in a $Ln^{3+}$-organic ligand complex (antenna effect) [99]

## 5.2 Anchoring of lanthanides onto PMO

In order to overcome this stability problem, inorganic and organic-inorganic hybrid ligands have been developed. This way stable organic-inorganic hybrids were prepared, a new class of photo-functional lanthanide materials [102], [103]. These materials integrate properties of organic compounds (high processability, organic functionalities and elasticity) with the hardness and thermal and chemical stability of inorganic compounds. As chemically bound hybrids are preferred to prevent leaching, PMOs are very attractive candidates for this. Organic functional groups can easily be incorporated and the well-ordered mesoporous structure and large surface areas make them excellent supports for this kind of complexes [104], [105].

## 5.3 Coordination of the lanthanides

The synthesized materials were used to coordinate different lanthanide cations. As Pic@PMO's excited state energy level is wel matching for lanthanides emitting in the visible area it has been grafted with $Tb^{3+}$ and $Eu^{3+}$, while Porph@PMO, which excited state level is perfect

vor NIR emitting lanthanides, has been grafted with $Yb^{3+}$.

## 5.4 Luminescence properties: Results and Discussion

### 5.4.1 Pic@PMO luminescence

A combined emission-excitation spectrum of pure Pic@PMO has been recorded (**Figure 5.2**). It can be seen that the material is easily excited around 350-400 nm, which yields a broad emission peak from 400-600 nm. The sharp peaks observed between 420 and 480 nm originate from the Xenon excitation source and are thus not a feature of the material.

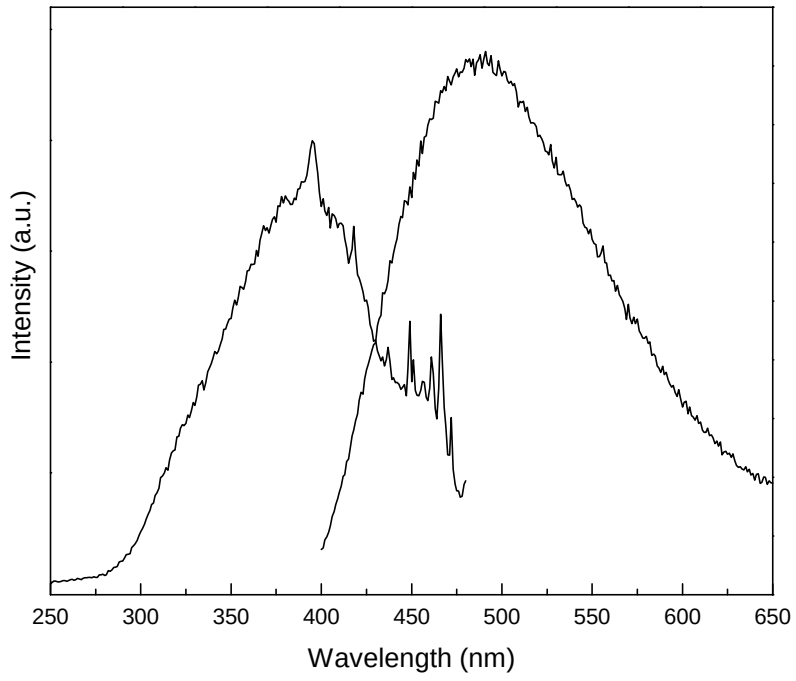


**Figure 5.2:** Combined emission-excitation spectrum of pure Pic@PMO

The Pic@PMO materials have been (co-)grafted with $Eu^{3+}$ and $Tb^{3+}$ cations in different molar ratios. By varying the relative amounts of lanthanide cations, the emittance color of the material could be tuned. In **Figure 5.3** the excitation-emission spectra of Pic@PMO coordinated with $Eu^{3+}$ (Eu@Pic@PMO) and $Tb^{3+}$ (Tb@Pic@PMO) ions have been presented.

When comparing the excitation spectra, it can be noted that both materials show an intense

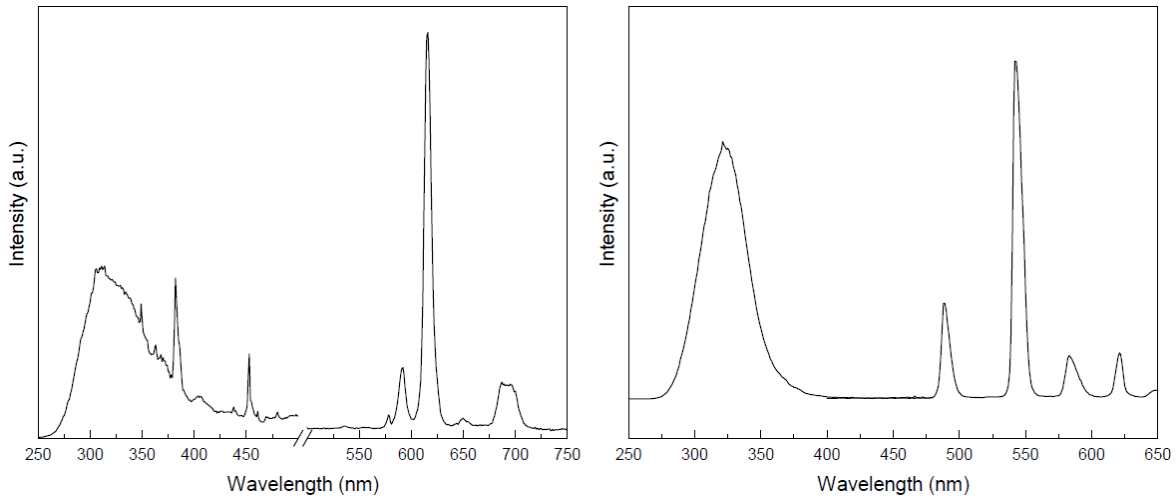


**Figure 5.3:** Combined emission-excitation spectrum of Eu@Pic@PMO (left) and Tb@Pic@PMO (right)

broad peak around 350 nm, originating from the Pic@PMO support material. By coordination of a lanthanide ion, this peak has been shifted to lower wavelengths (almost 400 nm for the non-grafted material, around 330 nm for Tb@Pic@PMO and just above 300 nm for Eu@Pic@PMO). In the Eu@Pic@PMO excitation spectrum, this broad peak is accompanied by some sharp f-f transition peaks resulting from the $Eu^{3+}$ cation. The peak around 380 nm is assigned to the ${}^5L_6 \longleftarrow {}^7F_0$ transition and around 455 nm to the ${}^5D_2 \longleftarrow {}^7F_0$ transition. The Tb@Pic@PMO sample only shows the broad ligand excitation peak, which means that energy absorption and transfer from the antenna is more efficient in this sample.

Further analyzing the emission spectra, it could be observed that both materials only show sharp f-f transition peaks (the assigned peaks are listed in **Table 5.1**, which points to efficient energy transfer from the host material to the $Ln^{3+}$ ions. As the ${}^5D_0 \longrightarrow {}^7F_2$ peak is by far the most intense for Eu@Pic@PMO one can conclude that the environment exhibits low symmetry, thus no inversion points will be present [99].

Ideal for efficient energy transfer between the antenna $T_1$ and lanthanide emitting state is an energy difference of $\sim$ 3000 $cm^{-1}$ [99]. In literature, $T_1$ level of silica bounded picolinic acid, a comparable material, was reported to be 25252 $cm^{-1}$ [106], corresponding with a 396 nm absorption peak (which is almost perfectly matching with the absorption peak of Pic@PMO in **Figure 5.3**). The energy gap to the $Tb^{3+}$ emitting level (${}^5D_4$, 20500 $cm^{-1}$), is thus already quite large, yielding non-ideal energy transfer. Still, when analyzing Tb@Pic@PMO's excitation-emission spectrum, a broad Pic@PMO absorption peak is noted in combination with sharp $Tb^{3+}$ emission peaks, indicating efficient energy transfer.

However, for the Eu@Pic@PMO material, some f-f transitions in the absorption spectra are noted, indicating less efficient energy transfer and by consequence lower efficiency. As $Eu^{3+}$'s emitting level has even lower energy than $Tb^{3+}$'s ($^5D_0$, 17277 $cm^{-1}$), this is an expected result.

**Table 5.1:** Assignment of the Eu@Pic@PMO and Tb@Pic@PMO emission peaks

| Wavelength (nm) | Wavenumber ($cm^{-1}$) | f-f transition |
|---|---|---|
| Eu@Pic@PMO [107], [108], [99] | | |
| 575 | 17390 | $^5D_0 \longrightarrow {}^7F_0$ |
| 590 | 16950 | $^5D_0 \longrightarrow {}^7F_1$ |
| 620 | 16130 | $^5D_0 \longrightarrow {}^7F_2$ |
| 650 | 15385 | $^5D_0 \longrightarrow {}^7F_3$ |
| 690 | 14490 | $^5D_0 \longrightarrow {}^7F_4$ |
| Tb@Pic@Pic@PMO [109], [108], [99] | | |
| 485 | 20620 | $^5D_4 \longrightarrow {}^7F_6$ |
| 550 | 18180 | $^5D_4 \longrightarrow {}^7F_5$ |
| 580 | 17240 | $^5D_4 \longrightarrow {}^7F_4$ |
| 625 | 16000 | $^5D_4 \longrightarrow {}^7F_3$ |

Combining these two different lanthanides ($Eu^{3+}$ and $Tb^{3+}$) in different ratios should yield emission close to white light. In **Figure 5.4**, the luminescence profile of a sample containing equal molar ratios of $Tb^{3+}$ and $Eu^{3+}$ (Tb,Eu(1:1)@Pic@PMO) is shown. Typical $Tb^{3+}$ emission peaks (matching with the ones assigned in **Table 5.1**) are observed in the green region, while peaks in the red region are in agreement with observed Eu@Pic@PMO peaks. When looking at the CIE (International Commission on Illumination, abbreviation for French name: Commission Internationale de l'Éclairage) profile, it is clear that almost pure yellow light is obtained (see **Figure 5.5** for the visually observed luminescence of the different samples).
To make white light a blue component should be added, which is not present in this sample. However, blue light components for this material could only originate from the ligand, as there are no lanthanides emitting in the blue range that can be excited by this host material [99]. Thus, as energy transfer in the material is very efficient and no ligand band is present, a blue light component and resulting white light can never be obtained using this material.
The data shown are valid for excitation at 322 nm (corresponding with the maximum of the materials excitation peak, the materials combined excitation-emission spectrum can be found in **appendix C**), excitation at other wavelengths yielded slightly different ratios of emission

peaks but none resulted in pure white light (the emission map combining 7 emission spectra recorded using excitation between 300 and 350 nm can be found in **appendix C**).

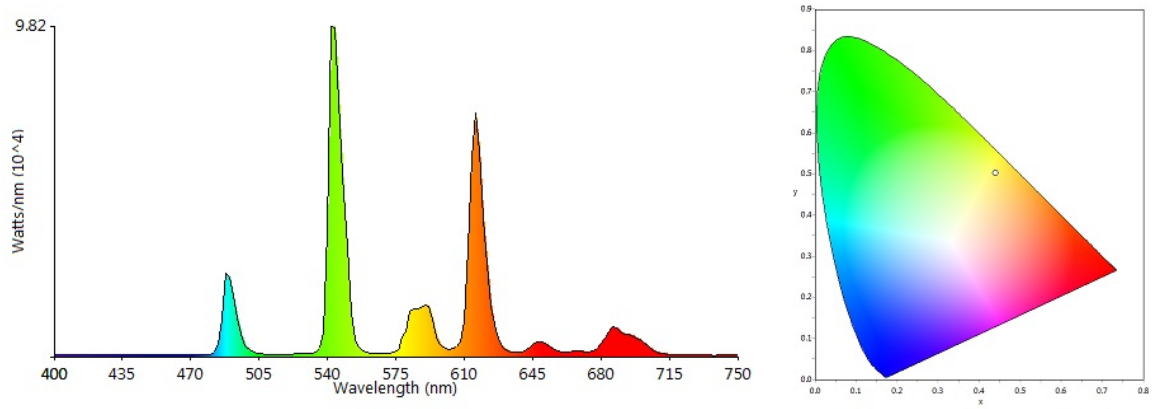


**Figure 5.4:** Luminescence profile of Tb,Eu(1:1)@Pic@PMO excited at 322 nm, left: emission spectrum with representation of matching colors at each wavelength, right: CIE chromaticity diagram of the sample

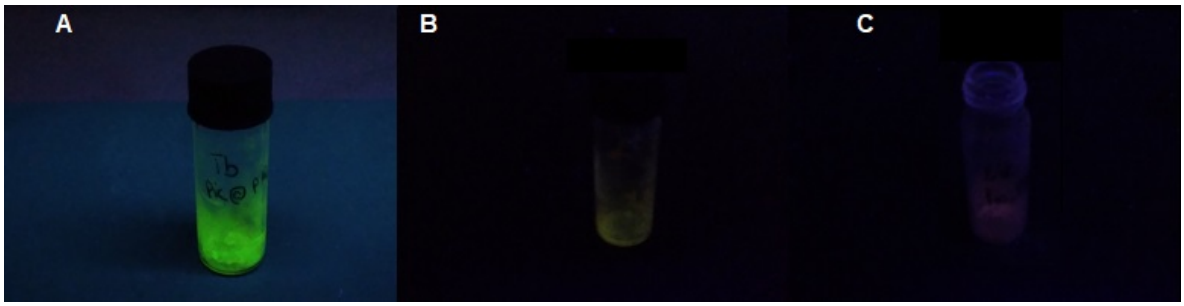


**Figure 5.5:** Observed luminescence of Pic@PMO samples, a 302 nm wavelength excitation was used to take these photos: A) Tb@Pic@PMO emitting bright green light, B) Tb,Eu(1:1)@Pic@PMO emitting yellow light, C) Eu@Pic@PMO emitting red light

The calculated CIE coordinates and CCT (Correlated Color Temperature) can be found in **Table 5.2**. As white light corresponds to x=0.333 and y=0.333 it can be concluded that the coordinate values are too high to yield white light (at all studied excitation wavelengths). All samples show a CCT between 2700 and 3600 K, which means that the emitted color corresponds with an emitting Planckian radiator[1] heated to this temperature [110]. The observed CCT values are situated a little below the value for white light, which corresponds with the observed warm yellow light.

[1] an ideal radiator

**Table 5.2:** Calculated CIE coordinates and CCT for Tb,Eu(1:1)@Pic@PMO excited at different wavelengths

| excitation wavelength | CIE x | CIE y | CCT (K) |
|---|---|---|---|
| 300 nm | 0.4505 | 0.4857 | 3355 |
| 310 nm | 0.4422 | 0.4986 | 3549 |
| 320 nm | 0.4411 | 0.5014 | 3581 |
| 322 nm | 0.4404 | 0.5025 | 3597 |
| 330 nm | 0.3951 | 0.5220 | n/a |
| 340 nm | 0.4559 | 0.4777 | 3228 |
| 350 nm | 0.4730 | 0.4355 | 2709 |

The decay profiles of Eu@Pic@PMO and Tb@Pic@PMO are presented in **Figure 5.6**, those of Pic@PMO and Tb,Eu(1:1)@Pic@PMO can be found in **appendix C**. Decay data of all materials has been listed in **Table 5.3**. Except for the Tb,Eu(1:1)@Pic@PMO 616 nm peak, the curves could only be well fitted when using a double-exponential function, which suggests that the $Ln^{3+}$ cations are surround by more than one coordination environment. This is quite common in hybrid support materials [104]. Decay times have been calculated using **Formula 5.1** for mono-exponential decay, **Formula 5.2** for bi-exponential decay and **Formula 5.3** to calculate the average decay times.

$$y = A_1 * e^{(-x/t_1)} + y_0 \tag{5.1}$$

$$y = A_1 * e^{(-x/t_1)} + A_2 * e^{(-x/t_2)} + y_0 \tag{5.2}$$

$$\tau_{av} = \frac{A_1 * \tau_1^2 + A_2 * \tau_2^2}{A_1 * \tau_1 + A_2 * \tau_2} \tag{5.3}$$

Where $t_1$ and $t_2$ are the mean lifetimes of both sets and $A_1$ and $A_2$ their respective amplitudes. $y_0$ corresponds with the intensity at t=0.

It is readily noted from the presented data that decay times for pure Pic@PMO are very short, in the range of 1 ns. The lanthanide coordinated materials show as expected decay times which are much longer, with big differences between the differently grafted materials. Tb@Pic@PMO shows the longest decay time and Eu@Pic@PMO the shortest (with the different peaks of Tb,Eu(1:1)@Pic@PMO in between). This is an extra confirmation of more efficient luminescence in the Tb@Pic@PMO sample, with very long decay times. For

Tb,Eu(1:1)@Pic@PMO, the $Eu^{3+}$ peak (616 nm) shows a longer decay time than the $Tb^{3+}$ peak (542 nm), with longer decay times for these peaks as for the pure $Eu^{3+}$ doped material. This suggests Tb-to-Eu transfer, previously observed in PMO supported lanthanide complexes by Biju *et al.* [105]. As this energy transfer occurs, the ligands should be quite close to each other, otherwise this would not be possible. Still, compared to the literature material, this process was proven less efficient as the Tb emission peak is still the most intense and Tb and Eu emission decay times are in the same range.

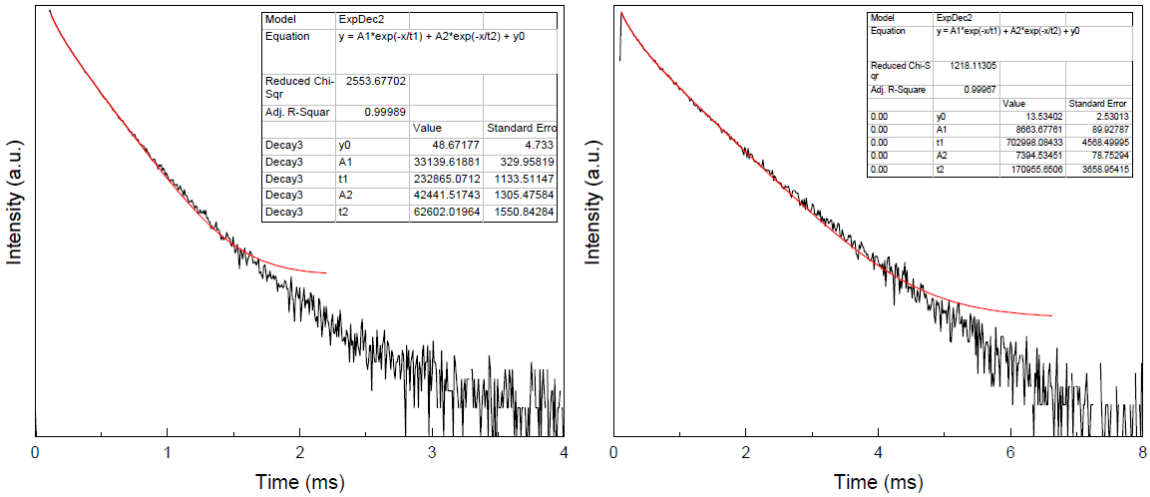


**Figure 5.6:** Decay profiles of Eu@Pic@PMO (left) and Tb@Pic@PMO (right)

**Table 5.3:** Luminescence decay times of Pic@PMO samples

| Sample | $\tau_1(\mu s)$ | $\tau_2(\mu s)$ | $\tau_{av}(\mu s)$ |
|---|---|---|---|
| Pic@PMO | $8.1 * 10^{-4}$ | $4.6 * 10^{-3}$ | $1.1 * 10^{-3}$ |
| Eu@Pic@PMO | 232.9 | 626.0 | 189.3 |
| Tb@Pic@PMO | 703.0 | 171.0 | 611.5 |
| Tb,Eu(1:1)@Pic@PMO 542 nm peak | 86.2 | 450.7 | 324.9 |
| Tb,Eu(1:1)@Pic@PMO 616 nm peak | 469.3 | n/a | n/a |

### 5.4.2 Porph@PMO Luminescence

Excitation and emission spectra of the pure Porph@PMO material have been measured and are presented in **Figure 5.7**. The excitation spectrum is dominated by the intense B (Soret[2]) band around 420 nm, with a shoulder around 390 nm. This peak is characteristic for the allowed $S_0 \longrightarrow S_2$ transition of porphyrins. In the emission spectrum, two peaks can be observed, one at around 650 nm and one around 720 nm, corresponding to respectively the $Q_{(0,0)}$ and $Q_{(0,1)}$ bands, characteristic for the forbidden porphyrin $S_0 \longrightarrow S_1$ transitions. When comparing these results with literature results [70] it is clear that pure porphyrin luminescence is observed and thus the porphyrin structure remained intact during the synthesis. However, the relative intensity of the $Q_{(0,0)}$ band in comparison with the $Q_{(0,1)}$ band is much lower than for unsubstituted porphyrins. This most likely results from the coupling of porphyrins to the PMO, as $Q_{(0,0)}$ intensity (and spectral position) is very sensitive for changes in the environment of the porphyrin

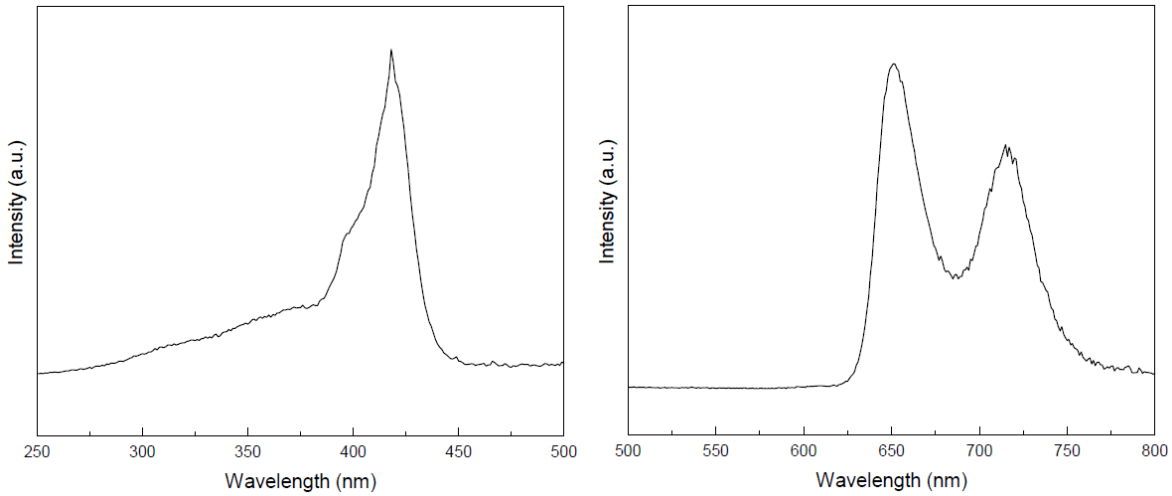


**Figure 5.7:** Excitation (left) and emission (right) spectra of pure Porph@PMO

As mentioned previously, porphyrins are perfect ligands for the coordination of lanthanides due to their strong light absorbing properties and easy binding with all kinds of Ln(III) cations. The most interesting lanthanides to couple with these ligands are the NIR emitting $Nd^{3+}$, $Er^{3+}$ and $Yb^{3+}$, as porphyrin excited state levels match perfectly with the accepting level of these $Ln^{3+}$ ions. As $Yb^{3+}$ usually gives the best quantum yields of the NIR emitting lanthanides [112], it has been studied in this work.

[2] An intense peak in the blue region, discovered by and named after Jacques-Louis Soret [111]

The Yb@Porph@PMO material could be excited at two different wavelengths (**Figure 5.8**), in the blue (around 460 nm) and red (around 650 nm and higher) region. The blue band was assigned to the porphyrin Soret band, which did not show any shoulder in this material. Most likely the shift to higher wavelengths and disappearance of the shoulder in comparison with non-grafted Porph@PMO results from metalation and substitution of the porphyrin and resulting symmetry changes. Moreover, a broad peak around 350 nm appears, which was not observed for the material without a coordinated lanthanide. Between 650 and 750 nm, at the far edge of the visual spectrum and very close to the NIR, four intense peaks are observed, most likely originating from the porphyrin Q bands. It has to be noted that these are not only much more intense (relative to the Soret band) than in 'free' porphyrin materials but also shifted to higher wavelengths.

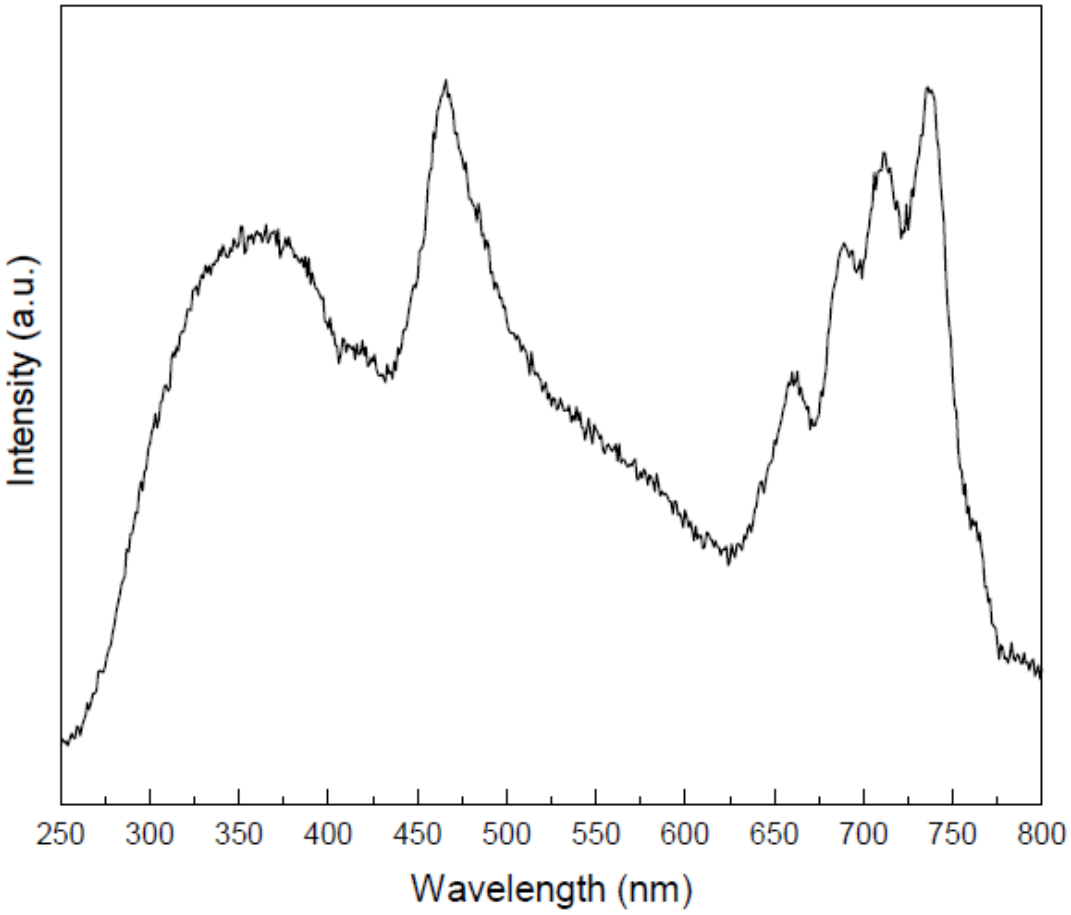


**Figure 5.8:** Excitation spectrum of Yb@Porph@PMO, the sample shows intense peaks at 450 nm and between 650 and 800 nm

For both excitation wavelengths, an emission spectra has been recorded (**Figure 5.9**), in which one broad peak is noted around 975 nm. This peak, characteristic for the $Yb^{3+}$ $^2F_{(5/2)} \longrightarrow {}^2F_{(7/2)}$ transition, is the only f-f transition observed, as the 4f configuration of $Yb^{3+}$ consists only of these two states. It has to be noted that a slight shift in the peak maxima is observed depending on the excitation wavelength. Where the 467 nm excited sample gives an emittance maximum around 985 nm, the 650 nm excited sample yields a maximum around 970 nm. The theoretical value for this peak is 995 nm [99], thus the 650 nm sample is shifted further away from the theoretical value and more influenced by the environment.

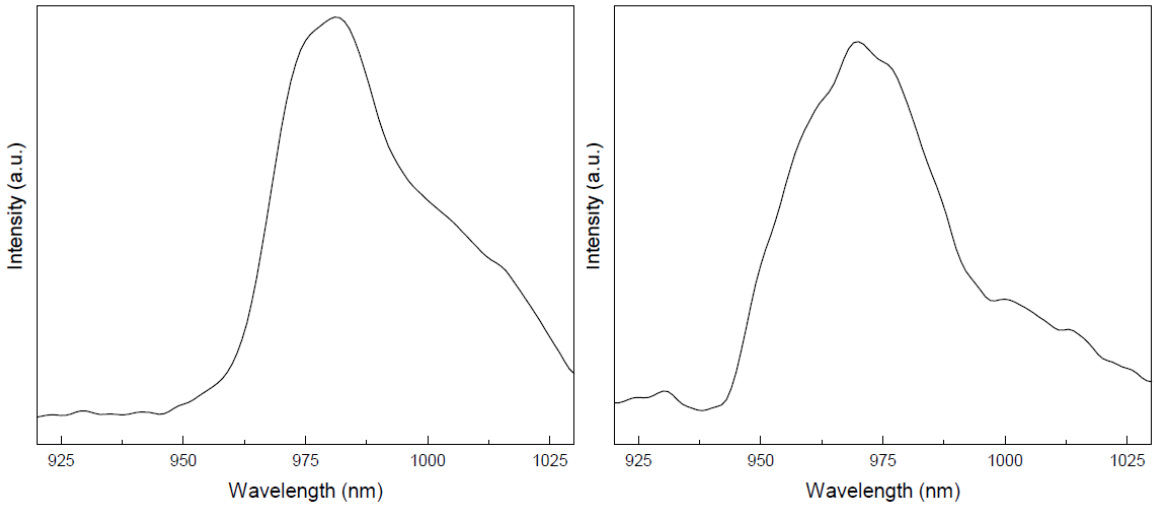


**Figure 5.9:** Emission spectra of Yb@Porph@PMO (left: excited at 467 nm, right: excited at 650 nm)

The decay profile of Yb@Porph@PMO has also been measured and is presented in **Figure 5.10**. Again curves could only be well fitted when using a double-exponential function. All decay times have been listed in **Table 5.4**.

When comparing these values, it should be noted that the excitation wavelength only has a minor influence on the materials decay profile. Both excitation wavelengths yielded quite good decay times, but excitation at 467 nm gave the best result. These values are in agreement with literature data, where lifetimes between 1 and 20 µs were reported as typical for porphyrin $Yb^{3+}$ complexes [113]. Most likely the hydrophobic PMO support material has a major influence on these decay profiles.

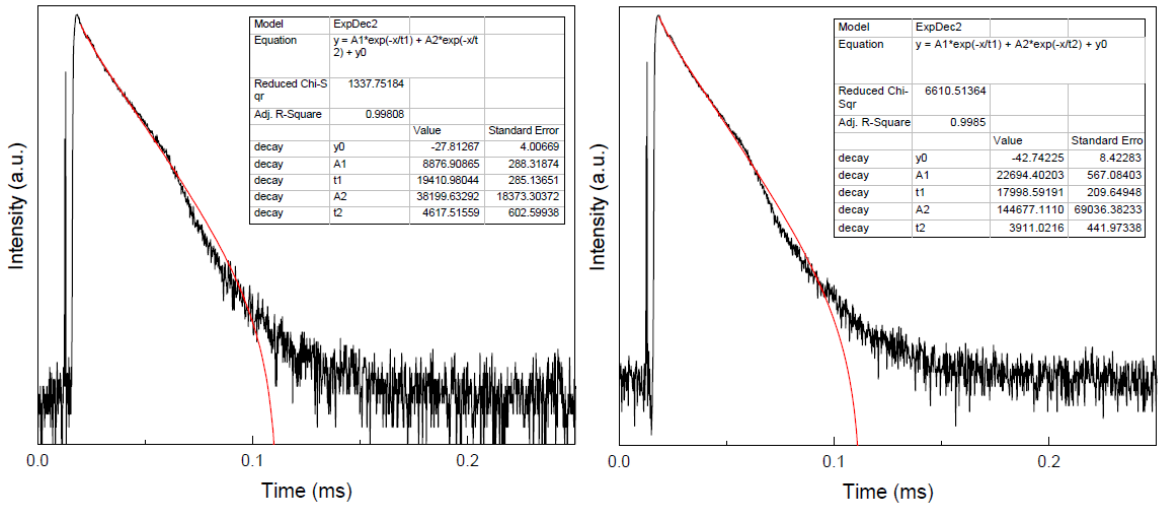


**Figure 5.10:** Luminescence decay profile of Yb@Porph@PMO (left: excited at 467 nm, right: excited at 650 nm)

**Table 5.4:** Luminescence decay times of Yb@Porph@PMO samples

| Sample | $\tau_1(\mu s)$ | $\tau_2(\mu s)$ | $\tau_{av}(\mu s)$ |
|---|---|---|---|
| 467 nm excitation | 19.4 | 4.6 | 11.9 |
| 650 nm excitation | 18.0 | 3.9 | 9.8 |

## 5.5 Conclusions

The monoallyl PMO has been proven as an efficient support material for luminescence applications. Multiple ligands can easily be attached, to yield completely different luminescence properties. The Pic@PMO material can be used to coordinate intense visual light emitting lanthanides to make visual light emitters or environment sensors. Both $Eu^{3+}$ and $Tb^{3+}$ have been (co)-grafted onto the support material and were proven to emit light efficiently. A combination of both cations yielded warm yellow light, attractive for in-house lighting. The Porph@PMO material has shown itself as a very interesting support for NIR emitting lanthanides like $Yb^{3+}$. The lanthanide coordinated material shows long decay times and can be efficiently excited around 700 nm, which is perfect for bio-medical applications. Moreover its properties are, to best of our knowledge, unprecedented for Yb@Porph materials.

# Appendix A

# Experimental

## A.1 PMO synthesis

### A.1.1 Synthesis of the AHETSCH precursor

The following chemicals were used:
1,1,3,3,5,5-hexaethoxytrisilacyclohexane (HETSCH, 95%, ABCR), t-BuLi (1.7 M in pentane, Sigma-Aldrich), allylbromide (99%, Sigma-Aldrich), anhydrous THF (99.9%, 250 ppm BHT as inhibitor, Sigma-Aldrich), $NaHCO_3$ (Chem lab, 99.5%+), silica gel (60Å, 60-200 $\mu$m, ROCC), EtOAc (99%, Carl Roth), hexane (mixture of isomers, Acros Organics).

In dried glassware and under Ar atmosphere, 60 mL of anhydrous THF was added, followed by 20 mL HETSCH. This solution was heavily stirred in a $CO_2$ - isopropanol icebath (-78.5 ℃) and 1 equivalent t-BuLi (18.7 mL) was added over 30 minutes, followed by 30 minutes of continued stirring. In a separate flask a solution of 40 mL anhydrous THF and 4.568 mL allylbromide (1.07 equivalents) was prepared and cooled to -78.5 ℃. Using a $CO_2$ cooled syringe, the HETSCH solution was added to the stirred allylbromide solution over 30 minutes. The resulting mixture was left to stir overnight with temperature gradually increasing. Afterwards, the resulting yellow solution was washed with 25 mL 0.2 w% $NaHCO_3$ solution and 2x50 mL $H_2O$. The solvent was evaporated (under reduced pressure) out of the resulting organic phase and a faint yellow oil was obtained. The resulting AHETSCH precursor was purified by flash column chromatography with hexane:EtOAc (10:1).

### A.1.2 Synthesis of the monoallyl ring PMO

The following chemicals were used:
Pluronic P123 (Mn = 5800 g/mol, Sigma-Aldrich), KCl (99.5%, Carl Roth), HCl (37%, Fisher

Chemical), Acetone (laboratory reagent grade, Fisher Chemical)

In a 50 mL flask, 0.375 g Pluronic P123 and 2.19 g KCl were dissolved in 11.25 mL $H_2O$. 0.9 mL of HCl (37%) was added and the mixture was stirred (600-800 RPM) to yield a clear blue solution. Subsequently, 0.5625 g AHETSCH was added to yield a molar composition of AHETSCH:$H_2O$:P123:HCl:KCl 1:500:0.0517:8.62:23.5. The mixture was directly brought to stirring at 45 ℃ for 3 hours, after which the stirring was turned off and the temperature was raised to 95 ℃ to let the material age for 24 hours. A white precipitate was formed and filtered off. The powder was washed with 3x25 mL $H_2O$ and 3x25 mL acetone and subsequently the template was removed using 6 hour Soxhlet extraction in acetone. The yielded white powder was dried overnight at 120 ℃ in vacuum.

## A.2 Coupling of Ligands to the PMO

### A.2.1 Acid chloride preparation

The following chemicals were used:
4,4',4",4"'-(Porphine-5,10,15,20-tetrayl)tetrakis(benzoic acid (> 97 %, TCI), Picolinic Acid (99%, Acros Organics), $SOCl_2$ (99.5+%, Acros Organics).

Porphyrin (100 mg, 0.126 mmol) or Picolinic acid (155 mg, 1.26 mmol) were dissolved in 5 mL $SOCl_2$ in dried glassware. The mixture was refluxed for 4 hours at 80 ℃ under Ar atmosphere. The remaining solvent after reaction was removed under reduced pressure.

### A.2.2 Amide coupling

The following chemicals were used:
Cysteamine (> 95% TCI), $CHCl_3$ (Laboratory reagent grade, Fisher Chemical), $NEt_3$ ($\geqslant$ 99%, Sigma-Aldrich), $NaHCO_3$ (99.5+%, Chem-lab), NaCl (> 99.5%, Fisher Chemical), $MgSO_4$ (99% anhydrous, Fisher Chemical)

In a general procedure, chlorinated porphyrin/picolinic acid was dissolved in 10 mL $CHCl_3$. The mixture was stirred at 0 ℃ under Ar atmosphere. Separately, 1 equivalent of cysteamine was dissolved in 10 mL $CHCl_3$ and 2 equivalents $NEt_3$, this was drop wise added to the porphyrin/picoline solution. The mixture was covered with Al-foil and stirred for 2 hours. The resulting solution was then washed with $NaHCO_3$ and brine, before drying of the organic phase over $MgSO_4$ (this washing step was not used for the porphyrin mixture). After evaporation of the organic phase, a light yellow (picoline) or dark purple (porphyrine) powder was obtained.

### A.2.3 Click on the PMO

The following chemicals were used:
2-hydroxy-4'-(2-hydroxyethoxy)-2-methylpropiophenone (Irgacure 2959, 98%, Sigma-Aldrich), $NaH_2PO_4 \cdot 2\,H_2O$ (Typanalyse, Ferak Berlin), $Na_2HPO_4$ (98 %, Sigma-Aldrich), Acetone (laboratory reagent grade, Fisher Chemical)

A pH 7 phosphate buffer was prepared by dissolving 0.655 g $NaH_2PO_4 \cdot 2\,H_2O$ (4.2 mmol) and 0.696 g $Na_2HPO_4$ (5.8 mmol) in water, the resulting solution was flushed with Ar. 50 mL Irgacure 2959 (0.22 mmol, excess), was dissolved in the phosphate buffer and flushed with Ar. In a general procedure, 100 mg of monoallyl ring PMO and 0.14 mmol of the yielded amides (25.5 mg picolin compound or 126.735 mg porphyrin compound) were added to this Irgacure initiator. The resulting suspension was mixed in ultrasonic bath and treated for 3 hours in a home-made UV reactor ($\lambda$ = 360 nm). The product was filtered of and washed with $H_2O$ and acetone. Subsequently, to remove all leftover reagents, the powder was soxhlet extracted using acetone for 6 hours. Finally, the yielded product was dried overnight at 110 ℃.

## A.3 Coordination of metals

### A.3.1 Coordination of $Ln^{3+}$

The following chemicals were used:
$Ln(NO_3)_3 \cdot 6\,H_2O$ (Ln = Eu, Tb, Yb) (99.9% Sigma Aldrich), Methanol (96%, VWR)

In a general procedure, an excess of the appropriate lanthanide salt was dissolved in 5 mL of methanol and added to a pyrex tube containing the PMO material. The tube was closed and treated with ultrasounds for 20 minutes, before leaving for 24 hours at room temperature to soak. Afterwards, the mixture was heated for 24 hours at 85 ℃. After cooling to room temperature, the resulting powder was filtered of and washed with methanol to remove adsorbed lanthanide ions. Finally, the resulting powder was dried at 60 ℃.

### A.3.2 Coordination of $Co^{2+}$

The following chemicals were used:
$Co(OAc)_2 \cdot 4\,H_2O$ (99%, Honeywell Riedel-de Haën AG), DMF (Analytical reagent grade, Fisher Chemical)

In a general procedure, equimolar amounts of the ligand and $Co(OAc)_2 \cdot 4\,H_2O$ are dissolved in DMF. The mixture is refluxed overnight at 160 ℃. Afterwards, the obtained powder is

filtered and washed with DMF. The product is purified using Soxhlet extraction with acetone (6 hours.)

## A.4 Catalysis

The following chemicals were used:
Epichlorohydrin (99.9%, Fluorochem), mesitylene (98%, Sigma-Aldrich), $CH_2Cl_2$ (HPLC grade, Fisher Chemical), DMAP ($\geqslant$ 98 %, Fluka Analytical), $CO_2$ (Air liquide Belgium), acetone (laboratory reagent grade, Fisher Chemical)

In a general procedure, a 125 mL stainless steel Parr reactor was loaded with 10 mg catalyst, 1 mg DMAP, 46.26 mg epichlorohydrin and 2 mL $CH_2Cl_2$. The reaction vessel was subsequently flushed and placed under pressure with $CO_2$, whereafter it was heated to reach 120 ℃ and the desired pressure. After the desired reaction time had passed, the mixture was allowed to cool down to $\sim$ 40 ℃ and the resulting mixture was transferred to a 25 mL flask using acetone. The acetone was removed under reduced pressure to yield the resulting mixture for analysis.

# Appendix B

# Characterization techniques

To obtain internal surface area ($S_{BET}$ via BET theory) and pore size distribution ($d_{BJH}$, BJH theory), $N_2$-sorption experiments were performed on a micromeretics Tristar II at 77 K. Diffuse Reflectance Infrared Fourier Transform Spectroscopy (DRIFTS) measurements were done using a Nicolett 6700 FTIR spectrometer equipped with a Greasby-Specac diffuse reflectance cell, modified to measure samples at 20 - 300 ℃ under vacuum. Pore ordening was confirmed using PXRD on a Thermo Scientific ARL X'TRA X-ray diffractometer using Cu K$\alpha$ radiation of 40 kV and 30 mA. CHNS analysis was performed on a Thermo Flash 200 elemental analyser with $V_2O_5$ as catalyst. The chemical structure of reagents and catalytic products were analyzed using $^1$H NMR in $CDCl_3$ or DMSO, on a Bruker 300 MHz AVANCE spectrometer with chemical shifts ($\delta$) expressed in ppm relative to a tetramethylsilane standard. Co loadings were studied by X-ray Fluorescence (XRF) on a Rigaku NEX CG with an Al source and compared to Sr-K$\alpha$ as internal standard. TEM pictures were taken on a JEOL JEM 2200-FS TEM and TGA measurements were performed using a Netzsch STA 449 F3 (Jupiter) apparatus. GC/MS spectra were obtained on a Agilent 6890 GC equipped with a DB5ms column (60m x 0.25mm x 0.25µm), coupled with an Agilent 5973 MSD with EI ionisation.

Luminescence properties were measured using an Edinburgh Instruments FLSP920 UV-vis-NIR spectrometer setup, equipped with a 450W Xe lamp as steady state excitation source. Luminescence decay times of the sample were obtained via a 60W pulsed Xe lamp, operating at a frequency of 100 Hz. PL decay times of the ungrafted samples were recorded using using a Supercontinuum white light laser for TCSPC (Time Correlated Single Photon Counting, 80 ps - hundreds of ns). Emission signals in the visible range were detected using a Hamamatsu R928P photomultiplier tube, a Hamamatsu R5509-72 photomultiplier was used for signals in the NIR region. To properly compare results, all setings were kept equal between measurements (same amounts, all samples put between quartz plates, same split size, step and dwell

time). All emission spectra have been corrected for detector response.

# Appendix C

# Spectroscopic data

## C.1 NMR & GC spectra

### C.1.1 PMO synthesis

**Pure PMO precursor (literature)**: In **Figure C.1**, the following peaks were assigned: (300 MHz, $CDCl_3$) $\delta = 6.01$ (ddt, $J$=17.0, 9.9, 7.0, 1H, $CH_2CH{=}CH_2$, hydrogen f), 5.00 (ddd, $J$=17.0, 3.6, 1.4, 1H, $CH{=}CH_2$, hydrogen g), 4.87 (ddt, $J$=10.0, 2.1, 1.0, 1H, $CH{=}CH_2$, hydrogen g), 3.85 - 3.71 (m, 12H, $OCH_2$, hydrogen b), 2.41 - 2.32 (m, 2H, $CHCH_2CH{=}CH_2$, hydrogen e), 1.26 - 1.16 (m, 18H, $OCH_2CH_3$, hydrogen a), 0.38 (t, $J$=6.4, 1H, $CH(Si)_2(CH_2CH{=}CH_2)$, hydrogen d), 0.20 - 0.02 (m, 4H, $SiCH_2Si$, hydrogen c). * is the signal from the NMR solvent ($CDCl_3$), # was assigned to leftover THF used as reaction solvent.

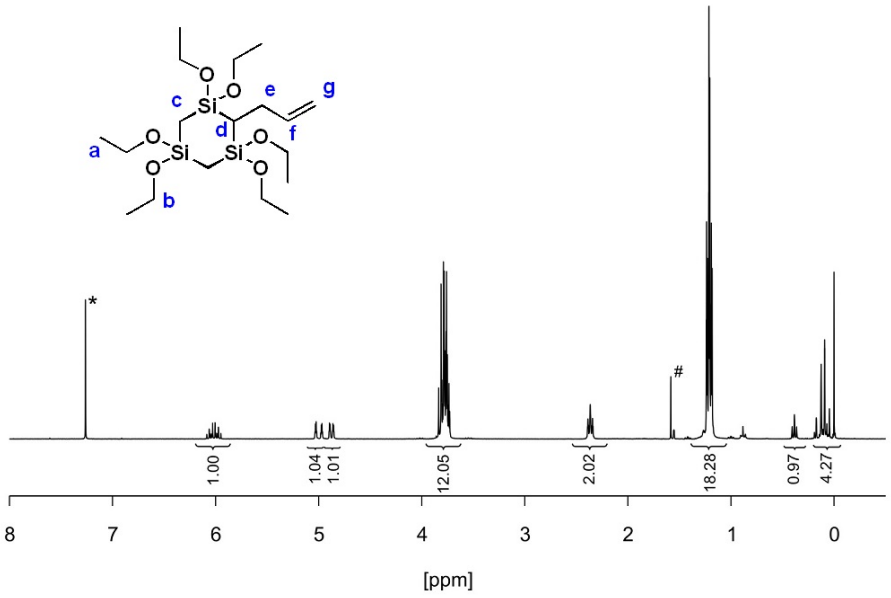


**Figure C.1:** $^1$H NMR of the pure PMO precursor[10]

**PMO Precursor after synthesis**: A mixture of non allylated and mono allyl ring PMO were obtained as well as some impurities. In **Figure C.2**, the following peaks were assigned: (300 MHz, $CDCl_3$) $\delta$ = 5.92 (ddt, $J$=17.0, 9.9, 7.0, 1H, $CH_2CH{=}CH_2$, hydrogen f), 4.9 (d, $J$=18, 1H, $CH{=}CH_2$, hydrogen g), 4.78 (d, $J$=10.5, 1H, $CH{=}CH_2$, hydrogen g), 3.78 - 3.62 (m, 12H, $OCH_2$, hydrogen b), 2.30 - 2.24 (t, $J$ = 6, 2H, $CHCH_2CH{=}CH_2$, hydrogen e), 1.16 - 1.08 (m, 18H, $OCH_2CH_3$, hydrogen a), 0.29 (t, $J$=6.4, 1H, $CH(Si)_2(CH_2CH{=}CH_2)$, hydrogen d), 0.12 - -0.05 (m, 4H, $SiCH_2Si$, hydrogen c).

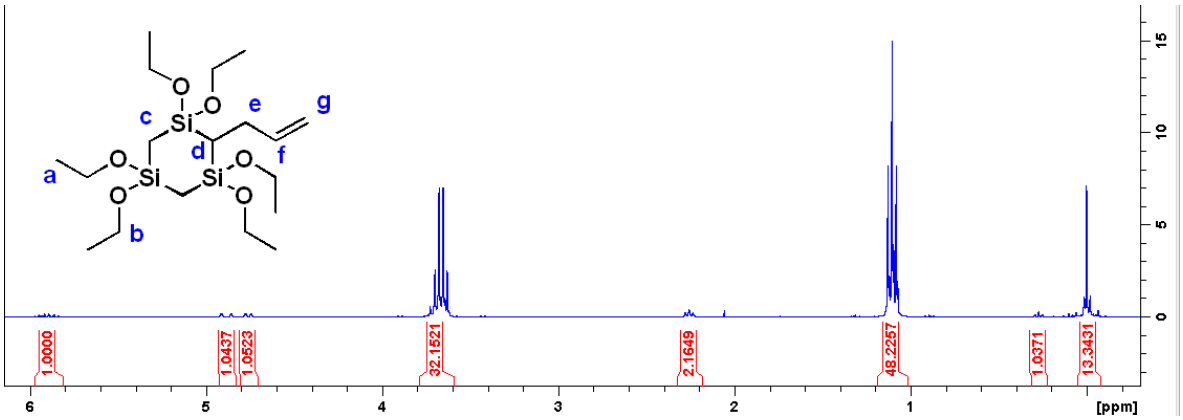


**Figure C.2:** $^1$H NMR of the PMO precursor mixture after synthesis

### C.1.2 Coupling of picolinic acid with PMO

**Pure Picolinic acid**: the $^1$H NMR spectrum of the commercially bought picolinic acid was measured (**Figure C.3** and peaks were assigned (300 MHz, d-DMSO): $\delta$ = 8.71 (dq, $J$ = 4.68, 0.92, 1H, hydrogen 1), 8.05 (dt, $J$ = 7.83, 1.29, 1H, hydrogen 4), 7.99 (td, $J$ = 7.5, 1.74, 1H, hydrogen 3), 7.63 (ddd, $J$ = 7.35, 4.7, 1.5, 1H, hydrogen 2). A large acetone peak was observed around $\delta$ = 2.08 due to incomplete drying of the tube. Outside of the frame shown here, around $\delta$ = 13.14, a broad peak assigned to the acid hydrogen was observed, its integrated intensity was 0.9.

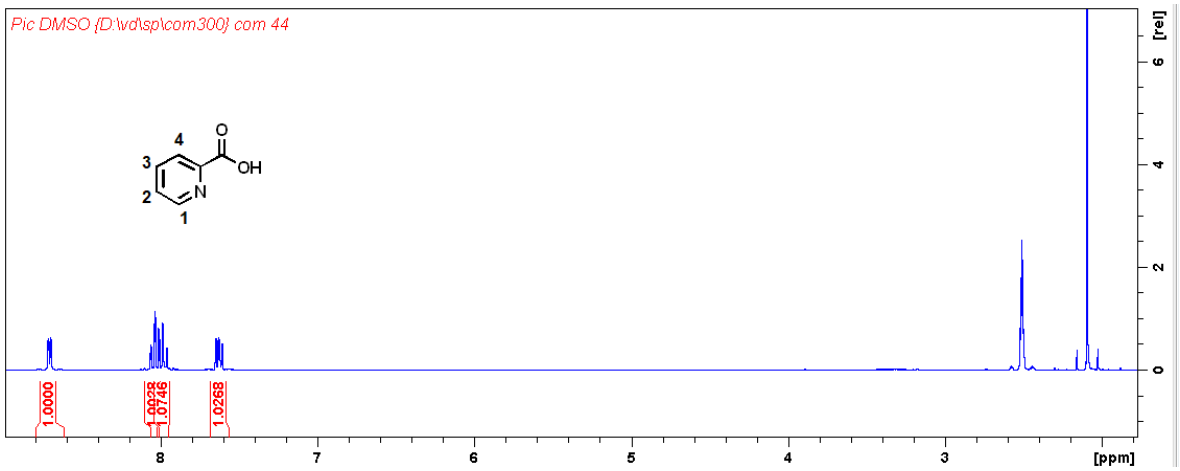


**Figure C.3:** $^1$H NMR of pure Picolinic Acid

**PicCys**: the synthesis procedure to form PicCys was checked with $^1$H NMR shown in **Figure C.4**. The following peaks were assigned (300 MHz, $CDCl_3$): $\delta$ = 8.56 (dq, $J$ = 4.6, 0.9, 1H, hydrogen 1), 8.18 (dt, $J$ = 7.85, 1.1, 1H, hydrogen 4), 7.85 (td, $J$ = 7.65, 1.8, hydrogen 3), 7.43 (m, 1H, hydrogen 2), 3.67 (m, 2H, OC−HN−C$H_2$CH$_2$−S, hydrogen 5), 2.78 (m, 2H, C−HN−CH$_2$C$H_2$−S, hydrogen 6). The amide and thiol peaks were not observed, a peak due to remaining water from purification at $\delta$ = 1.56 was assigned.

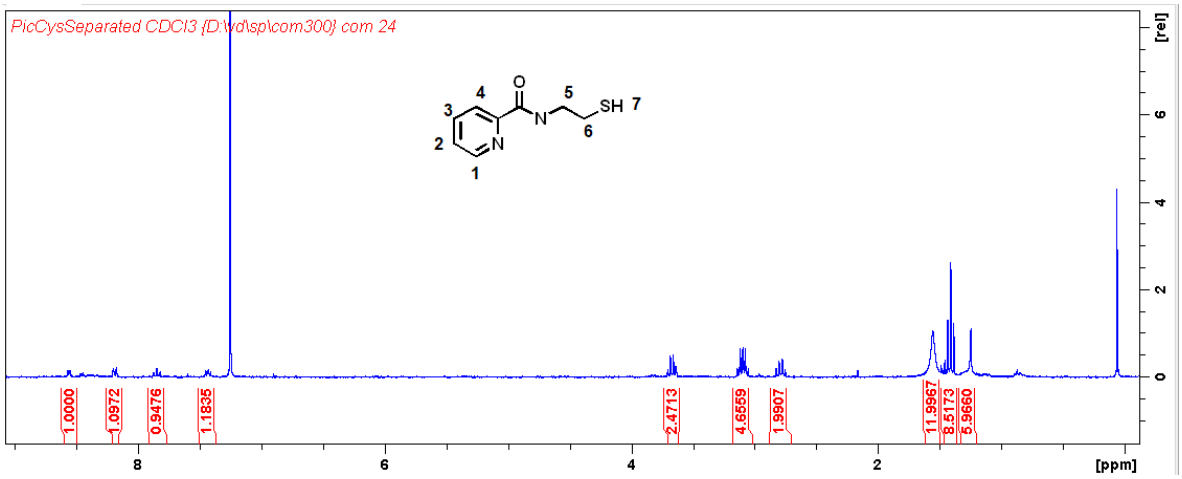


**Figure C.4:** $^{1}$H NMR of the synthesized PicCys

### C.1.3 Coupling of porphyrin with PMO

**Pure porphyrin**: the $^{1}$H NMR spectrum of the commercially bought 4,4',4",4"'-(Porphine-5,10,15,20-tetrayl)tetrakis(benzoic acid) is presented in **Figure C.3**. The following peaks were assigned (300 MHz, DMSO): $\delta$ = 13.3 (s, 4H, carboxylic acid hydrogens), 8.86 (t, 20, 8H, pyrrolle ring hydrogens), 8.37 (o, 6, 16H, benzene ring hydrogens), 3.31 (t, 22.5, 18H), 2.08 (t, 21, 9H). The last two named peaks could not be assigned to any hydrogen in the porphyrin structure.

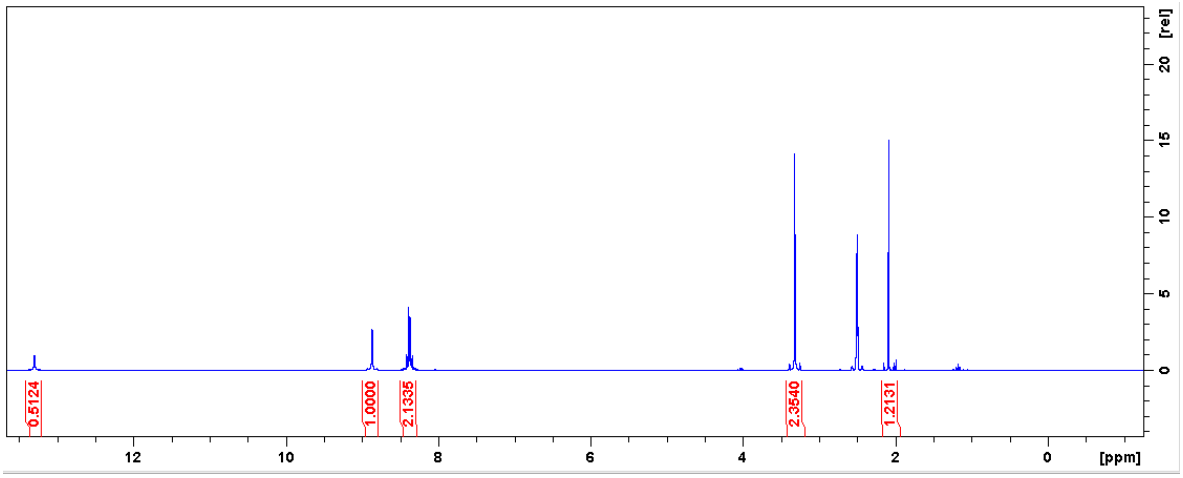


**Figure C.5:** $^{1}$H NMR of pure 4,4',4",4"'-(Porphine-5,10,15,20-tetrayl)tetrakis(benzoic acid)

**PicCys**: the formed PorphCys was measured using $^{1}$H NMR shown in **Figure C.4**. The following peaks were identified (300 MHz, $CDCl_3$): $\delta$ = 8.81 (s, 1H), 8.39 (m, 3H), 8.16 (d,

8, 3H), 8.1 (d, 9, 1H), 2.37 (s, 11H), 1.93 (s, 21H). No peak assignment was possible. Around 2.96 and 1.26 ppm, two clear $NEt_3$ peaks were noted.

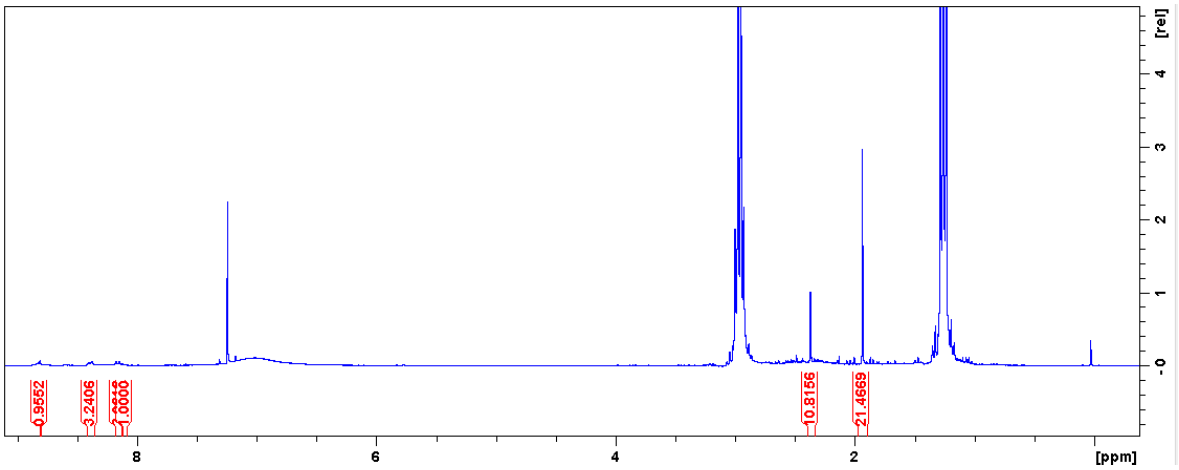


**Figure C.6:** $^1$H NMR of the synthesized PorphCys

### C.1.4 Catalysis

**GC/MS**: A GC/MS spectrum of a first catalytic test (Parameters: Co@Porph@PMO, 1 hour, 6 bar $CO_2$, 120 ℃) was measured. Three peaks were obtained. A broad, low intensity peak at 7.22 which was left unassigned but most likely resulted from a solvent (as the obtained mass is too low to belong to one of the reactants), a much intenser peak at 8.10 assigned to mesitylene (added as internal standard) and an even more intense peak at 10.27, assigned to the reaction product. The GC/MS spectrum is presented in **Figure C.7**, assignment of the peaks in **Figure C.8**.

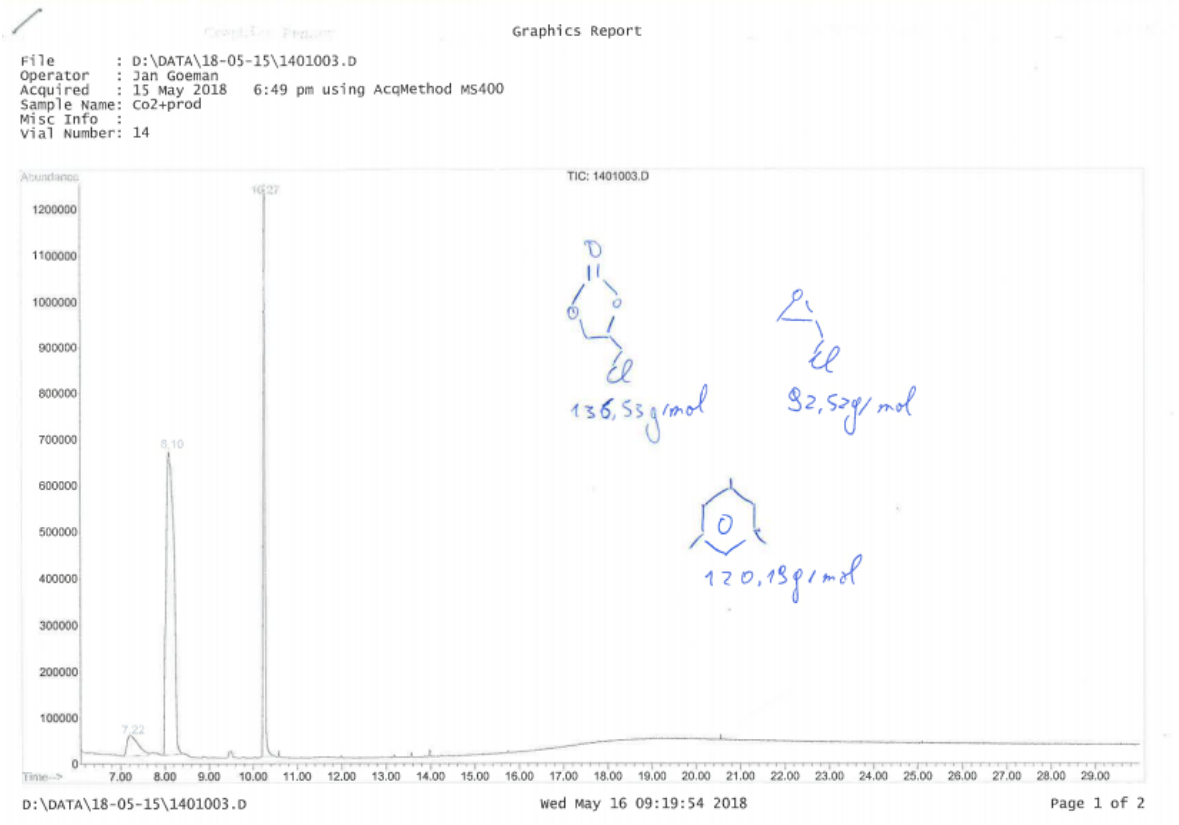


**Figure C.7:** GC/MS spectrum of the first catalytic test with three observed peaks (time = 7.22, 8.10 and 10.27). The chemical structure and molar mass of starting material, internal standard and reaction product are drawn on the spectrum.

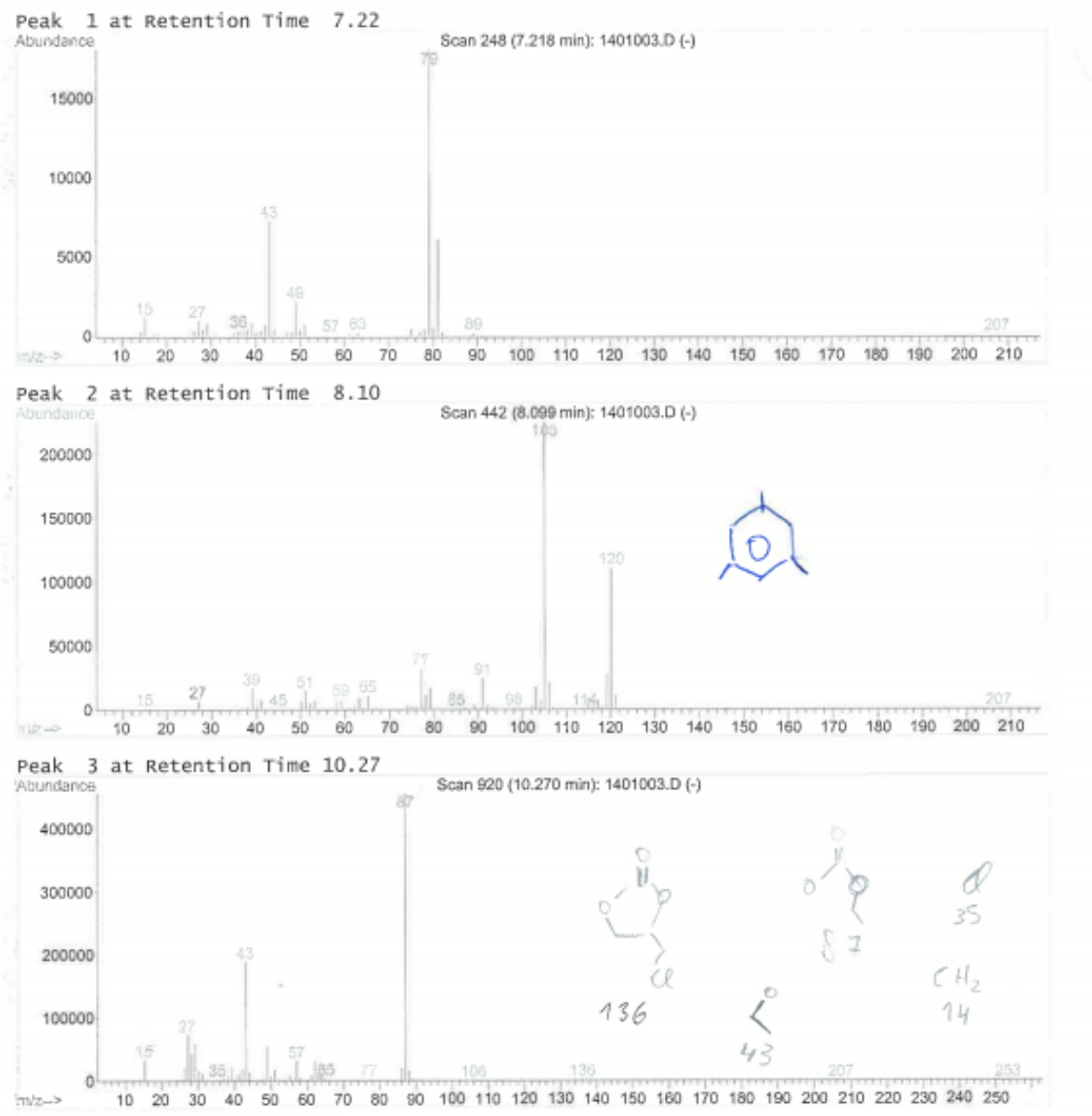


**Figure C.8:** Observed MS fragments of the three GC/MS peaks. The first peak is left unassigned, the second one is assigned to the internal standard mesitylene (drawn in the spectrum) and the tird peak is assigned to the reaction product (Some fragments are drawn, each fragments m/z is given)

**Epichlorohydrin**: The $^1$H NMR spectrum of commercially bought epichlorohydrin was measured and is presented in **Figure C.9**. The following peaks were assigned (300 MHz, $CDCl_3$):

$\delta$ = 3.52 (m, 2H, Cl−$CH_2$−CHC$H_2$O), 3.18 (m, 1H, ClC$H_2$−$CH$−C$H_2$O), 2.83 (m, 1H, ClC$H_2$CH−$CH_2$−O), 2.63 (m, 1H, ClC$H_2$CH−$CH_2$−O).

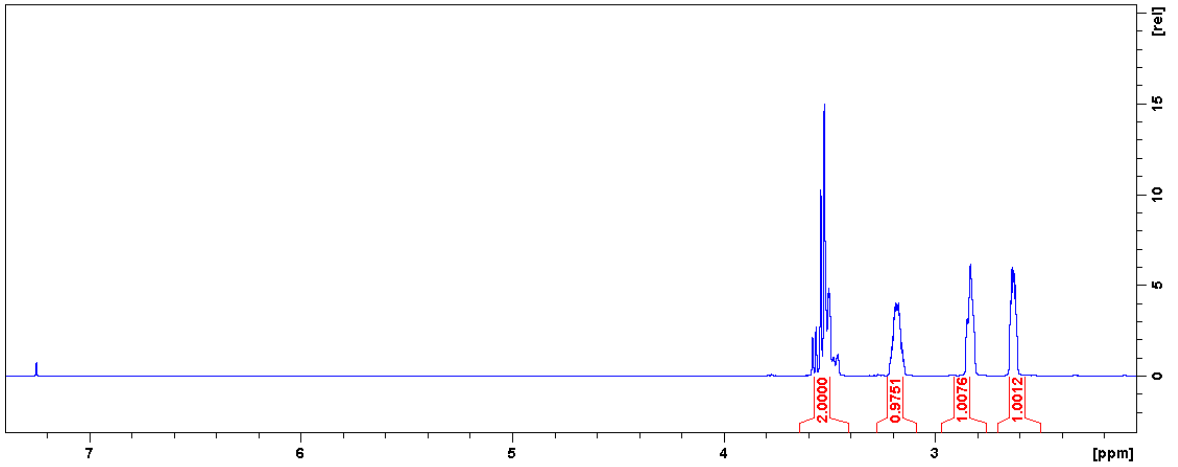


**Figure C.9:** $^1$H NMR of the pure Epichlorohydrin

**Co@Porph**: The $^1$H NMR spectrum of the homogeneous catalytic test is presented in **Figure C.10**. The following peaks were assigned (300 MHz, $CDCl_3$): $\delta$ = 6.80 (s, 3H, mesitylene aromatic hydrogens), 4.95 (m, 1H, ClC$H_2$−$CH$−C$H_2$OCOO), 4.59 (t, 9, 1H, ClC$H_2$CH−$CH_2$−OCOO), 4.41 (dd, 9, 6, 1H, ClC$H_2$CH−$CH_2$−OCOO), 3.75 (m, 2H, Cl−$CH_2$−CHC$H_2$OCOO), 2.27 (s, 9H, mesitylene methyl groups). The unassigned peaks do not belong to product or reagent and thus result most likely from contamination, no product peaks were observed.

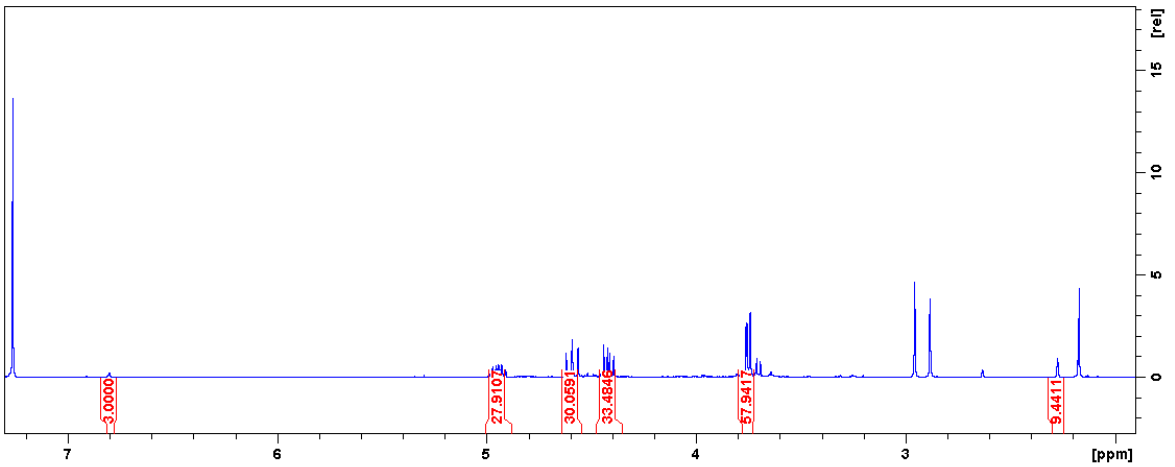


**Figure C.10:** $^1$H NMR of reaction mixture obtained by using Co@Porph as catalyst

**Co@Pic@PMO 6 bar**: The catalytic test using Co@Pic@PMO and 6 bar $CO_2$ was analyzed using $^1$H NMR (see **Figure C.11**). The following peaks were assigned (300 MHz, $CDCl_3$): $\delta$ = 6.71 (s, 3H, mesitylene aromatic hydrogens), 4.88 (m, 1H, $ClCH_2-CH-CH_2OCOO$), 4.48 (t, 6, 1H, $ClCH_2CH-CH_2-OCOO$), 4.28 (dd, 9, 6, 1H, $ClCH_2CH-CH_2-OCOO$), 3.67 (dd, 11, 5, 2H, $Cl-CH_2-CHCH_2OCOO$), 3.54 (m, 2H, $Cl-CH_2-CHCH_2O$), 3.16 (m, 1H, $ClCH_2-CH-CH_2O$), 2.77 (t, 5, 1H, $ClCH_2CH-CH_2-O$), 2.58 (t, 3, 1H, $ClCH_2CH-CH_2-O$). The mesitylene methyl groups peak could not be observed, as it was overlapped by the acetone peak. The beginproduct intensities were very low and the peaks hard to find, multiple unassigned peaks resulted most likely from contamination.

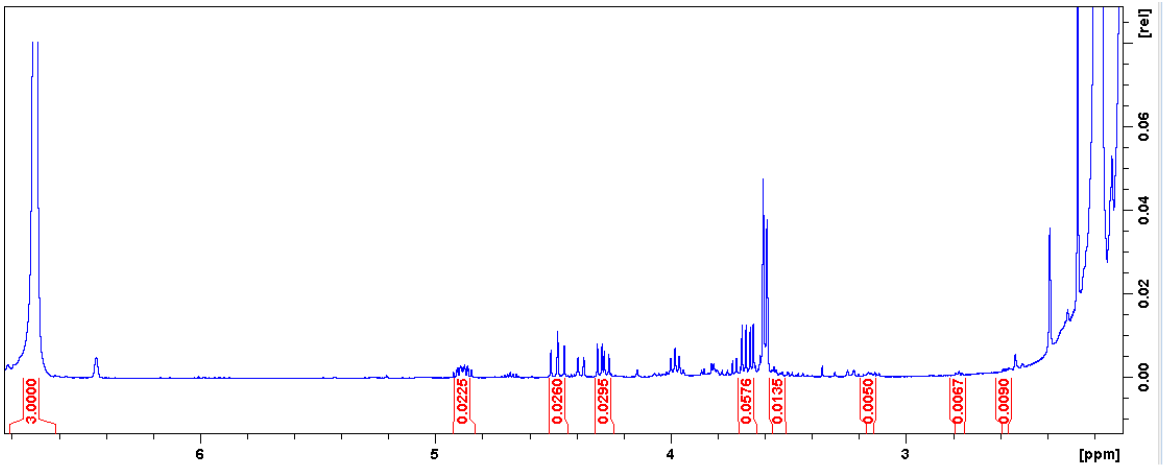


**Figure C.11:** $^1$H NMR of reaction mixture obtained by using Co@Pic@PMO as catalyst and 6 bar $CO_2$

**Co@Pic@PMO 5 bar**: The $^1$H NMR spectrum of the catalytic test using Co@Pic@PMO and 5 bar is presented in **Figure C.12**). The following peaks were assigned (300 MHz, $CDCl_3$): $\delta$ = 4.67 (m, 1H, $ClCH_2-CH-CH_2OCOO$), 4.30 (t, 6, 1H, $ClCH_2CH-CH_2-OCOO$), 4.06 (dd, 9, 6, 1H, $ClCH_2CH-CH_2-OCOO$), 3.51 (dd, 13, 5, 2H, $Cl-CH_2-CHCH_2OCOO$), 3.15 (m, 1H, $ClCH_2-CH-CH_2O$), 2.85 (m, 1H, $ClCH_2CH-CH_2-O$), 2.51 (s, 1H, $ClCH_2CH-CH_2-O$). No mesitylene was added in this sample. Multiple unassigned peaks were observed, most likely resulting from contamination. The beginproduct intensities were very low and the peaks hard to find, only three of four peaks were observed and assigned.

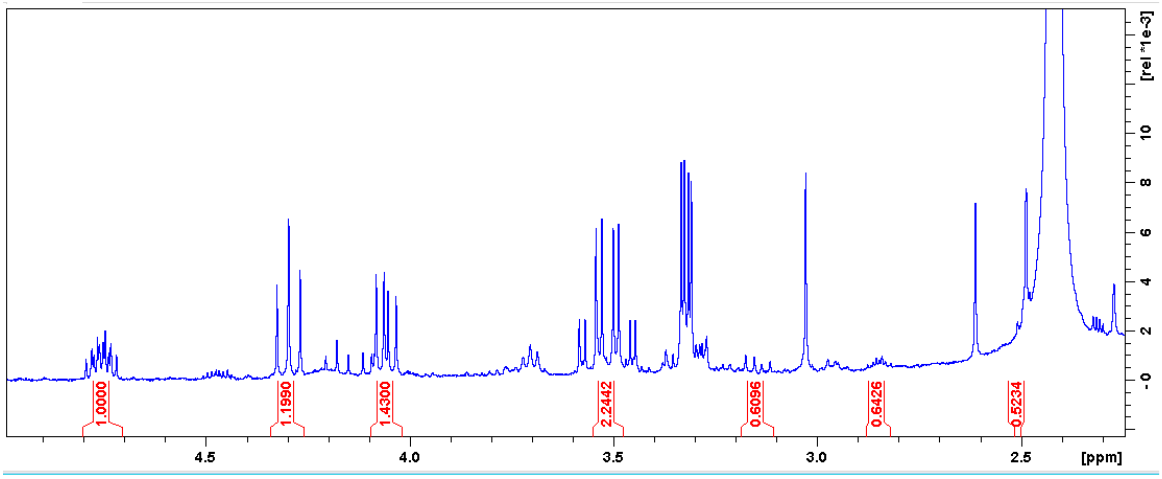


**Figure C.12:** $^{1}$H NMR of reaction mixture obtained by using Co@Pic@PMO as catalyst and 5 bar $CO_2$

**Co@Pic@PMO 4 bar**: Co@Pic@PMO was tested as a catalyst using 4 bar $CO_2$, the obtained $^{1}$H NMR spectrum is presented in **Figure C.13**). The following peaks were assigned (300 MHz, $CDCl_3$): $\delta$ = 6.79 (s, 3H, mesitylene aromatic hydrogens), 4.93 (m, 1H, $ClCH_2-\mathit{CH}-CH_2OCOO$), 4.56 (t, 9, 1H, $ClCH_2CH-\mathit{CH_2}-OCOO$), 4.38 (dd, 9, 6, 1H, $ClCH_2CH-\mathit{CH_2}-OCOO$), 3.75 (m, 2H, $Cl-\mathit{CH_2}-CHCH_2OCOO$), 3.21 (m, 1H, $ClCH_2-\mathit{CH}-CH_2O$). The mesitylene methyl groups peak could not be observed, as it was overlapped by the acetone peak. The beginproduct peaks were again only observed in the noise, only one peak could be found. Multiple unassigned peaks most likely result from contamination.

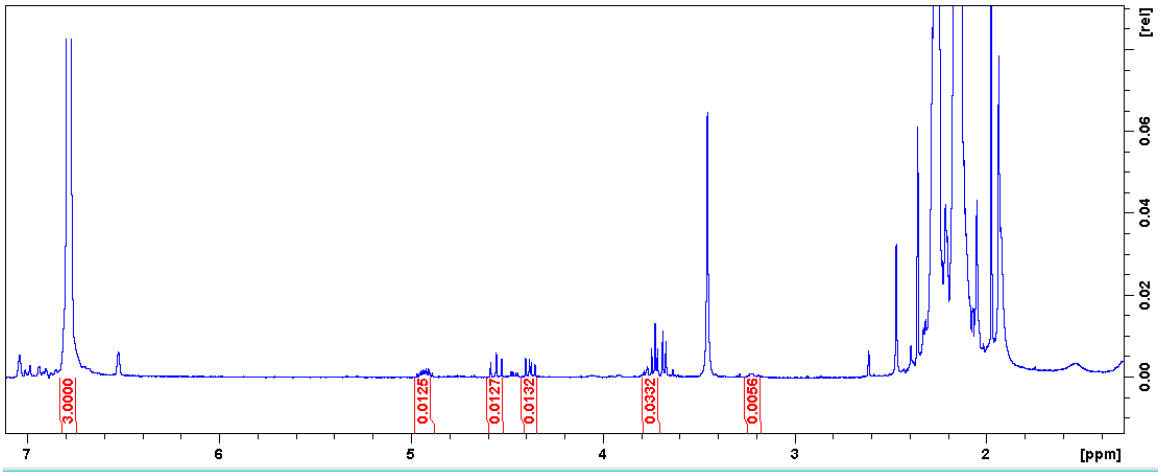


**Figure C.13:** $^{1}$H NMR of reaction mixture obtained by using Co@Pic@PMO as catalyst and 4 bar $CO_2$

**Co@Porph@PMO 6 bar**: The obtained $^{1}$H NMR spectrum for the catalytic test using 6 bar $CO_2$ and Co@Porph@PMO is presented in **Figure C.14**). The following peaks were assigned (300 MHz, $CDCl_3$): $\delta$ = 4.95 (m, 1H, $ClCH_2-CH-CH_2OCOO$), 4.59 (t, 9, 1H, $ClCH_2CH-CH_2-OCOO$), 4.42 (dd, 9, 6, 1H, $ClCH_2CH-CH_2-OCOO$), 3.75 (m, 2H, $Cl-CH2-CHCH_2OCOO$), 3.64 (m, 2H, $Cl-CH_2-CHCH_2O$), 3.25 (m, 1H, $ClCH_2-CH-CH_2O$), 2.73 (m, 1H, $ClCH_2CH-CH2-O$), 2.63 (s, 1H, $ClCH_2CH-CH_2-O$). No mesitylene was added in this sample, beginning product peaks were only found between unassigned peak resulting from contaminations.

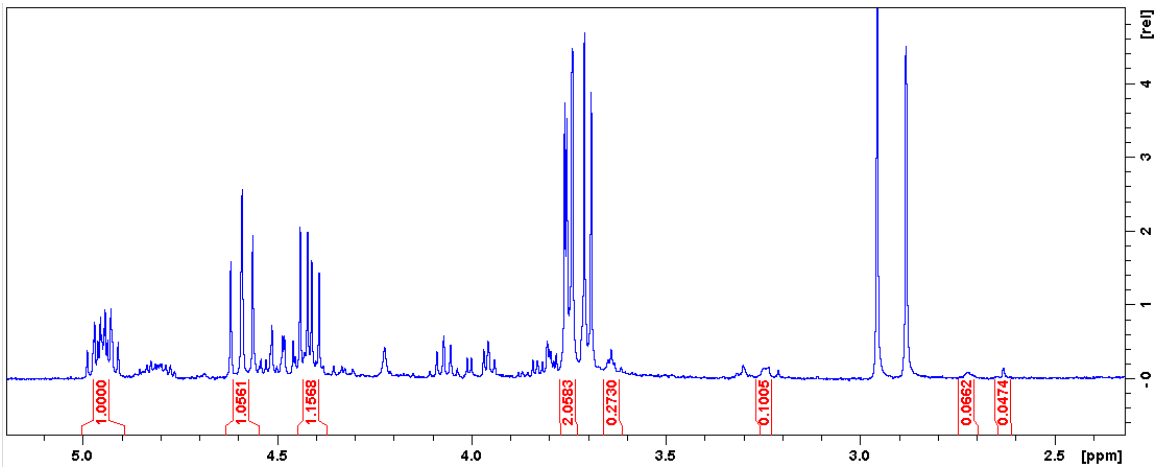


**Figure C.14:** $^{1}$H NMR of reaction mixture obtained by using Co@Porph@PMO as catalyst and 6 bar $CO_2$

**Co@Porph@PMO 4 bar**: A catalytic test was performed using Co@Porph@PMO as a catalyst combined with 4 bar $CO_2$, the resulting $^1H$ NMR spectrum is shown in **Figure C.15**. The following peaks were assigned (300 MHz, $CDCl_3$): $\delta$ = 4.94 (m, 1H, $ClCH_2-CH-CH_2OCOO$), 4.57 (t, 9, 1H, $ClCH_2CH-CH_2-OCOO$), 4.39 (dd, 9, 6, 1H, $ClCH_2CH-CH_2-OCOO$), 3.73 (t, 6, 2H, $Cl-CH_2-CHCH_2OCOO$), 3.62 (m, 2H, $Cl-CH_2-CHCH_2O$), 3.21 (m, 1H, $ClCH_2-CH-CH_2O$). Like in the previous sample, no mesitylene was added. Furthermore, only two starting material peaks were found between unassigned contamination peaks.

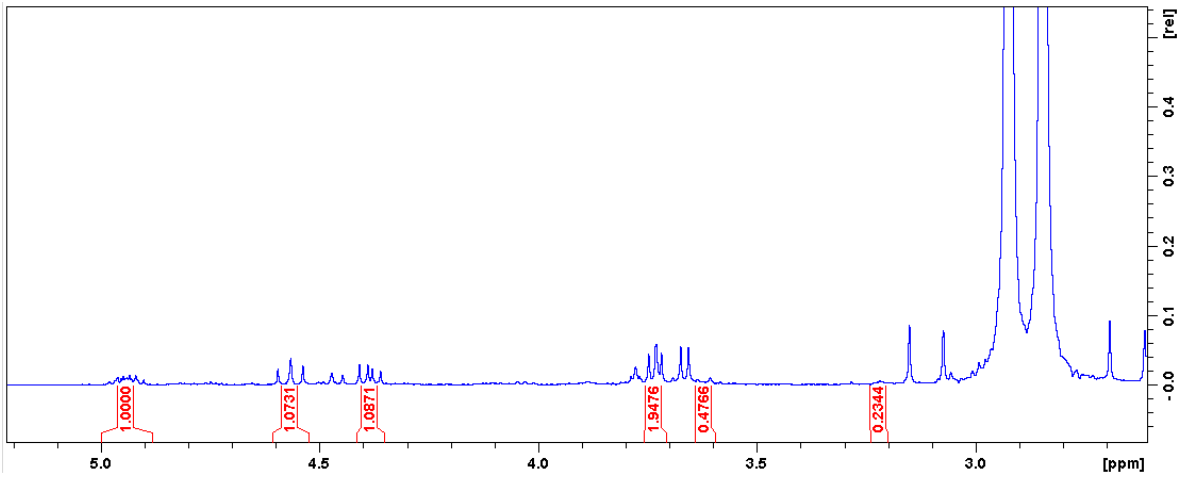


**Figure C.15:** $^1$H NMR of reaction mixture obtained by using Co@Porph@PMO as catalyst and 4 bar $CO_2$

**Co@Porph@PMO 2 bar**: Co@Porph@PMO was used as a catalyst under a $CO_2$ pressure of 2 bars. The resulting $^1H$ NMR spectrum is presented in **Figure C.16**. The following peaks were assigned (300 MHz, $CDCl_3$): $\delta$ = 4.77 (m, 1H, $ClCH_2-CH-CH_2OCOO$), 4.31 (t, 9, 1H, $ClCH_2CH-CH_2-OCOO$), 4.08 (dd, 9, 6, 1H, $ClCH_2CH-CH_2-OCOO$), 3.55 (m, 2H, $Cl-CH_2-CHCH_2OCOO$), 3.33 (m, 2H, $Cl-CH_2-CHCH_2O$), 3.06 (s, 1H, $ClCH_2-CH-CH_2O$). Two starting material peaks are clearly observed in this sample, indicating reduced conversion, the two lower lying peaks are not visible due to a very intense broad overlapping peak. No mesitylene was added in this sample.

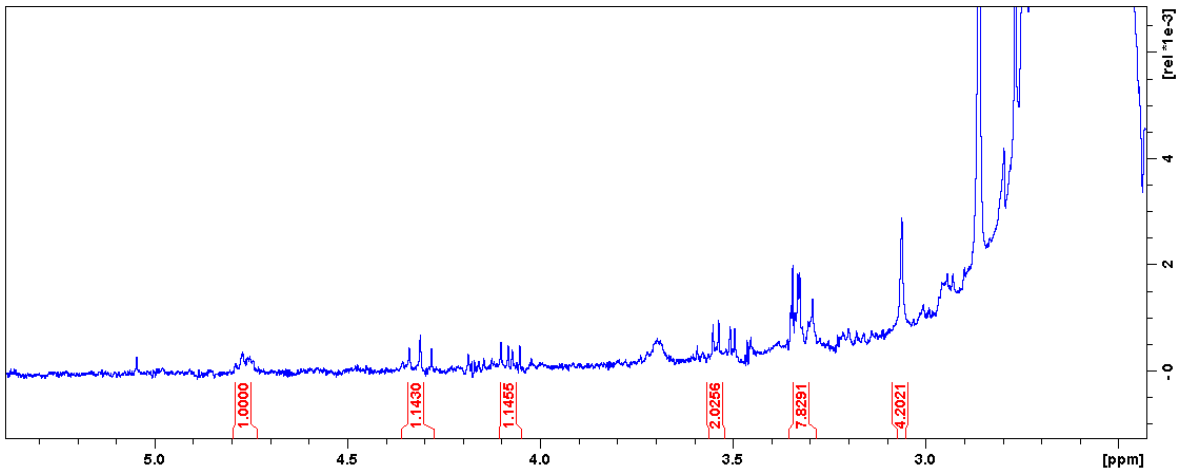


**Figure C.16:** $^{1}$H NMR of reaction mixture obtained by using Co@Porph@PMO as catalyst and 2 bar $CO_2$

**Co@Porph@PMO reuse**:The second catalytic run of Co@Porph@PMO was analyzed using $^{1}H$ NMR. In the resulting spectrum (**Figure C.17**), following peaks were assigned (300 MHz, $CDCl_3$): $\delta = 6.76$ (s, 3H, mesitylene aromatic hydrogens), 4.94 (m, 1H, $ClCH_2{-}CH{-}CH_2OCOO$), 4.55 (t, 9, 1H, $ClCH_2CH{-}CH_2{-}OCOO$), 4.36 (dd, 9, 6, 1H, $ClCH_2CH{-}CH_2{-}OCOO$), 3.75 (m, 2H, $Cl{-}CH_2{-}CHCH_2OCOO$), 3.54 (dd, 9, 6, 2H, $Cl{-}CH_2{-}CHCH_2O$), 3.19 (m, 1H, $ClCH_2{-}CH{-}CH_2O$), 2.85 (t, 5, 1H, $ClCH_2CH{-}CH_2{-}O$), 2.65 (dd, 9, 6, 1H, $ClCH_2CH{-}CH_2{-}O$), 2.23 (s, 9H, mesitylene methyl groups). The starting material peaks could clearly be observed, this could be a result of stuck starting material from the first run. Some unassigned peaks from contaminations were also observed.

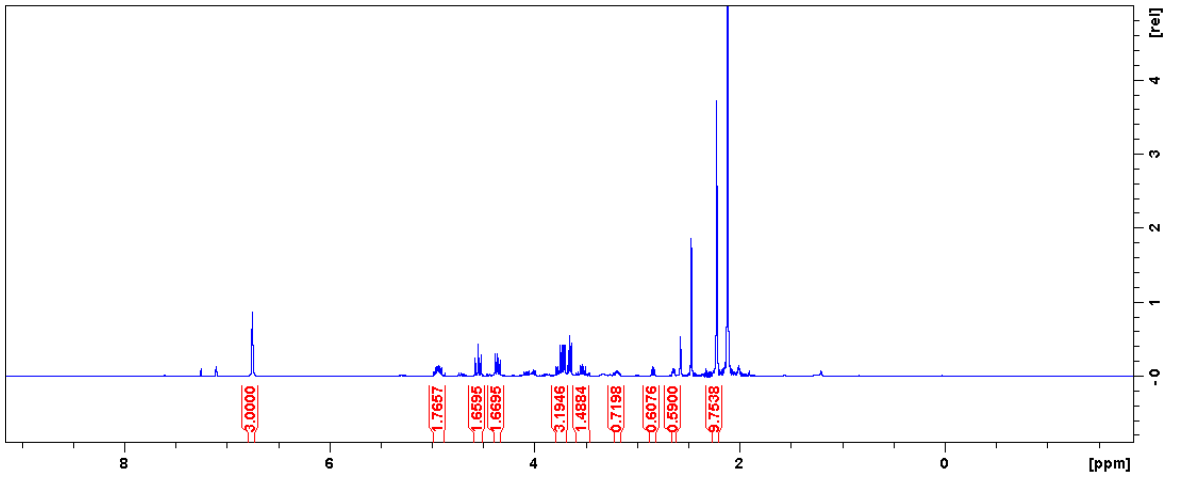


**Figure C.17:** $^{1}$H NMR of reaction mixture obtained during the second catalytic run of Co@Porph@PMO (6 bar $CO_2$, 1 hour)

## C.2 Luminescence data

**Emission map**: **Figure C.18** shows the emission map of Tb,Eu(1:1)@Pic@PMO. Both absolute and relative intensities of the different peaks vary with the excitation wavelength.

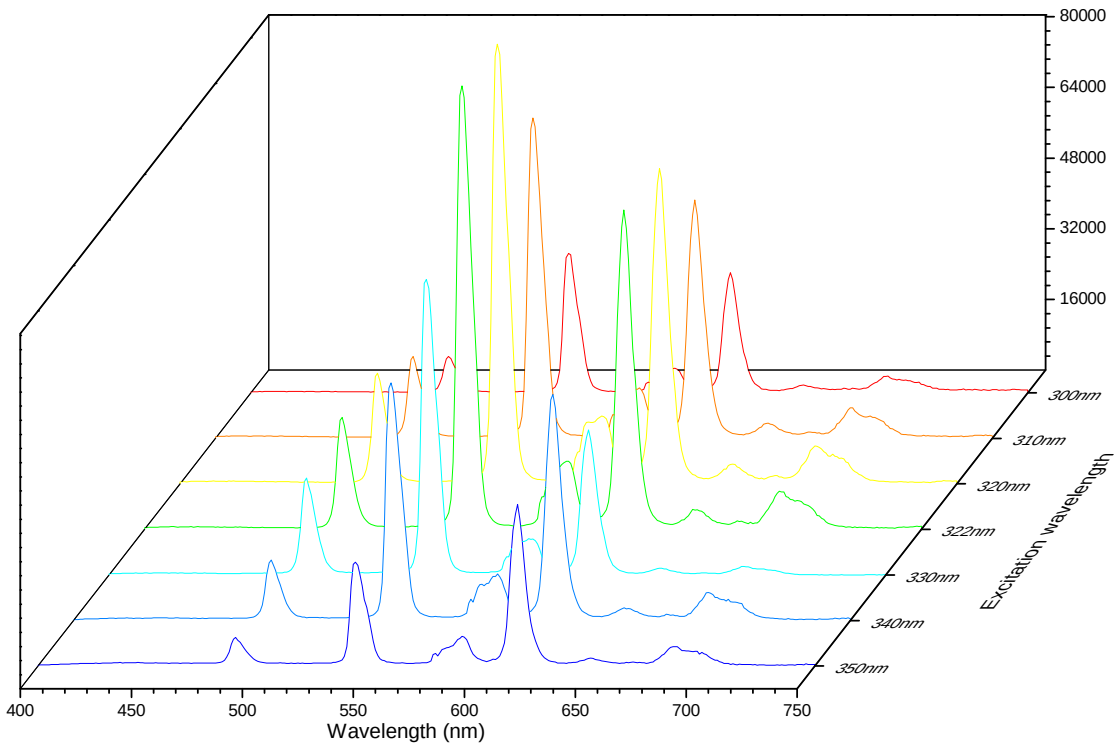


**Figure C.18:** Emission map of Tb,Eu(1:1)@Pic@PMO: observed emission profiles for different excitation wavelengths

**Decay profiles**: In **Figure C.19** and **Figure C.20** the decay profiles of Pic@PMO and Tb,Eu(1,1)@Pic@PMO, respectively, are given. Tb,Eu(1:1)@Pic@PMO shows different decay profiles for the 542 nm peak (corresponding to $Tb^{3+}$ luminescence) and the 616 nm peak (corresponding to $Eu^{3+}$ luminescence)

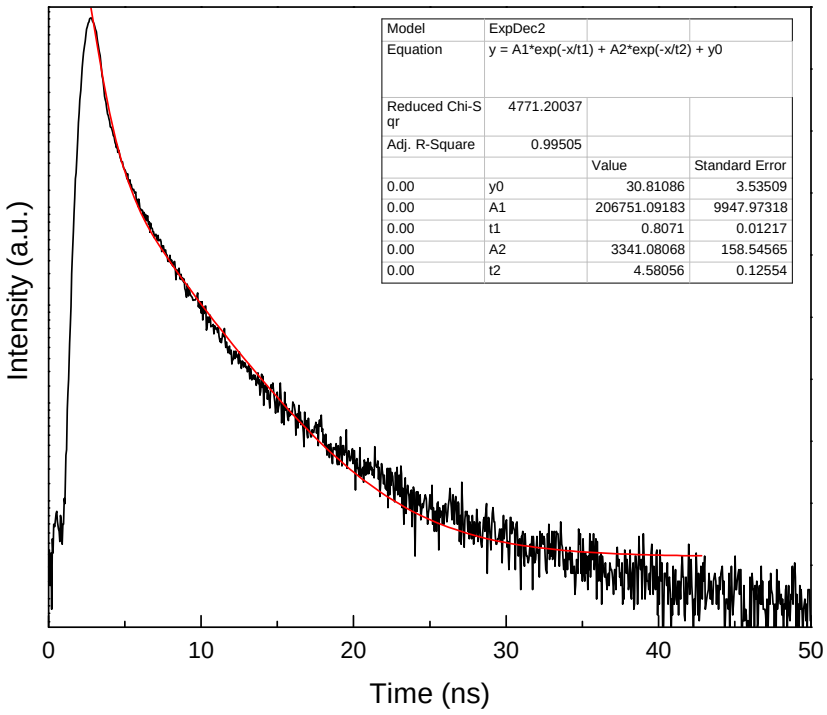


**Figure C.19:** Decay profile of pure Pic@PMO

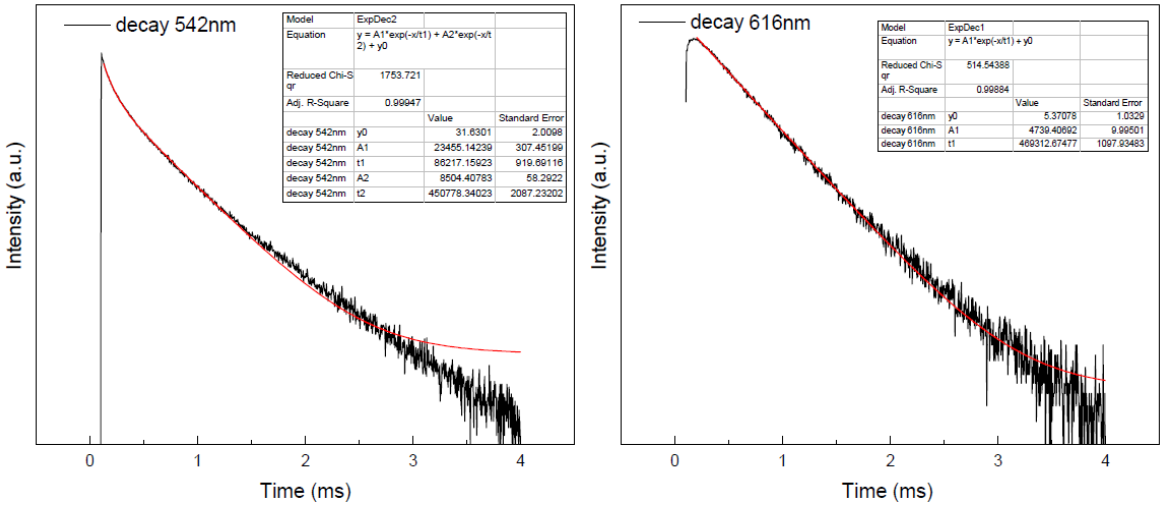


**Figure C.20:** Decay profile of Tb,Eu(1:1)@Pic@PMO, left decay of the 542 nm peak, right decay of the 616 nm peak

## C.3 Stability

The DTA spectra of Pic@PMO 3 and Porph@PMO 2 are presented in **Figure C.21**. It could be observed that the mass loss seen in the TGA spectra corresponds with a negative DTA peak. This means that the mass loss is an exothermic process, indicating oxidative degradation.

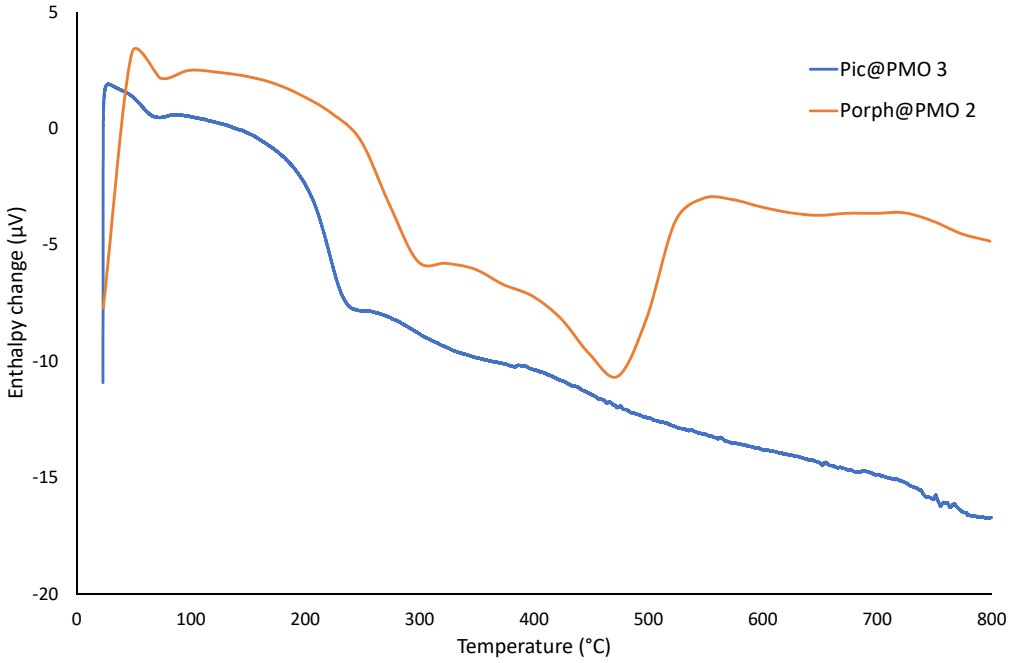


**Figure C.21:** DTA spectra of Pic@PMO 3 and Porph@PMO 2

# Bibliography


[1] C. Colella and A. F. Gualtieri. Cronstedt's zeolite. *Microporous and Mesoporous Materials*, 105(3):213–221, 2007.

[2] C. S. Cundy and P. A. Cox. The hydrothermal synthesis of zeolites: History and development from the earliest days to the present time. *Chemical Reviews*, 103(3):663–701, 2003.

[3] Pascal Van der Voort. Solid state chemistry. Course text, 2016-2017.

[4] C. T. Kresge, M. E. Leonowicz, W. J. Roth, J. C. Vartuli, and J. S. Beck. Ordered mesoporous molecular-sieves synthesized by a liquid-crystal template mechanism. *Nature*, 359(6397):710–712, 1992.

[5] D. Y. Zhao, J. L. Feng, Q. S. Huo, N. Melosh, G. H. Fredrickson, B. F. Chmelka, and G. D. Stucky. Triblock copolymer syntheses of mesoporous silica with periodic 50 to 300 angstrom pores. *Science*, 279(5350):548–552, 1998.

[6] J. Ouwehand. A novel thiol functionalized periodic mesoporous organosilica as adsorbent and bifunctional catalyst. Masterthesis, Ghent University, 2014.

[7] T. Asefa, M. J. MacLachlan, N. Coombs, and G. A. Ozin. Periodic mesoporous organosilicas with organic groups inside the channel walls. *Nature*, 402(6764):867–871, 1999.

[8] B. J. Melde, B. T. Holland, C. F. Blanford, and A. Stein. Mesoporous sieves with unified hybrid inorganic/organic frameworks. *Chemistry of Materials*, 11(11):3302–3308, 1999.

[9] S. Inagaki, S. Guan, Y. Fukushima, T. Ohsuna, and O. Terasaki. Novel mesoporous materials with a uniform distribution of organic groups and inorganic oxide in their frameworks. *Journal of the American Chemical Society*, 121(41):9611–9614, 1999.

[10] S. Clerick. *Ultra-stable ring-type organosilicas with click modifiable groups: application as chromatographic support and HPLC packing.* Phd thesis, Ghent University, 2017.

[11] P. Van der Voort, D. Esquivel, E. De Canck, F. Goethals, I. Van Driessche, and F. J. Romero-Salguero. Periodic mesoporous organosilicas: from simple to complex bridges; a comprehensive overview of functions, morphologies and applications. *Chemical Society Reviews*, 42(9):3913–3955, 2013.

[12] M. A. Wahab and J. N. Beltramini. Recent advances in hybrid periodic mesostructured organosilica materials: opportunities from fundamental to biomedical applications. *Rsc Advances*, 5(96):79129–79151, 2015.

[13] N. Mizoshita, T. Tani, and S. Inagaki. Syntheses, properties and applications of periodic mesoporous organosilicas prepared from bridged organosilane precursors. *Chemical Society Reviews*, 40(2):789–800, 2011.

[14] M. P. Kapoor and S. Inagaki. Highly ordered mesoporous organosilica hybrid materials. *Bulletin of the Chemical Society of Japan*, 79(10):1463–1475, 2006.

[15] T. Sakurai and T. Iizuka. Gate electrode rc delay effects in vlsis. *Ieee Transactions on Electron Devices*, 32(2):370–374, 1985.

[16] F. Goethals, I. Ciofi, O. Madia, K. Vanstreels, M. R. Baklanov, C. Detavernier, P. Van der Voort, and I. Van Driessche. Ultra-low-k cyclic carbon-bridged pmo films with a high chemical resistance. *Journal of Materials Chemistry*, 22(17):8281–8286, 2012.

[17] M. Redzheb, S. Armini, T. Berger, M. Jacobs, M. Krishtab, K. Vanstreels, S. Bernstorff, and P. Van der Voort. On the mechanical and electrical properties of self-assembly-based organosilicate porous films. *Journal of Materials Chemistry C*, 5(33):8599–8607, 2017.

[18] M. Ide, E. De Canck, I. Van Driessche, F. Lynen, and P. Van der Voort. Developing a new and versatile ordered mesoporous organosilica as a ph and temperature stable chromatographic packing material. *Rsc Advances*, 5(8):5546–5552, 2015.

[19] G. R. Zhu, D. M. Jiang, Q. H. Yang, J. Yang, and C. Li. trans-(1r,2r)-diaminocyclohexane-functionalized mesoporous organosilica spheres as chiral stationary phase. *Journal of Chromatography A*, 1149(2):219–227, 2007.

[20] A. Walcarius and L. Mercier. Mesoporous organosilica adsorbents: nanoengineered materials for removal of organic and inorganic pollutants. *Journal of Materials Chemistry*, 20(22):4478–4511, 2010.

[21] M. C. Burleigh, S. Dai, E. W. Hagaman, and J. S. Lin. Imprinted polysilsesquioxanes for the enhanced recognition of metal ions. *Chemistry of Materials*, 13(8):2537–2546, 2001.

[22] S. Z. Qiao, C. Z. Yu, W. Xing, Q. H. Hu, H. Djojoputro, and G. Q. Lu. Synthesis and bio-adsorptive properties of large-pore periodic mesoporous organosilica rods. *Chemistry of Materials*, 17(24):6172–6176, 2005.

[23] M. S. Bhattacharyya, P. Hiwale, M. Piras, L. Medda, D. Steri, M. Piludu, A. Salis, and M. Monduzzi. Lysozyme adsorption and release from ordered mesoporous materials. *Journal of Physical Chemistry C*, 114(47):19928–19934, 2010.

[24] X. Q. Wang, D. N. Lu, R. Austin, A. Agarwal, L. J. Mueller, Z. Liu, J. Z. Wu, and P. Y. Feng. Protein refolding assisted by periodic mesoporous organosilicas. *Langmuir*, 23(10):5735–5739, 2007.

[25] E. De Canck, C. Vercaemst, F. Verpoort, and P. Van Der Voort. A new sulphonic acid functionalized periodic mesoporous organosilica as a suitable catalyst. In Eric M Gaigneaux, M Devillers, S Hermans, PA Jacobs, JA Martens, and P Ruiz, editors, *Studies in Surface Science and Catalysis*, volume 175, pages 365–368. Elsevier, 2010.

[26] E. De Canck, I. Dosuna-Rodríguez, E. M. Gaigneaux, and P. Van Der Voort. Periodic mesoporous organosilica functionalized with sulfonic acid groups as acid catalyst for glycerol acetylation. *Materials*, 6(8):3556–3570, 2013.

[27] M. I. López, D. Esquivel, C. Jiménez-Sanchidrián, F. J. Romero-Salguero, and P. Van Der Voort. A 'one-step' sulfonic acid pmo as a recyclable acid catalyst. *Journal of Catalysis*, 326:139–148, 2015.

[28] D. Dube, M. Rat, W. Shen, F. Beland, and S. Kaliaguine. Perfluoroalkylsulfonic acid-functionalized periodic mesostructured organosilica: a strongly acidic heterogeneous catalyst. *Journal of Materials Science*, 44(24):6683–6692, 2009.

[29] S. El Hankari, B. Motos-Perez, P. Hesemann, A. Bouhaouss, and J. J. E. Moreau. Pore size control and organocatalytic properties of nanostructured silica hybrid materials containing amino and ammonium groups. *Journal of Materials Chemistry*, 21(19):6948–6955, 2011.

[30] L. Zhang, J. Liu, J. Yang, Q. H. Yang, and C. Li. Direct synthesis of highly ordered amine-functionalized mesoporous ethane-silicas. *Microporous and Mesoporous Materials*, 109(1-3):172–183, 2008.

[31] E. A. Prasetyanto, M. B. Ansari, B. H. Min, and S. E. Park. Melamine tri-silsesquioxane bridged periodic mesoporous organosilica as an efficient metal-free catalyst for co(2) activation. *Catalysis Today*, 158(3-4):252–257, 2010.

[32] J. A. Melero, J. Iglesias, J. M. Arsuaga, J. Sainz-Pardo, P. de Frutos, and S. Blazquez. Synthesis and catalytic activity of organic-inorganic hybrid ti-sba-15 materials. *Journal of Materials Chemistry*, 17(4):377–385, 2007.

[33] S. Sisodiya, S. Shylesh, and A. P. Singh. Tin incorporated periodic mesoporous organosilicas (sn-pmos): Synthesis, characterization, and catalytic activity in the epoxidation reaction of olefins. *Catalysis Communications*, 12(7):629–633, 2011.

[34] S. Shylesh and A. P. Singh. Vanadium-containing ethane-silica hybrid periodic mesoporous organosilicas: Synthesis, structural characterization and catalytic applications. *Microporous and Mesoporous Materials*, 94(1-3):127–138, 2006.

[35] A. Feliczak, K. Walczak, A. Wawrzynczak, and I. Nowak. The use of mesoporous molecular sieves containing niobium for the synthesis of vegetable oil-based products. *Catalysis Today*, 140(1-2):23–29, 2009.

[36] S. Shylesh, P. P. Samuel, and A. P. Singh. Synthesis of hydrothermally stable aluminium-containing ethane-silica hybrid mesoporous materials using different aluminium sources. *Microporous and Mesoporous Materials*, 100(1-3):250–258, 2007.

[37] S. Shylesh, C. Srilakshmi, A. P. Singh, and B. G. Anderson. One step synthesis of chromium-containing periodic mesoporous organosilicas and their catalytic activity in the oxidation of cyclohexane. *Microporous and Mesoporous Materials*, 99(3):334–344, 2007.

[38] V. Dufaud, F. Beauchesne, and L. Bonneviot. Organometallic chemistry inside the pore walls of mesostructured silica materials. *Angewandte Chemie-International Edition*, 44(22):3475–3477, 2005.

[39] F. Zhang, C. M. Kang, Y. Y. Wei, and H. X. Li. Aerosol-spraying synthesis of periodic mesoporous organometalsilica spheres with chamber cavities as active and reusable catalysts in aqueous organic reactions. *Advanced Functional Materials*, 21(16):3189–3197, 2011.

[40] X. S. Yang, F. X. Zhu, J. L. Huang, F. Zhang, and H. X. Li. Phenyl@rh(i)-bridged periodic mesoporous organometalsilica with high catalytic efficiency in water-medium organic reactions. *Chemistry of Materials*, 21(20):4925–4933, 2009.

[41] J. L. Huang, F. X. Zhu, W. H. He, F. Zhang, W. Wang, and H. X. Li. Periodic mesoporous organometallic silicas with unary or binary organometals inside the channel walls as active and reusable catalysts in aqueous organic reactions. *Journal of the American Chemical Society*, 132(5):1492–+, 2010.

[42] J. Alauzun, A. Mehdi, C. Reye, and R. J. P. Corriu. Mesoporous materials with an acidic framework and basic pores. a successful cohabitation. *Journal of the American Chemical Society*, 128(27):8718–8719, 2006.

[43] X. Liu, P. Y. Wang, Y. Yang, P. Wang, and Q. H. Yang. (r)-(+)-binol-functionalized mesoporous organosilica as a highly efficient pre-chiral catalyst for asymmetric catalysis. *Chemistry-an Asian Journal*, 5(5):1232–1239, 2010.

[44] A. Kuschel and S. Polarz. Effects of primary and secondary surface groups in enantioselective catalysis using nanoporous materials with chiral walls. *Journal of the American Chemical Society*, 132(18):6558–6565, 2010.

[45] S. Clerick, E. De Canck, K. Hendrickx, V. Van Speybroeck, and P. Van der Voort. Heterogeneous ru(iii) oxidation catalysts via 'click' bidentate ligands on a periodic mesoporous organosilica support. *Green Chemistry*, 18(22):6035–6045, 2016.

[46] M. Rat, M. H. Zahedi-Niaki, S. Kaliaguine, and T. O. Do. Sulfonic acid functionalized periodic mesoporous organosilicas as acetalization catalysts. *Microporous and Mesoporous Materials*, 112(1-3):26–31, 2008.

[47] W. P. Guo, X. Li, and X. S. Zhao. Understanding the hydrothermal stability of large-pore periodic mesoporous organosilicas and pure silicas. *Microporous and Mesoporous Materials*, 93(1-3):285–293, 2006.

[48] K. Landskron, B. D. Hatton, D. D. Perovic, and G. A. Ozin. Periodic mesoporous organosilicas containing interconnected si(ch2) (3) rings. *Science*, 302(5643):266–269, 2003.

[49] F. Goethals, B. Meeus, A. Verberckmoes, P. Van der Voort, and I. Van Driessche. Hydrophobic high quality ring pmos with an extremely high stability. *Journal of Materials Chemistry*, 20(9):1709–1716, 2010.

[50] H. C. Kolb, M. G. Finn, and K. B. Sharpless. Click chemistry: Diverse chemical function from a few good reactions. *Angewandte Chemie-International Edition*, 40(11):2004–+, 2001.

[51] C. E. Hoyle and C. N. Bowman. Thiol-ene click chemistry. *Angewandte Chemie-International Edition*, 49(9):1540–1573, 2010.

[52] D. Esquivel, O. van den Berg, F. J. Romero-Salguero, F. Du Prez, and P. Van Der Voort. 100% thiol-functionalized ethylene pmos prepared by "thiolacid-ene" chemistry. *Chemical Communications*, 49(23):2344–2346, 2013.

[53] J. Gehring, B. Trepka, N. Klinkenberg, H. Bronner, D. Schleheck, and S. Polarz. Sunlight-triggered nanoparticle synergy: Teamwork of reactive oxygen species and nitric oxide released from mesoporous organosilica with advanced antibacterial activity. *Journal of the American Chemical Society*, 138(9):3076–3084, 2016.

[54] M. Besouw, R. Masereeuw, L. van den Heuvel, and E. Levtchenko. Cysteamine: an old drug with new potential. *Drug Discovery Today*, 18(15-16):785–792, 2013.

[55] CYSTARAN drug information. `http://www.empr.com/cystaran/drug/8411/`. Accessed: 21-03-2018.

[56] F. Goethals, C. Vercaemst, V. Cloet, S. Hoste, P. Van Der Voort, and I. Van Driessche. Comparative study of ethylene- and ethenylene-bridged periodic mesoporous organosilicas. *Microporous and Mesoporous Materials*, 131(1-3):68–74, 2010.

[57] Carl Vercaemst. *Isomeric Olefinic Periodic Mesoporous Organosilicas: An Emerging Class of Versatile Nano- materials*. Doctoraatsthesis, Ghent University, 2009.

[58] Stephen Brunauer, P. H. Emmett, and Edward Teller. Adsorption of gases in multimolecular layers. *Journal of the American Chemical Society*, 60(2):309–319, 1938.

[59] Elliott P. Barrett, Leslie G. Joyner, and Paul P. Halenda. The determination of pore volume and area distributions in porous substances. i. computations from nitrogen isotherms. *Journal of the American Chemical Society*, 73(1):373–380, 1951.

[60] A. Zürner, J. Kirstein, M. Döblinger, C. Bräuchle, and T. Bein. Visualizing single-molecule diffusion in mesoporous materials. *Nature*, 450:705–708, 2007.

[61] P. Anzenbacher, V. Kral, K. Jursikova, J. Gunterova, and A. Kasal. Porphyrins covalently bound to polystyrene .2. an efficient model of monooxygenase reactivity. *Journal of Molecular Catalysis a-Chemical*, 118(1):63–68, 1997.

[62] M. C. Burleigh, M. A. Markowitz, M. S. Spector, and B. P. Gaber. Direct synthesis of periodic mesoporous organosilicas: Functional incorporation by co-condensation with organosilanes. *Journal of Physical Chemistry B*, 105(41):9935–9942, 2001.

[63] M. Vasconcellos-Dias, C. D. Nunes, P. D. Vaz, P. Ferreira, P. Brandao, V. Felix, and M. J. Calhorda. Heptacoordinate tricarbonyl mo(ii) complexes as highly selective oxidation homogeneous and heterogeneous catalysts. *Journal of Catalysis*, 256(2):301–311, 2008.

[64] M. S. Moorthy, M. J. Kim, J. H. Bae, S. S. Park, N. Saravanan, S. H. Kim, and C. S. Ha. Multifunctional periodic mesoporous organosilicas for biomolecule recognition, biomedical applications in cancer therapy, and metal adsorption. *European Journal of Inorganic Chemistry*, 17:3028–3038, 2013.

[65] P. Borah, J. Mondal, and Y. L. Zhao. Urea-pyridine bridged periodic mesoporous organosilica: An efficient hydrogen-bond donating heterogeneous organocatalyst for henry reaction. *Journal of Catalysis*, 330:129–134, 2015.

[66] M. S. Liu, X. Y. Lu, L. Shi, F. X. Wang, and J. M. Sun. Periodic mesoporous organosilica with a basic urea-derived framework for enhanced carbon dioxide capture and conversion under mild conditions. *Chemsuschem*, 10(6):1110–1119, 2017.

[67] L. R. Milgrom. *The Colours of Life: An Introduction to the Chemistry of Porphyrins and Related Compounds*. Oxford University Press: New York, 1997.

[68] K. M. Kadish, Smith K. M., and R. Guilard. *The Porhyrin Handbook*. Academic Press, 2000.

[69] J. S. Miller. Organometallic- and organic-based magnets: New chemistry and new materials for the new millennium. *Inorganic Chemistry*, 39(20):4392–4408, 2000.

[70] R. Wiglusz, J. Legendziewicz, A. Graczyk, S. Radzki, P. Gawryszewska, and J. Sokolnicki. Spectroscopic properties of porphyrins and effect of lanthanide ions on their luminescence efficiency. *Journal of Alloys and Compounds*, 380(1-2):396–404, 2004.

[71] A. Yella, H. W. Lee, H. N. Tsao, C. Y. Yi, A. K. Chandiran, M. K. Nazeeruddin, E. W. G. Diau, C. Y. Yeh, S. M. Zakeeruddin, and M. Gratzel. Porphyrin-sensitized solar cells with cobalt (ii/iii)-based redox electrolyte exceed 12 percent efficiency. *Science*, 334(6056):629–634, 2011.

[72] T. J. Dougherty, C. J. Gomer, B. W. Henderson, G. Jori, D. Kessel, M. Korbelik, J. Moan, and Q. Peng. Photodynamic therapy. *Journal of the National Cancer Institute*, 90(12):889–905, 1998.

[73] V. Bulach, F. Sguerra, and M. W. Hosseini. Porphyrin lanthanide complexes for nir emission. *Coordination Chemistry Reviews*, 256(15-16):1468–1478, 2012.

[74] B. Meunier. Metalloporphyrins as versatile catalysts for oxidation reactions and oxidative dna cleavage. *Chemical Reviews*, 92(6):1411–1456, 1992.

[75] C. Maeda, Y. Miyazaki, and T. Ema. Recent progress in catalytic conversions of carbon dioxide. *Catalysis Science & Technology*, 4(6):1482–1497, 2014.

[76] N. E. Leadbeater and M. Marco. Preparation of polymer-supported ligands and metal complexes for use in catalysis. *Chemical Reviews*, 102(10):3217–3273, 2002.

[77] B. Johnson-White, M. Zeinali, A. P. Malanoski, and M. A. Dinderman. Sunlight-catalyzed conversion of cyclic organics with novel mesoporous organosilicas. *Catalysis Communications*, 8(7):1052–1056, 2007.

[78] E. Y. Jeong, A. Burri, S. Y. Lee, and S. E. Park. Synthesis and catalytic behavior of tetrakis(4-carboxyphenyl) porphyrin-periodic mesoporous organosilica. *Journal of Materials Chemistry*, 20(48):10869–10875, 2010.

[79] E. Y. Jeong and S. E. Park. Synthesis of porphyrin-bridged periodic mesoporous organosilica and their catalytic applications. *Research on Chemical Intermediates*, 38(6):1237–1248, 2012.

[80] E. M. Gale, A. K. Patra, and T. C. Harrop. Versatile methodology toward nin2s2 complexes as nickel superoxide dismutase models: Structure and proton affinity. *Inorganic Chemistry*, 48(13):5620–5622, 2009.

[81] P. E. Dawson, T. W. Muir, I. Clarklewis, and S. B. H. Kent. Synthesis of proteins by native chemical ligation. *Science*, 266(5186):776–779, 1994.

[82] G. J. Kramer. Hydrocarbons in a net-zero emission world. Lecture at NCCC XIX, march 2018.

[83] P. Markewitz, W. Kuckshinrichs, W. Leitner, J. Linssen, P. Zapp, R. Bongartz, A. Schreiber, and T. E. Muller. Worldwide innovations in the development of carbon capture technologies and the utilization of co2. *Energy —& Environmental Science*, 5(6):7281–7305, 2012.

[84] A. Goeppert, M. Czaun, G. K. S. Prakash, and G. A. Olah. Air as the renewable carbon source of the future: an overview of co2 capture from the atmosphere. *Energy & Environmental Science*, 5(7):7833–7853, 2012.

[85] E. V. Kondratenko, G. Mul, J. Baltrusaitis, G. O. Larrazabal, and J. Perez-Ramirez. Status and perspectives of co2 conversion into fuels and chemicals by catalytic, photocatalytic and electrocatalytic processes. *Energy & Environmental Science*, 6(11):3112–3135, 2013.

[86] M. Aresta. *Carbon Dioxide as Chemical Feedstock*. Wiley-VCH, 2010.

[87] C. Martin, G. Fiorani, and A. W. Kleij. Recent advances in the catalytic preparation of cyclic organic carbonates. *Acs Catalysis*, 5(2):1353–1370, 2015.

[88] X. B. Lu, Y. J. Zhang, B. Liang, X. Li, and H. Wang. Chemical fixation of carbon dioxide to cyclic carbonates under extremely mild conditions with highly active bifunctional catalysts. *Journal of Molecular Catalysis a-Chemical*, 210(1-2):31–34, 2004.

[89] R. L. Paddock and S. T. Nguyen. Chemical co2 fixation: Cr(iii) salen complexes as highly efficient catalysts for the coupling of co2 and epoxides. *Journal of the American Chemical Society*, 123(46):11498–11499, 2001.

[90] Y. M. Shen, W. L. Duan, and M. Shi. Chemical fixation of carbon dioxide catalyzed by binaphthyldiamino zn, cu, and co salen-type complexes. *Journal of Organic Chemistry*, 68(4):1559–1562, 2003.

[91] T. Aida and S. Inoue. Activation of carbon-dioxide with aluminum porphyrin and reaction with epoxide - studies on (tetraphenylporphinato)aluminum alkoxide having a long oxyalkylene chain as the alkoxide group. *Journal of the American Chemical Society*, 105(5):1304–1309, 1983.

[92] W. J. Kruper and D. V. Dellar. Catalytic formation of cyclic carbonates from epoxides and co2 with chromium metalloporphyrinates. *Journal of Organic Chemistry*, 60(3):725–727, 1995.

[93] R. L. Paddock, Y. Hiyama, J. M. McKay, and S. T. Nguyen. Co(iii) porphyrin/dmap: an efficient catalyst system for the synthesis of cyclic carbonates from co2 and epoxides. *Tetrahedron Letters*, 45(9):2023–2026, 2004.

[94] L. L. Jin, H. W. Jing, T. Chang, X. L. Bu, L. Wang, and Z. L. Liu. Metal porphyrin/phenyltrimethylammonium tribromide: High efficient catalysts for coupling reaction of co2 and epoxides. *Journal of Molecular Catalysis a-Chemical*, 261(2):262–266, 2007.

[95] M. Cokoja, M. E. Wilhelm, M. H. Anthofer, W. A. Herrmann, and F. E. Kuhn. Synthesis of cyclic carbonates from epoxides and carbon dioxide by using organocatalysts. *Chemsuschem*, 8(15):2436–2454, 2015.

[96] D. S. Bai, Q. O. Wang, Y. Y. Song, B. Li, and H. W. Jing. Synthesis of cyclic carbonate from epoxide and co2 catalyzed by magnetic nanoparticle-supported porphyrin. *Catalysis Communications*, 12(7):684–688, 2011.

[97] A. B. Chen, P. P. Ju, Y. Z. Zhang, J. Z. Chen, H. Gao, L. M. Chen, and Y. F. Yu. Highly recyclable and magnetic catalyst of a metalloporphyrin-based polymeric composite for cycloaddition of co2 to epoxide. *Rsc Advances*, 6(99):96455–96466, 2016.

[98] M. Cokoja, C. Bruckmeier, B. Rieger, W. A. Herrmann, and F. E. Kuhn. Transformation of carbon dioxide with homogeneous transition-metal catalysts: A molecular solution to a global challenge? *Angewandte Chemie-International Edition*, 50(37):8510–8537, 2011.

[99] Rik Van Deun. The f-elements. Course text, 2017-2018.

[100] K. A. J. Gschneidner and L. R. Eyring. *Handbook on the physics and chemistry of rare earths*. North-holland publishing company, 1978.

[101] S. V. Eliseeva and J. C. G. Bunzli. Lanthanide luminescence for functional materials and bio-sciences. *Chemical Society Reviews*, 39(1):189–227, 2010.

[102] K. Binnemans. Lanthanide-based luminescent hybrid materials. *Chemical Reviews*, 109(9):4283–4374, 2009.

[103] B. Yan. Recent progress in photofunctional lanthanide hybrid materials. *Rsc Advances*, 2(25):9304–9324, 2012.

[104] A. M. Kaczmarek, D. Esquivel, J. Ouwehand, P. Van der Voort, F. J. Romero-Salguero, and R. Van Deun. Temperature dependent nir emitting lanthanide-pmo/silica hybrid materials. *Dalton Transactions*, 46(24):7878–7887, 2017.

[105] S. Biju, Y. K. Eom, J. C. G. Bunzli, and H. K. Kim. Biphenylene-bridged mesostructured organosilica as a novel hybrid host material for ln(iii) (ln = eu, gd, tb, er, yb) ions in the presence of 2-thenoyltrifluoroacetone. *Journal of Materials Chemistry C*, 1(21):3454–3466, 2013.

[106] Q. M. Wang and B. Yan. A novel way to prepare luminescent terbium molecular-scale hybrid materials: Modified heterocyclic ligands covalently bonded with silica. *Crystal Growth & Design*, 5(2):497–503, 2005.

[107] W. T. Carnall, P. R. Fields, and K. Rajnak. Electronic energy levels of the trivalent lanthanide aquo ions .iv. eu3+. *Journal of Chemical Physics*, 49(10):4450–4455, 1968.

[108] J. H. Xue, X. H. Hua, L. M. Yang, W. H. Li, Y. Z. Xu, G. Z. Zhao, G. H. Zhang, K. X. Liu, J. E. Chen, and J. G. Wu. Synthesis, crystal structures and luminescence properties of europium and terbium picolinamide complexes. *Chinese Chemical Letters*, 25(6):887–891, 2014.

[109] W. T. Carnall, P. R. Fields, and K. Rajnak. Electronic energy levels of the trivalent lanthanide aquo ions .iii. tb3+. *Journal of Chemical Physics*, 49(10):4447–4449, 1968.

[110] International Electrotechnical Commission and International Commission on Illumination. *International lighting Vocabulary*. Publication (International Electrotechnical Commission). Bureau Central de la Commission Electrotechnique Internationale, 1987.

[111] J.L. Soret. Analyse spectrale: Sur le spectre d'absorption du sang dans la partie violette et ultra-violette. *Comptes rendus de l'Académie des sciences*, 97:1269–1270, 1883.

[112] J. C. G. Bunzli, S. Comby, A. S. Chauvin, and C. D. B. Vandevyver. New opportunities for lanthanide luminescence. *Journal of Rare Earths*, 25(3):257–274, 2007.

[113] W. K. Wong, X. Zhu, and W. Y. Wong. Synthesis, structure, reactivity and photoluminescence of lanthanide(iii) monoporphyrinate complexes. *Coordination Chemistry Reviews*, 251(17-20):2386–2399, 2007.